NORTHWESTERN UNIVERSITY

# Engineered Peptide Platforms: Design, Synthesis and Application

A DISSERTATION

SUBMITTED TO THE GRADUATE SCHOOL

IN PARTIAL FULFILLMENT OF THE REQUIREMENTS

for the degree

DOCTOR OF PHILOSOPHY

Field of Chemistry

By

Wonmin Choi

EVANSTON, ILLINOIS

December 2021

# Abstract

Engineered Peptide Platforms: Design, Synthesis and Application

Wonmin Choi

Peptides consists of a series of amino acids connected via an amide type of covalent chemical bond. A diverse field of applications such as biosensors,[2] catalysis,[4] and biomedicine[6] include the oligomeric forms of peptides due to their genuine features comparing to other biomacromolecules. Particularly, peptides in the field of biomedical application have garnered much interest due to their biocompatibility, high selectivity, and potency.

Different platforms and technologies have been adopted to improve efficacy or expand the versatility of peptides. Peptide hydrogels, for example, have a three-dimensional fibrillar network structure employing self-assembly of peptides. Due to their low toxicity and biodegradability, peptide hydrogels have been widely used in different biomedical application such as drug delivery,[7] protein separation,[8] biosensors,[9] tissue engineering,[10] and wound healing.[11] The protein-like polymer (PLP) is another class of peptide employing platform where peptides are densely arranged onto a hydrophobic polymer backbone, giving a globular structure similar to natural proteins. PLPs show unique properties compared to other peptide based therapeutics such as increased cellular uptake or enhanced enzyme resistance, thus opening a new opportunity for therapeutic peptide delivery.

This thesis explores the diverse peptide platforms from biological signal responsive peptide materials to the PLP as a novel technology for peptide drug delivery. In Chapter 1, a brief

introduction of different engineered peptide platforms will be discussed. In Chapter 2 and 3, the pH-responsive charge conversion peptide pro-gelators and light-activatable enzyme responsive nanoparticles are described, respectively, as advanced design of stimuli-responsive peptide materials. In Chapter 4, the backbone effect of PLPs to enzyme resistance is discussed. Enzyme resistance of PLPs with different backbone structures is further demonstrated by both experimental results and computational simulations. A new synthetic route for PLPs is introduced in Chapter 5. PLP synthesis with photo-induced electron/energy transfer-reversible addition-fragmentation chain transfer polymerization (PET-RAFT) provides mild and environmentally friendly polymerization methods. Finally, therapeutic application of PLPs to treat Huntington's Disease (HD) and neovascular age-related macular degeneration (nAMD) will be discussed in Chapter 6 and 7.

# Acknowledgement

First and foremost, I would like to express my deepest gratitude to my advisor Prof. Nathan Gianneschi for his great support and mentorship. Thinking back to where I was and where I am now, it was never easy to settle into different culture and environment especially because I move from Korea to San Diego and from San Diego to Chicago. And all of this life journey starts from him. Every time, he always provided an environment that I can only focus on the research. Also, he gave me great opportunities to work with wonderful collaborators so that I can adventure different field of science. This helps me a lot to be grown up as a scientist.

Also, I would like to thank all of my committee members, Prof. Richard Silverman, Prof. Julia Kalow and previous member, Prof. Thomas O'Halloran for their fruitful feedbacks and guidance. Also, I appreciate Prof. Chad Mirkin for serving as my preliminary committee.

I also appreciate my dearest collaborators for teaching me with their expertise and knowledge. I feel so privileged to have them as collaborators. Thank you to Prof. Monica de la Cruz and Dr. Baofu Qiao for guiding me to a new area of computational analysis of PLPs. Also, I would like to thank Prof. Jeremy Lavine, Prof. Gregory Schwartz, Dr. Steven Droho and David Swygart for their untiring experimental trials and knowledge of disease to treat the neovascular age-related degeneration. I`m also grateful for Nayereh Ghoreishi-Haack, Dr. Lori Tran, Iwona Stephien, and Dr. Elizabeth Dempsey from Developmental Therapeutic Core (DTC) for their tremendous support of animal studies.

All of Gianneschi lab members taught me a lot with their kindness and intelligence. Dr. Matthew Thompson always helped me to get through all the tough situation in the lab and finally

find the best way. Also, every time I face difficulties in the experiment, he tried the best to support me with resources and knowledge. Thanks to his support, I could continue the experiment without any difficulties. I also want to thank Dr. Or Berger for the great collaboration and teaching me protein chemistry. In addition, I would like to thank Mara Fattah. She is a great mentee but also a good collaborator. It was such a great time to work with her and I really appreciate her for cheering me up with her good vibe. Also, I would like to thank Dr. Julia Oktaweic, Omar Ebrahim, Spencer Burton and Daniel Lee for being a good friend and doing good collaborations.

Further, I really want to thank Dr. Hao Sun for his tremendous support and encouragement. We had such a valued time to discuss the experiment, share the life experiences and plan for the future. His knowledge in polymer chemistry nourished me to become a better scientist. He is not only a great mentor but also my dearest friend. It was so lucky to have a friend like him. I would never expect to survive well without him. Lastly, I`m more than happy for him to pursue his academic dream in New Haven.

I also want to thank previous group members. I want to thank to Dr. Soumitra Punekar. We spent a lot of time to discuss the project and also had a good time to play with Fantasy Football. I also appreciate two of my great graduate mentors, Dr. Andrea Carlini and Dr. Cassandra Callmann, for their patience and teaching me their experimental skills. I also want to thank Dr. Claudia Battistella, Dr. Maria Proetto, and Dr. Ziying Hu for the great friendship and helping.

It is also important to mention my Master`s degree advisor Prof. Yan Lee. Under his supervision, I could learn how to do proper science. He introduced me the world of science and he is the reason why I have dreamed about being a scientist. Also, I want to thank Prof. Minkyu Kim

for his guidance and advice. In addition, I would like to thank Prof. Dokyung Kim. Since we met in San Diego, he becomes my good mentor and gave me fruitful suggestions.

Last but not least, I`d like to thank my incredible family. Their unconditional support and faith toward me are the reasons why I am here today. Lastly, I want to thank my fiancé Chan Song for her love and support from a deep heart.

# DEDICATION

To my beloved Family, Chan Song,

and God.

# Table of Contents

# List of Figures

**Chapter 4. Peptide Brush Polymer Backbone Governs Proteolytic Stability of Peptides**



**Chapter 5. Bioactive Peptide Brush Polymers via Photoinduced Reversible-Deactivation Radical Polymerization**

**Chapter 6. Protein-like Polymers for the Therapeutic Application : Neovascular Age-Related Macular Degeneration (nAMD)**



**Chapter 7. Protein-like Polymers for the Therapeutic Application: Huntington's Disease**

# List of Tables

# Chapter 1. Introduction to Engineered Peptide Platforms : From Stimuli-Responsive Nanomaterials to Protein-Like Polymers

## 1.1 Introduction

Peptides are one of nature's most important biomolecules. They consist of a series of amino acids which arrange into secondary or tertiary structures that give certain aspects of biological function. There are many classes of bioactive peptides in the nature, such as antimicrobial peptides, vasoactive intestinal peptides, immune/inflammatory peptides, endocrine peptides, brain peptides, etc. These peptides play important roles in the human body because they serve as biological messengers, carrying information from one tissue through the blood to another.

Diverse applications of peptides in a variety of fields have been possible due to the discovery of solid phase peptide synthesis (SPPS).[12] The ability of SPPS to synthesize peptide with high purity and multi-gram scalability has revolutionized peptide research and expanded the scope of applications such as biosensor, catalysis, and medicine. However, there is still a need for novel design of peptide containing materials due to the chemical and physical instability, tendency for aggregation, low membrane permeability, short half-life and fast elimination of the natural peptide.[13] Sophisticated and elaborate peptide systems have been developed and applied to different applications. In this chapter, different types of peptide platforms with de novo design strategies and their biomedical applications will be explored.

## 1.2 Stimuli-responsive peptide nanomaterials

### 1.2.1 pH-Responsive Self-Assembling Peptide

Peptides display distinguished properties such as stimuli-responsiveness, modularity and multi-functionality. These properties of peptides can be amplified by nanostructure assembly or functionalization. Self-assembling peptides (SAP) is one of the examples of well-ordered peptide nanostructures where peptides undergo spontaneous assembling into ordered nanostructures (Figure 1.1). Broad applications such as drug delivery,[14] molecular electronics,[15] regenerative medicine,[16] or tissue engineering[10] utilize SAP as a platform.

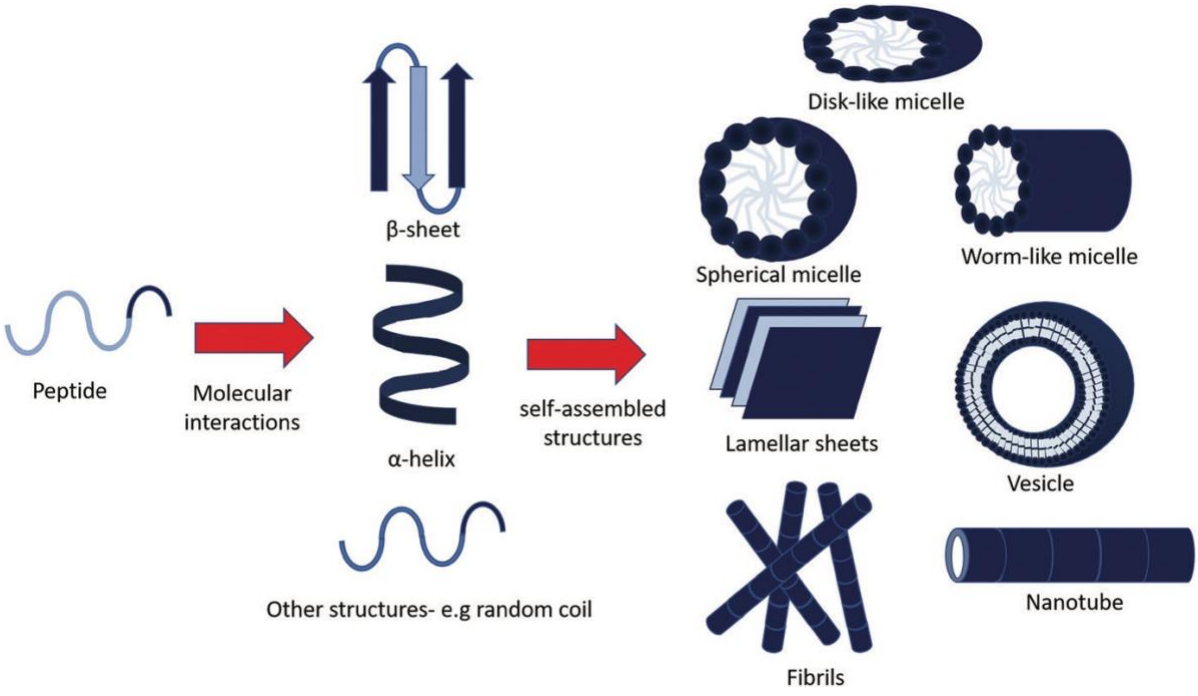


**Figure 1.1** Process of self-assembling peptides into different well-ordered nanostructures. Peptides assemble into secondary structure (e.g. β-sheet, α-helix, random coil) via molecular interactions and further construct the large scale nanostructures. Copyright 2017 The Royal Society of Chemistry.[17]

Although SAPs have been widely used in biomedical applications due to their chemical diversity, biocompatibility and biodegradability, there are several challenges that have yet to be solved such as low injectability and disease-targeting.

A simple strategy using the reversible charge-conversional properties of maleic acid derivatives is described to solve these challenges. Under acidic conditions, the maleic acid derivatives exhibit amide bond hydrolysis, converting the negative charges into positive charges. Using these properties, we developed pH-responsive peptide pro-gelators. These pro-gelators possess good injectability due to the negative charges of maleic acid derivatives. Under the acidic conditions, such as tissue acidosis mediated injury, including myocardial ischemia, rheumatoid arthritis, and articular damages, we anticipate the acid-induced mask hydrolysis renewing the zwitterionic nature of the peptides with concomitant and rapid self-assembly via B-sheet formation into rehealable hydrogels. More details will be discussed in the Chapter 2.

### 1.2.2 Enzyme & Light Dual Responsive Nanoparticle

Amphiphilic nanoparticles gained much interest in the biomedical field due to their enhanced permeability and retention (EPR) effect related to relatively small diameters ranging from 6 to 200nm, enabling systemic transport.[18] However, the EPR effect is a passive mechanism of accumulation limited to diseases that undergo rapid angiogenesis in their pathology. Active targeting of nanoparticles can be achieved by introducing either endogenous (pH, redox gradient , enzyme) or exogenous (temperature, light, magnetic field, ultrasound) stimuli-responsive moiety in the nanoparticles.[19, 20] Among different stimuli, enzymatic signal or enzyme-catalyzed reactions are highly efficient due to the selectivity to specific enzyme substrates under mild conditions.[21]

Also, enzymes are involved in numerous biological signal and metabolic pathways which makes them attractive target stimuli.[22] Peptides are the substrate or target of these enzyme-catalyzed reactions called proteolysis, the breakdown of peptides or proteins into smaller peptides or amino acids. Using enzyme mediated proteolysis, our lab has pioneered a polymeric nanoparticle delivery system that responds to enzymes such as matrix metalloproteinase (MMPs), which are overexpressed in the tumor microenvironment (TME) of many cancer types and other inflammatory disease including myocardial infarction.[23, 24]

Even if the nanoparticles are able to target and accumulate in the TME, and therefore reduce off-target side effects and maximize drug concentration, poor drug loading capacity and inefficient nanoparticle penetration into the tumor can limit their therapeutic efficacy. This work attempts to tackle those drawbacks of current nanoparticles for drug delivery systems by incorporating light cleavable drug monomers into the enzyme-responsive nanoparticles.

### 1.2.3 Protein-like Polymers : New class of peptide platform

At the most basic level, the poor activity of many peptide drug candidates results from both rapid renal filtration and fast proteolytic degradation upon administration. These effects translate into short *in vivo* half-lives and limited effect. Although frequent administration and higher dosages offer the opportunity to restore therapeutic activity, these routes result in more invasive and persistent treatments, raising costs from both the manufacturing standpoint and the need for extensive in clinic patient care. There are several approaches that have been developed to overcome these weaknesses, such as incorporation of unnatural amino acids,[25] peptide lipidation,[26] peptide cyclization,[27] the formation of lactam bridges[28] and stapling.[29] In addition, peptide-

polymers and more frequently protein-polymer conjugates have become a major class of materials. Most famously, these have been developed for the clinic in the form of PEGylated proteins,[30] with continued advancement in the age of functional group, and mild living polymerization chemistry.[31] In each case, the materials are arranged as end-on polymer protein conjugates, with one or more polymer chains linked to a single protein.

Within the general field of peptide-polymer bioconjugates, brush peptide-polymers have attracted attention, with recent contributions employing dual polymerization strategies (Figure 1.2).[32, 33] In this work, Wooley and coworkers reported a synthetic polymer brush architecture via graft-through polymerization of polypeptide monomers (Figure 1.2 A). Cheng and coworkers prepared polypeptides via NCA ROP in a graft-from approach from a backbone accessed via ROMP (Figure 1.2 B). In this manner, brush polymers of polypeptides are accessed but without control over the amino acid sequence.

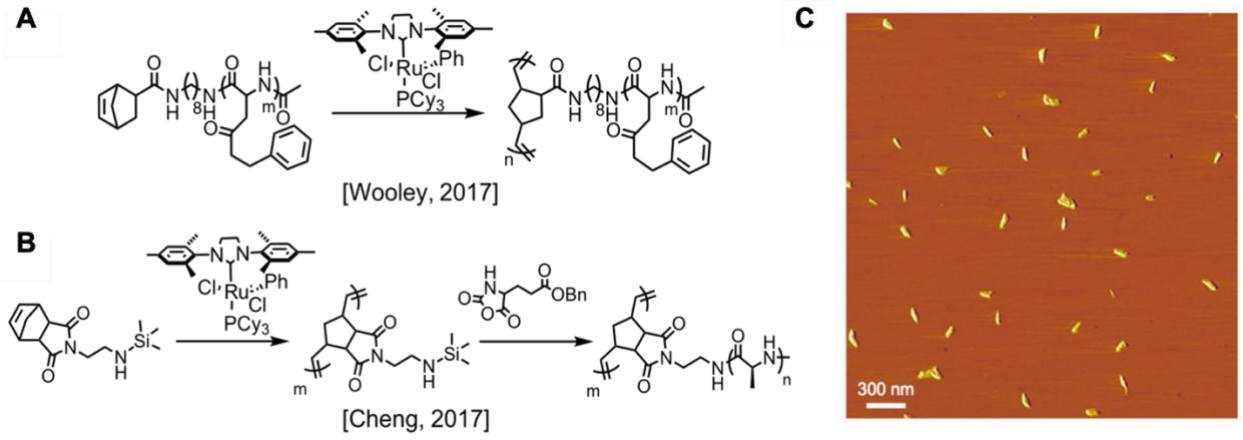


**Figure 1.2** Recent examples of peptide polymers employing dual polymerization strategies. (A) Graft-through polymerization reactions utilizing polypeptide monomers prepared via NCA ROP. (B) A graft-from strategy towards polypeptide brushes. (C) AFM data of polymers shown in (B), reveal rigid rod-like structures morphologically reminiscent of the proteoglycan structures (e.g. aggregan), on freshly cleaved mica. Copyright 2020 Wiley-VCH GmBH.[34]

While the versatility of post-polymerization modification methods has enabled the design of sequence defined peptide-brush polymers for several biological applications,[35-40] functional group-tolerant polymerization techniques have been exploited to directly polymerize peptide monomers bypassing synthetic and purification steps and yielding the most efficient, defect-free and densely arrayed brushes possible. We propose this as a new class of "polypeptide" where a therapeutic peptide is linked to a hydrophobic core (synthetic polymer), hence displaying active amino acids for recognition and function in a controlled, precise manner. Peptide monomers are polymerized into chains of high density that protect the peptide from degradation and prolong circulation without compromising bioactivity. This platform involves the direct (graft-through) polymerization of peptide-containing monomers via living polymerization methods, notably Ring Opening Metathesis Polymerization (ROMP). We define this type of peptide brush polymer platform as Protein-like Polymer (PLP). In the following chapters, we will discuss the mechanistic properties and new synthetic route of PLPs. In addition, we will explore the potential aspect of PLPs as a novel peptide therapeutics, especially, for the treatment of Huntington's Disease and neovascular age-related macular degeneration (nAMD).

# Chapter 2. pH-Responsive Charge-Conversion Progelator Peptides

This chapter is adapted from the following publication:

Carlini, A.S., Choi, W., McCallum, N. C., Gianneschi, N.C. pH-Responsive Charge-Conversion Progelator Peptides, *Advanced Functional Materials*, **2021**, 2007733.

## 2.1 Introduction

Reversible charge-conversion of proteins and polymers with maleamic acid derivatives has been used to study protein denaturation and folding pathways,[41-43] for structural disassembly of polymer films or colloidal structures,[44, 45] for cellular penetration,[46-48] and for drug release.[49-51] These moieties exhibit acid-triggered amide bond hydrolysis. Furthermore, the pH sensitivity can be tuned for faster responsiveness through increasing bulkiness with aliphatic substitutions onto the alkene backbone.[52, 53] Current strategies with self-assembled hydrogels utilize acidic tissue microenvironments for responsive network degradation and subsequent drug release.[54-56] To our knowledge, this strategy has not been applied to induce macromolecular hydrogel assembly, and thus targeted gelation, from a soluble precursor.

We sought to use charge-conversion chemistry as a facile method for converting inert small molecules into structurally dynamic biomaterial scaffolds at sites of tissue acidosis due to injury (e.g. myocardial ischemia, rheumatoid arthritis, articular cartilage damage, and epidermal wounds).[57, 58] Our design provides a strategy amenable to minimally invasive delivery and stimuli-responsive assembly at sites of inflammation for targeted tissue engineering.

During myocardial ischemia, the local pH drops below physiological conditions (~pH 6.0-6.4),[58, 59] which is caused by a gradual buildup of lactic acid (pKa 3.86) and drop in plasma bicarbonate. Similar drops in pH have been observed in synovial fluid at sites of arthritis or cartilage damage (pH 6.5),[60-62] chronic metabolic acidosis due to liver failure (pH 7.1),[63] and acute (pH 6.5) and chronic (pH 5.4) epidermal wounds.[64] These forms of tissue acidosis can exacerbate inflammation, leading to further tissue damage.[57, 65] Injectable hydrogels seeded with cells/growth factors or as acellular scaffolds have been used for the repair of cardiac tissue after myocardial infarction (MI),[66, 67] articular cartilage damage,[68, 69] burn and epidermal wounds,[70-72] and treatment of arthritic flares from wear and tear.[73, 74] Introduction of these viscoelastic scaffolds provides lubrication or acts to supplement degraded extracellular matrix (ECM), which provides structural support, a niche for cellular anchoring, and biochemical communications.[75-77] Additionally, drug-loaded hydrogels provide a porous network for controlled delivery of encapsulated anti-inflammatories, growth factors, and/or cell therapies.[78, 79]

Unfortunately, these injuries usually have irregular or gradated boundaries, making localized hydrogel delivery difficult. Furthermore, a balance between material spreading and solidification kinetics is a persistent challenge.[80] Excess spreading can cause material diffusion away from target tissue, and rapid gelation can preclude noninvasive delivery strategies or prevent appropriate tissue coverage. The advent of structurally dynamic materials has presented a useful strategy for controlled assembly in response to endogenous stimuli (e.g. pH, temperature, redox chemistry, metal chelation, enzymes, and mechanical stress).[81-86]

As a proof of concept, we modify the well-known KLD-12 self-assembling peptide (SAP). This peptide has already demonstrated utility as a degradable, nonimmunogenic, and nontoxic

hydrogel for tissue engineering.[87-91] However, practical application in the body following traumatic injury is limited by its high viscosity, precluding the use of minimally invasive catheter delivery[86]. Furthermore, lack of stimuli-responsiveness forces this material to assemble at the immediate site of application. We demonstrate that temporary charge-conversion of the self-assembling peptide KLD-12, from zwitterionic (Z=0) to polyanionic (Z=-6) is sufficient to yield soluble and low viscosity progelators. These materials are amenable to minimally invasive catheter delivery, unlike the KLD peptide. Furthermore, they exhibit pH-tunable gelation at physiologically relevant levels during injury-related tissue acidosis.

## 2.2 Results and Discussion

### 2.2.1 Synthesis of Charge-Conversion Progelators

For clinical translation, synthetic simplicity and reproducibility are attractive features for the design of biomaterials in biomedical applications.[92] Also, negatively- as opposed to positively-charged biomaterials, generally possess lower cytotoxicity and resist cellular internalization.[93, 94] Tunable sensitivity of simple nonsubstituted, and mono- and dialkyl- substituted maleamic acids to mildly acidic pH's has been reported through comprehensive NMR studies in the literature.[52, 53] As such, we modified KLD-12 (referred to as KLD control) through the addition of either maleic anhydride, citraconic anhydride, or dimethylmaleic anhydride to yield mal-KLD, cit-KLD, or dma-KLD, respectively (Figure 2.1). The resulting polyanionic peptides persisted as soluble solutions at high concentrations (10 mM) and physiologically relevant conditions (1x DPBS, pH 7.4).

Peptides were lyophilized for storage and rapidly dissolved upon resuspension. Peptide solutions were stable up to 14 days at pH 8-9 at room temperature.

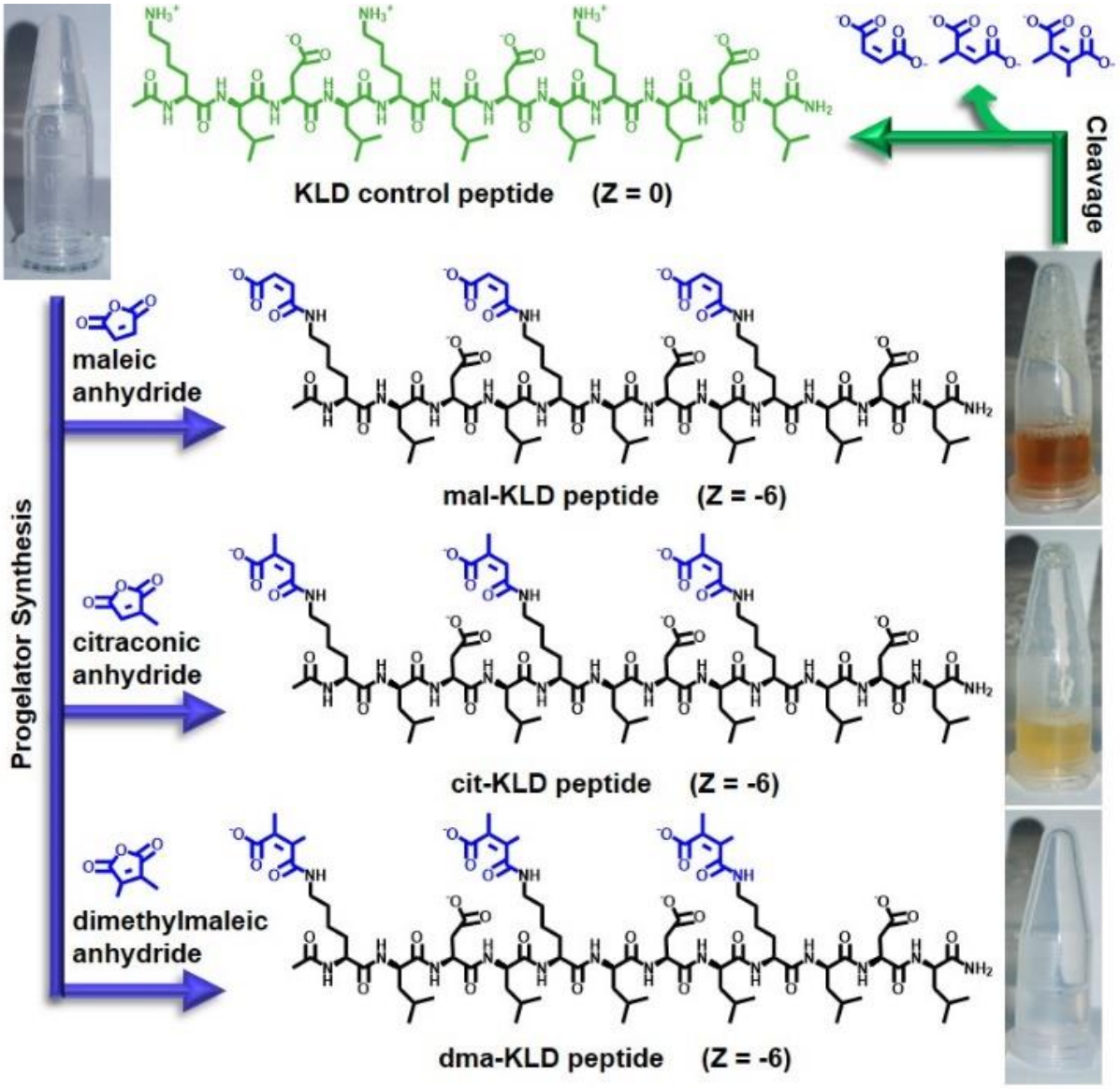


**Figure 2.1** Facile synthesis of peptide progelators. The zwitterionic KLD self-assembling peptide is modified with maleic anhydride, citraconic anhydride, or dimethylmaleic anhydride to generate the polyanionic progelators mal-KLD, cit-KLD, and dma-KLD, respectively. Inset images of

progelators at 10 mM show nonviscous solutions. Acid-treatment regenerates the starting hydrogel material upon release of maleic acid derivatives. Copyright 2021 Wiley-VCH GmBH.[3]

### 2.2.2 Characterization of Progelators with Tunable pH-Sensitivity

Synthesized progelators and KLD control peptide were quantitatively pure by liquid chromatography mass spectrometry (LCMS) and characterized for pH-responsive deprotection (Figure 2.2). $^{1}$H NMR spectra of each progelator in $D_2O$ buffered to pH 7.4 reveals the presence of protons unique to the maleamic acid amides on each progelator, which are absent in the KLD control peptide (Figure 2.2 C). Magnified views of these spectra at pH 7.4 are shown as the bottom traces in Figure 2.2 C, in which changes in the maleamic acid olefin or methyl protons are monitored over time. Upon addition of acidic buffer, a significant upfield shift of olefin protons is observed at 8 min for mal-KLD and cit-KLD, which agrees with anhydride spectra at variable pH values. We note that at pH 3.0, mal-KLD experiences reduced solubility, whereby the starting material olefin protons disappear from this spectrum. This is not observed at higher pH values with cit-KLD and dma-KLD.

Continued amide bond cleavage was monitored in real time up to 720 min for mal-KLD, cit-KLD, and dma-KLD at pH 3.0, 5.5, and 6.5, respectively. Release of capping moieties is denoted by increasing signal for protons c, f, and i. The product olefin protons for mal-KLD and cit-KLD are less deshielded by the absence of the amide pseudo-double bond character.

Importantly, each cleavage buffers was chosen to match the relative product diacid pKa, and thus their peptide activation pH's.[53] This is most notable for the cleavage of dma-KLD which

yields two populations (1.84 and 1.90 ppm) resulting from variable protonation states of the carboxylate. Additionally, protons peaks for d in cit-KLD and g/h in dma-KLD split into two closely spaced populations (d' and h'/g') upon incubation in acidic solution (red traces). NMR provides a useful analysis of the deprotection reactions, however, pH effects on the chemical shifts and overlapping signals from the progelators and resulting cleavage products hamper quantitative analysis.

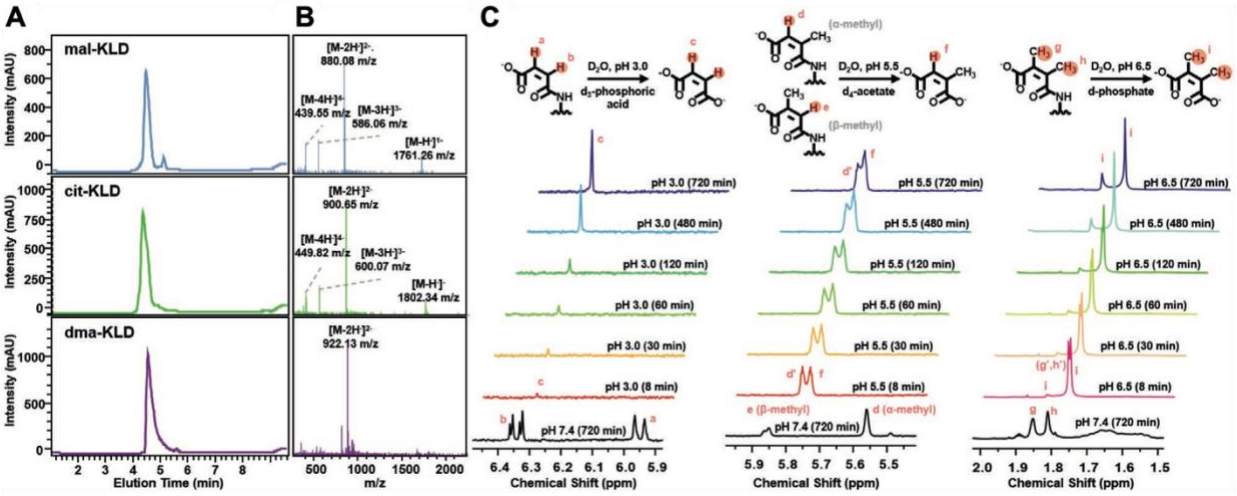


**Figure 2.2** Characterization of progelators by LCMS and pH-responsive deprotection by NMR. (A-C) Liquid chromatography mass spectrometry (LCMS) of mal-KLD, cit-KLD, and dma-KLD. (A) LC spectra show progelator peak (t ~4.5 min) as monitored at 214 nm and (B) corresponding mass spectral patterns with species identities. Spectra show m/z values corresponding to the progelators. (C) Synthetic scheme and 1H NMR spectra of pH-induced deprotection reported as signal intensity vs time at 8, 30, 60, 120, 480, and 720 min. Control spectra of starting progelator at pH 7.4 after 720 min is provided at the bottom in black. Peptides were prepared at 2.5 mg/mL (pH 7.4) or 5 mg/mL (pH 3.0, 5.5, 6.5). Proton identities with apostrophes represent the same peak under acidic conditions. Copyright 2021 Wiley-VCH GmBH.[3]

### 2.2.3 Deprotection of Soluble Progelators Initiates Self-assembly

The synthesis of disperse and fully soluble biomaterials is key for reducing delivery invasiveness. We used circular dichroism (CD) and transmission electron microscopy (TEM) to evaluate secondary structures formed by our peptides in solution before and after pH-responsive charge-conversion (Figure 2.3 and 2.4). All three progelators adopt random coil configurations, as seen by a peak minimum at ~202-205 nm (Figure 2.3). The most hydrophobic progelator, dma-KLD, also absorbed at higher wavelengths indicative of weak intra-strand assembly (Figure 2.3 D). Progelators were treated at pH 3.0 for 24 hr, followed by neutralization to pH 7.4 to recapitulate β-sheet assembly (minimum ~215-218nm) observed with the KLD-12 control peptide (minimum 222 nm). Strong absorbance of maleamic acids in our progelators below 200 nm, leads to near-saturation of the voltage detector. Dialysis of the deprotected solutions to remove maleic acid hydrolysis products yielded nearly identical voltage spectra to that of the KLD control.

Morphology of dilute progelators and pH-induced SAPs was observed with stained dry state TEM (Figure 2.4). Both mal-KLD and cit-KLD progelators exhibited no distinct structures (Figure 2.4 A and B), and dma-KLD showed low contrast staining of disordered structures (Figure 2.4 C), which is likely the result of transient oligomers bound by weak hydrophobic interactions, in agreement with CD results. pH-Induced deprotection of progelators yields elongated fibrillar networks identical to those of the KLD control peptide (Figure 2.4 D).

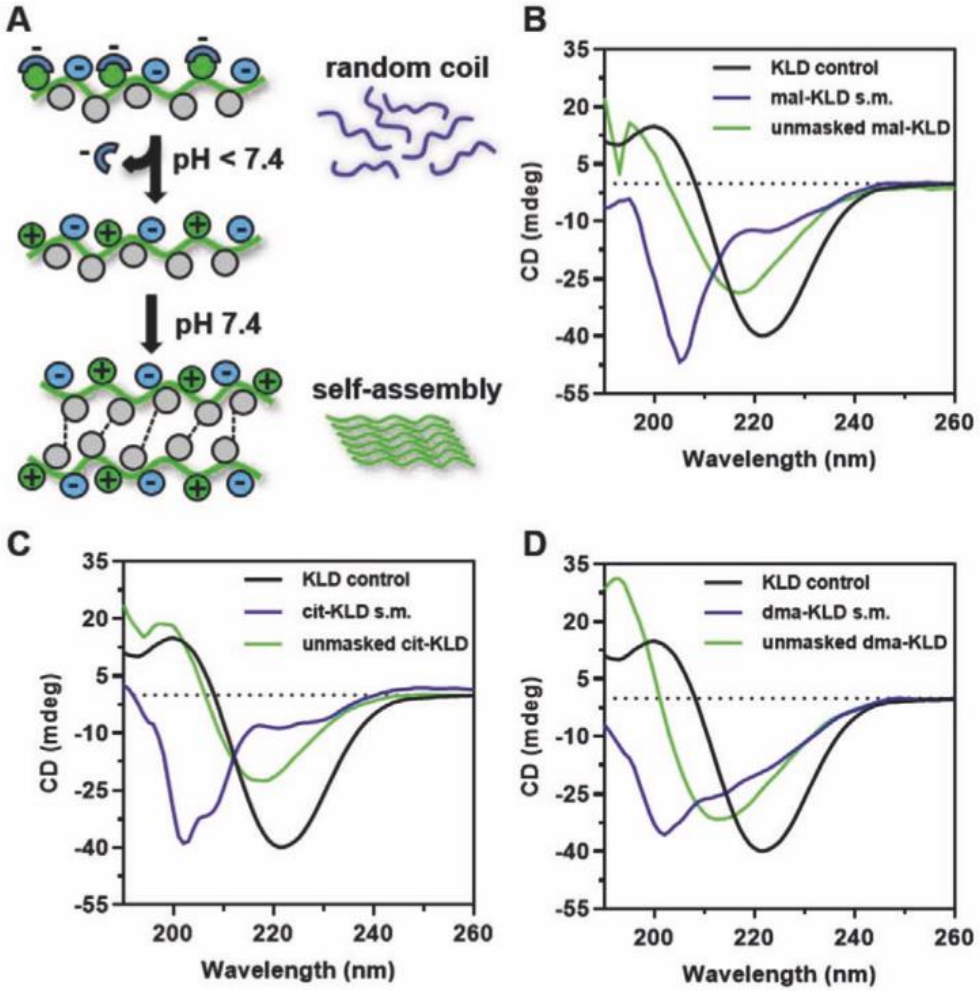


**Figure 2.3** Circular dichroism (CD) and transmission electron microscopy (TEM) analysis of self-assembly. (A) Schematic of polyanionic charge-conversion peptides that persist as random coils. Acid-induced lysine (+) deprotection induces self-assembly via ionic crosslinking (depicted) and hydrophobic interactions into β-sheets. (B-D) Circular dichroism of (B) mal-KLD, (C) cit-KLD, and (D) dma-KLD before and after acid treatment. KLD control peptide is shown for comparison. Progelators incubated at pH 3.0 for 24 hr, then dialyzed into 50 mM phosphate buffer (pH 7.4) for measurement at 400 μM peptide. Copyright 2021 Wiley-VCH GmBH.[3]

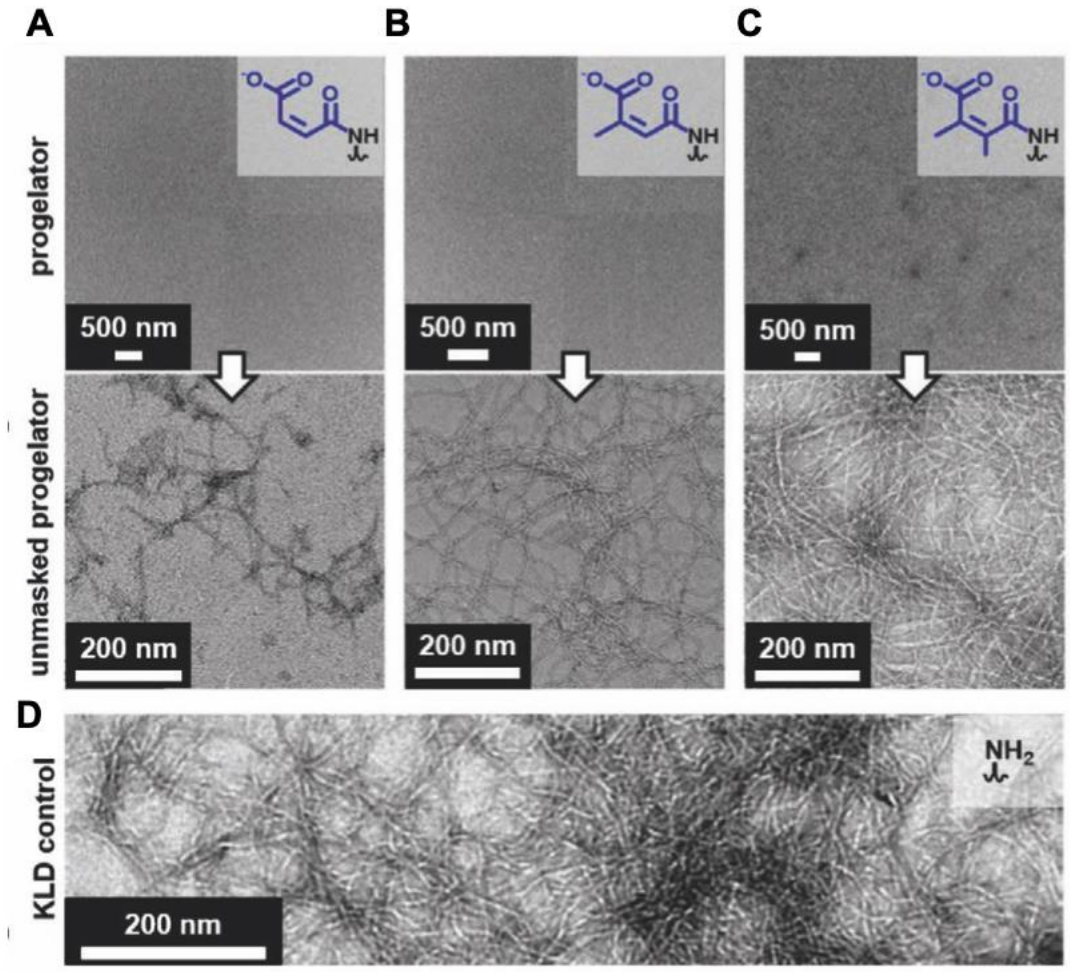


**Figure 2.4** Dry state, stained TEM micrographs of progelators and acid-treated SAPs. (A) mal-KLD, (B) cit-KLD, and (C) dma-KLD progelators with inset chemical structures of maleamic acids before (top) and after (bottom) acid treatment. (D) KLD control with inset chemical structure of deprotected lysine amine. TEM samples (100 μM) were treated at pH 3.0 for 12 hr, then neutralized to pH 7.4 prior to imaging. Copyright 2021 Wiley-VCH GmBH.[3]

### 2.2.4 Bulk Scale Deprotection Induces Significant Viscoelastic Changes

The KLD-12 peptide is a viscoelastic, physical hydrogel with rehealable properties.[95] We therefore, conducted tests to determine whether complete deprotection of our progelators could recapitulate native gelling behavior. Peptides were incubated at pH 7.4, 6.8, 5.5, and 3.0 for up to 24 hr, then neutralized for rheological measurements (Figure 2.5). Bulk samples show solid hydrogels, similar to the KLD control following acid-treatment (Figure 2.5 A). Incomplete deprotection or potential trapping of the maleic and citraconic acid products is suspected to cause the residual absorbance in the visible spectrum. Resulting solutions for all acid-treated progelators reveal viscoelastic hydrogels with storage moduli (G') greater than (G'') (Figure 2.5 B). Strain sweeps confirm that measurements are appropriately measured within the linear viscoelastic region (LVR). Acid-triggered hydrogelation induces frequency independent viscoelastic properties, indicating that self-assembled gels resist flowing over long periods of time. This is a useful property for biomaterial implants.

The sensitivity of each progelator under concentrated conditions, mimicking that of an injected dose, was tested at pH 7.4, 6.8, 5.5, and 3.0 for 24 hr (Figure 2.5 C). Additionally, each progelator was treated for 1 and 12 hr at corresponding acidities tested in Figure 2.2 C, where significant changes to responsiveness for each maleamic acid have been reported.[52, 53] One notable difference, is that pH 6.8 instead of 6.5 was used to test increasingly mild conditions for dma-KLD sensitivity. An increase in storage moduli, G', is observed with increasing acidity and longer treatment times. Furthermore, the stiffest hydrogels were formed by dma-KLD, which possesses the most labile maleamic acid in this study. Indeed, viscoelastic properties for the dma-KLD treated

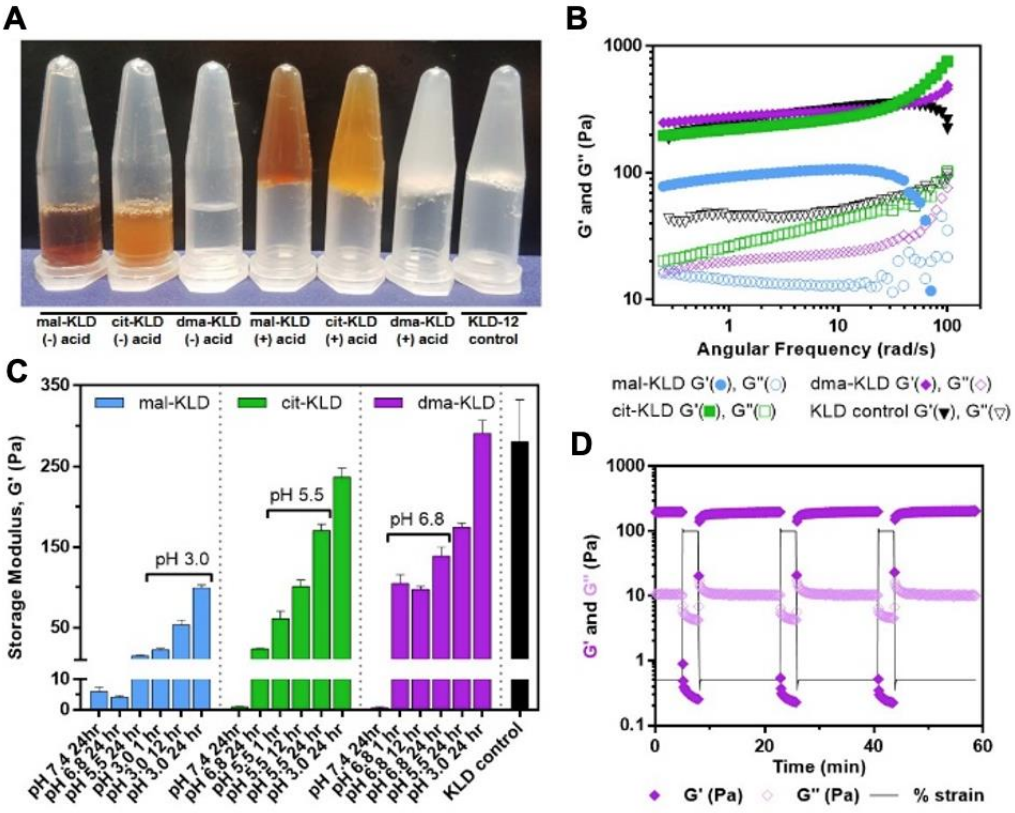


**Figure 2.5** Bulk rheological properties of pH-activated hydrogels. (A) Image of untreated (-) progelator solutions, acid-treated (+) hydrogels, and KLD control. (B) Frequency sweeps of viscoelastic moduli, G' and G'', of KLD control and hydrogels formulated from progelators treated at pH 3.0 for 24 hr. Angular frequency 100-0.25 rad/s, 0.5% strain, n=3 repeats. (C) Storage moduli, G', of peptides treated at pH 7.4, 6.8, 5.5, or 3.0 for 1, 12, or 24 hr. Angular frequency 2.5 rad/s, 0.5% strain. (n=3). Values are mean ± SEM. (D) Representative step-strain oscillations of dma-KLD treated with pH 3.0 for 24 hr demonstrate healing capacity. Angular frequency 2.5 rad/s. Measurements conducted with destructive strain at 100% for 3 min, and then regeneration at 0.5% strain for 15 min (n=3 cycles). All measurements performed on peptide samples that were neutralized and suspended in 1x DPBS (pH 7.4) at 10 mM. Copyright 2021 Wiley-VCH GmBH.[3]

at pH 3.0 for 24 hr resulted in viscoelastic moduli on par with the KLD control, indicative of complete maleamic acid deprotection. ESI of treated dma-KLD gels reveal partial and complete deprotection products. Thus, the dma-KLD responded well at physiologically relevant conditions

observed in mild tissue inflammation. We note that bulk scale cleavage is likely slowed, due to decreased solvent diffusion as macromolecular self-assembly occurs. We also suspect that *in vitro* gelation kinetics may differ from that *in vivo,*[80] as local pH gradients exist in inflamed tissues. Regardless, these experiments confirm gelation sensitivity can be tuned with simple modification of the charge-conversion moiety.

Finally, the capacity for hydrogel healing following excess strain was demonstrated through step-strain oscillations (Figure 2.5 D) in which destructive strain (100 %) was applied to disrupt the hydrogels, resulting in liquid-like solutions with G'<G''. This excess strain was removed, and rapid hydrogel regeneration was observed (crossover G'=G'' occurs within seconds) over several cycles.

### 2.2.5 Low Viscosity Progelators are Amenable to Catheter Injection

Needle-based injections require that materials are shear-thinning. Catheter based injections further require that the material have low enough viscosity to flow through the catheter during delivery, a process which can take up to 1 hr in a clinical setting.[80, 96] Many physical hydrogels are shear-thinning and rehealable, but aging time can vary from different relaxation and interpenetration properties between fractured domains.[97] Alternatively, excess viscosity from reassembly in the catheter can stop material delivery, altogether. A material that gels after delivery can bypass these issues.

As our peptide progelators in 1x DPBS are free-flowing solutions, we tested their utility for catheter-based injection (Figure 2.6). Complex viscosity of the peptides was measured as a function of shear rate (Figure 2.6 A and B). Progelators were over two orders of magnitude lower

in viscosity than the KLD-12 control gelator, as well as shear-thinning. Acid-induced gelation triggered an increase in viscosity. Furthermore, no temperature dependent changes in viscoelastic properties were observed when samples were slowly heated from 21-37 ˚C, representative of the temperature variations generally experienced by biomaterials during catheter delivery. We reasoned that our progelators would be amenable to catheter-based injections.

Progelators in this study demonstrated no resistance to delivery by hand or catheter failure when pumped at clinically relevant rates (0.6 mL/min) (Figure 2.6 C and D), whereas excess viscosity from the KLD-12 control peptide at 10 mM in 1x DPBS caused catheter failure *in vitro.* Thus, we have successfully designed an acid-activatable material for simple formulation and noninvasive delivery. Finally, given the wider inner diameter of clinical over-the-wire infusion catheters (e.g. EmergeTM PTCA, 0.36 mm), we reason that our low viscosity materials are amenable to both transendocardial injection and intracoronary infusion cardiac catheter delivery.

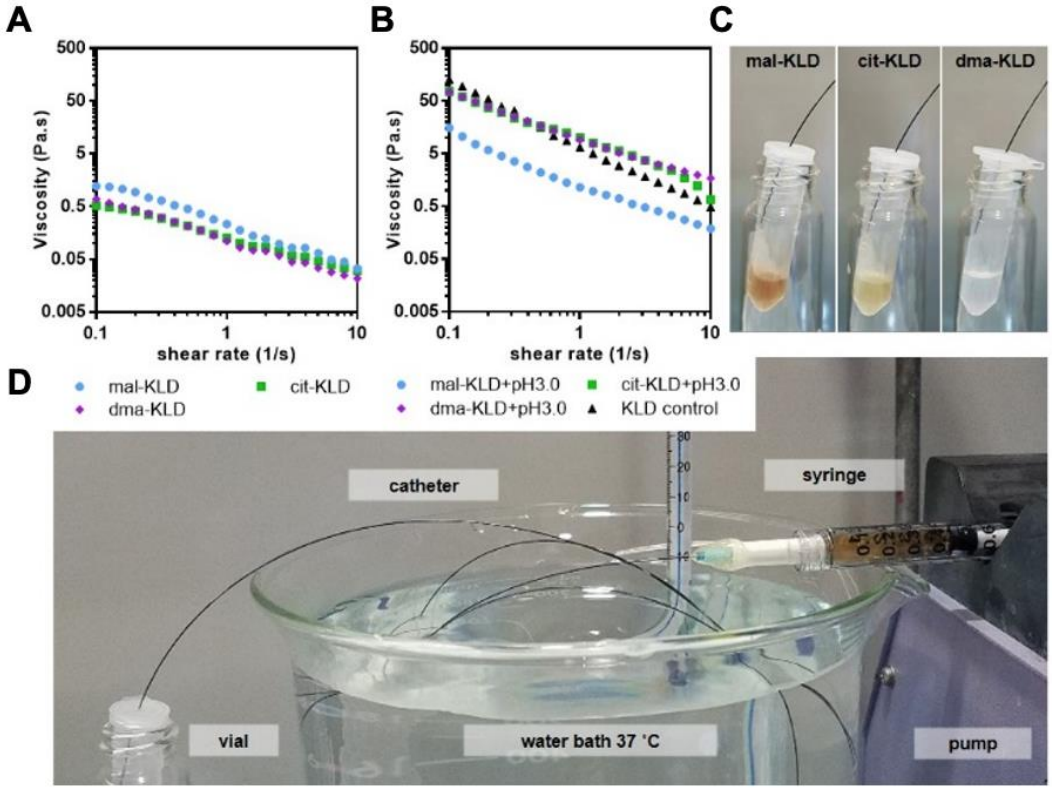


**Figure 2.6** Progelators persist as low viscosity solutions for catheter injection. (A-B) Viscosity of (A) progelator solutions and (B) acid-treated hydrogels. (C) Progelators solutions flow smoothly through the catheter at 0.6 mL/min. (D) Catheter injection setup with loaded syringe pumping progelators through a catheter submerged in a 37 ˚C water bath. Peptides 10 mM in 1x DPBS (pH 7.4). Copyright 2021 Wiley-VCH GmBH.[3]

### 2.2.6 Progelators Are Hemocompatibility In Blood Components.

Lack of hemocompatibility can be a limiting factor for injectable biomaterials, which must demonstrate inert activity within the blood during direct (intravenous injection and catheter infusion) or indirect (subcutaneous and intramuscular injection leakage) contact with the bloodstream.[98, 99] Potential blood interactions may cause thrombosis, induce hemolysis, or alter coagulation kinetics. We incubated our charge-conversion peptides at increasing dosages in whole

human blood components (Figure 2.7). For reference, generous estimates for clinically relevant doses from transendocardial catheter injection and intracoronary infusion are 1;830 and 1:500, respectively. The hemolytic properties of our progelators and the KLD control in isolated red blood cells (RBCs) were assessed for acute toxicity (Figure 2.7 A). Doses up to 1:10 for all peptides revealed <5% hemolysis, which is below the limit for consideration as a nonhemolytic biomaterial.[100]

Activated clotting times (ACT) were used as a general method that encompasses intrinsic and common coagulation pathways to assess thrombogenicity during delivery (Figure 2.7 B). This assay is the preferred test in catheterization labs and cardiac theratres.[101] Anticoagulative properties were observed at 1:100 and 1:10 blood doses for mal-KLD and cit-KLD, and to a much lesser extent at 1:10 with dma-KLD. The KLD control peptide exhibited no significant alteration to normal clotting times over that of the vehicle standard at all doses. In contrast, collagen showed a thrombogenic effect, and chelation of calcium prevented clotting altogether.

Finally, plasma recalcification profiles in platelet poor plasma (PPP) were used to study the intrinsic pathway of clotting, which can reveal adverse blood-biomaterial interactions (Figure 2.7 C and D). Collagen, which activates platelet aggregation, showed no early onset of coagulation in the presence of platelet-poor media (Figure 2.7 C). Glass coverslips, which have negatively charged and hydrophilic surfaces, were used as a positive control of contact activation, whereby coagulation onset time was reduced. As a negative control, PPP without $Ca^{2+}$ showed no onset of coagulation. Both mal-KLD and cit-KLD exhibited earlier onset times and marked decrease in extents of coagulation (Figure 2.7 D). Furthermore, cit-KLD caused a faster rate of coagulation than that of the other peptides. However, dma-KLD and KLD control peptides exhibited minimal

deviation from vehicle standard coagulation profiles, with no significant difference between each other at all doses.

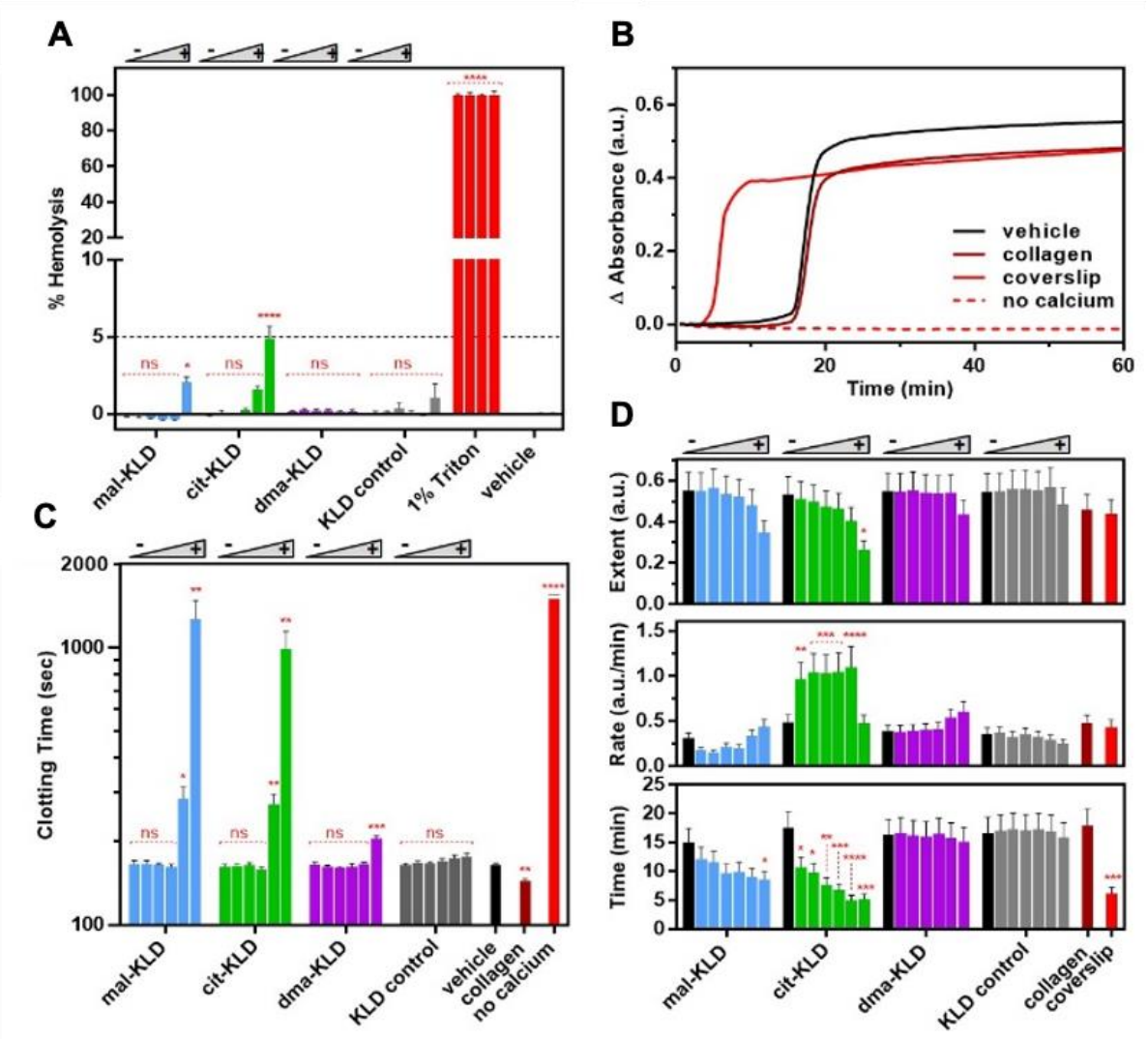


**Figure 2.7** Hemocompatibility of peptide progelators. (A) Percent hemolysis of human red blood cells (RBCs) after incubation with different concentrations of peptide for 1 hr. Inset line defines the threshold for hemolytic response (> 5%). (n=6) (B) Activated clotting times of whole human blood in the presence of different peptide concentrations. (n=5) (C) Plasma recalcification profiles in platelet poor plasma (PPP) for vehicle standard, and collagen, glass coverslip, and no calcium controls. (n=6) (D) Measurements of coagulation maximal extent, rate, and onset time from plasma recalcification profiles as a function of peptide concentrations. (n=6) All peptide dilutions in

biological fluid at 37 ˚C are provided in figures at increasing peptide in blood concentration from 1:10,000, 1:5000, 1:1000, 1:500, 1:100, and 1:10 volume ratios, given an injection concentration of 10 mM stock solution in 1x DPBS. *ns ($p > 0.05$), * ($p \leq 0.05$), ** ($p \leq 0.01$), *** ($p \leq 0.001$), and **** ($p \leq 0.0001$)*. Values are mean ± SEM. Copyright 2021 Wiley-VCH GmBH.[3]

### 2.2.7 Cell Viability of Progelators and Deprotection Products

Once the peptide has reached its intended acidic tissue target, deprotected KLD-12 peptide can self-assemble as a local tissue scaffold. This peptide is known to be biocompatible, but the new chemistries presented in this chapter are not. We performed MTT cell viability assays by incubating progelators (mal-KLD, cit-KLD, and dma-KLD) and deprotected caps (maleic, citraconic, and dimethylmaleic acid) with L-929 cells (mouse, subcutaneous connective tissue) to understand their cytotoxicity (Figure 2.8 A and B). No statistical significance was observed between peptides and the vehicle (1x DPBS) up to 1000 μM after 24 hr incubation (Figure 2.8 A). Similarly, deprotected caps studied at stoichiometrically matched concentrations, showed the same result (Figure 2.8 B). In contrast, 10% DMSO exhibited ~19% viability.

### 2.2.8 Self-Assembly Induced Drug Encapsulation of Model Drug

We reason that acid-induced deprotection and simultaneous self-assembly imbues our progelators with the capacity for activatable drug encapsulation. Thioflavin T (ThT) was chosen as a model drug for its fluorogenic capacity to quantitatively detect fiber formation and its stability to acidic pH.[102-105] Serial addition of ThT to KLD control peptide shows a monotonic increase in normalized fluorescence up to 50 μM. Furthermore, serial dilution of KLD in a fixed concentration

of ThT (50 μM) revealed a critical aggregation concentration (CAC) at pH 5.5, 6.8, and 7.4 of 80.0 (± 3.1) μM peptide. Incubation for 10 min of progelators (500 μM) above their CAC in buffers at associated activation pH values in Figure 2.5 C reveal fluorogenic turn-on as ThT (50 μM) is incorporated into the growing networks (Figure 2.8 C). Finally, coincubation of the solvatochromatic dye, Congo Red, with progelator provides a visual demonstration of small molecule sequestration. We envision that self-assembly induced encapsulation of therapeutics can provide a facile strategy for localizing treatment through simple co-delivery.

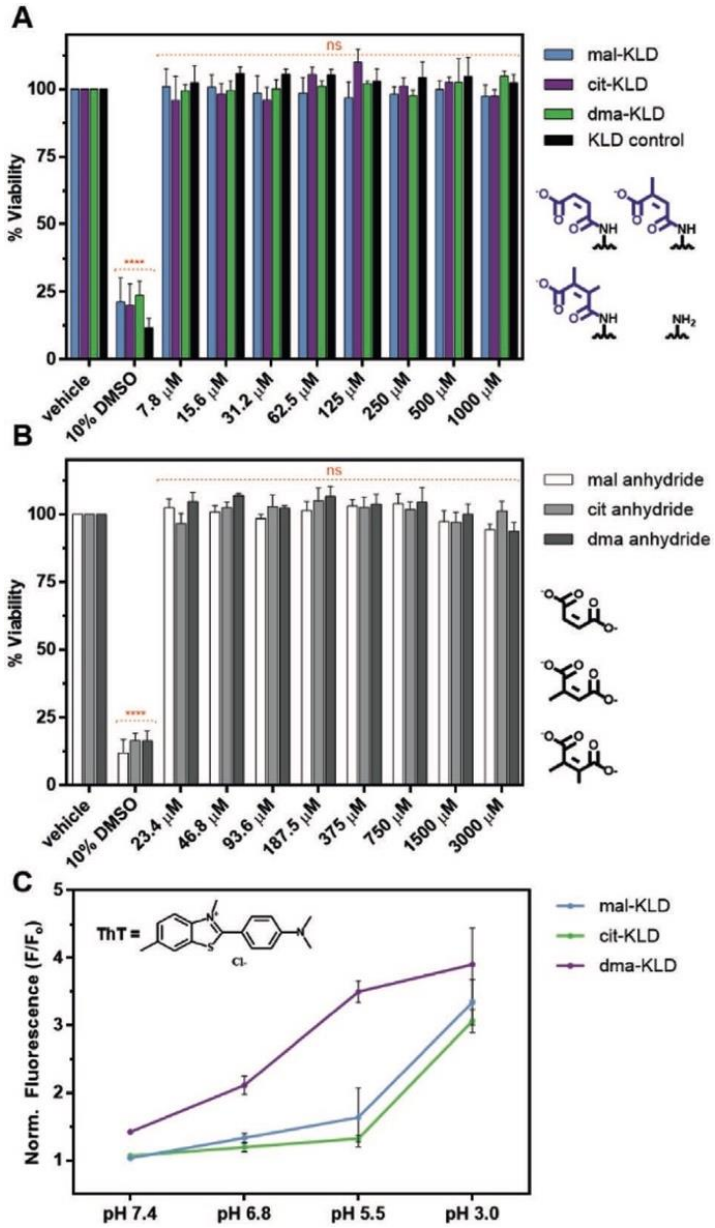


**Figure 2.8** Cell viability of progelator components and drug encapsulation. (A) Cell viability of mal-KLD, cit-KLD, dma-KLD, and KLD control incubated at 0, 7.8 15.6, 31.2, 62.5, 125, 250, 500, and 1000 μM peptide in 1x DPBS (pH 7.4). (n=3) (B) Cell viability of mal anhydride, cit anhydride, and dma anhydride incubated at 0, 23.4, 46.8, 93.6, 187.5, 375, 750, 1500, and 3000 μM in 1x DPBS (pH 7.4) (n=3). (C) Encapsulation of model drug into fiber network. Normalized fluorescence ($F/F_o$) of ThT (50 μM) and progelator (500 μM) after incubation at pH 7.4 6.8, 5.5, and 3.0 for 10 min. (n=4). Values are mean ± SEM. Inset chemical structure of ThT. Copyright 2021 Wiley-VCH GmBH.[3]

## 2.3 Conclusion

There is a need for synthetically simple tissue engineering scaffolds that can be delivered non-invasively to injury sites. In many extreme cases, inflammation is not localized (e.g. arthritis, myocardial ischemia, traumatic injury), so single injections of a preformed hydrogel to the site of interest may not be practical. Our design strategy enables a stimuli-responsive solution that flows freely until activated by inflammation-associated extracellular acidosis.

We present a simplistic approach to reversible modification of a self-assembling peptide using a one-step synthesis with quantitative yields. The pH-sensitivity of these progelators is readily tuned with substituted maleamic acid moieties, enabling assembly at physiologically relevant tissue acidities (pH ~ranging from 5.4-7.1). Thus, our platform utilizes unique advantages of both soluble small molecules (injectability and tissue perfusion) and macromolecular hydrogels (stationary support, prolonged retention, and drug encapsulation).

We reason that our materials have the capacity to spread unhindered until activated by the acidic extracellular microenvironment of inflamed tissue. This structurally dynamic behavior is especially useful in wound-healing applications where the *in vivo* architectures are tortuous, and in some instances require navigation through narrow pathways prior to self-assembly as a stationary hydrogel. A distinct advantage that many soft injectable hydrogels have is the capacity to repeatedly heal after strain-induced network disassembly. We showed that our acid-treated progelators were able to recapitulate this important property as well as increased spreading resistance during solidification.

Both mal-KLD and cit-KLD progelators exhibit significant anticoagulative properties, whereas dma-KLD dosing was nearly indistinguishable from that of hemocompatible KLD control peptide. The extent of coagulation for dma-KLD was only altered at the highest dose (1:10 peptide:blood), which indicates that local high concentrations of peptide have a minor anticoagulative effect on the intrinsic coagulation (contact-based) pathway. It is important to note that the two highest blood doses (1:10 and 1:100) are higher than would theoretically be present in the blood after 1 min of circulation, and assumes all material entered into the bloodstream and not the intended tissue. We therefore reason that maleamic acid modified peptides induce no relevant impact on hemocompatibility. Finally, a general trend presented itself as improved hemocompatibility with increasing progelator hydrophobicity in all clotting and coagulation assays. Additionally, no cytotoxicity was observed with RBCs or L-929 cells.

Finally, we provide a simple strategy for targeted drug accumulation without the need for complex synthetic modifications, as activation of peptide self-assembly was shown to trap a model drug in the hydrogel network. Ultimately, co-injection of progelators with any number of therapeutics (e.g. small drugs, growth factors, cell therapies) could allow for targeted accumulation and localized drug release from a stationary scaffold. This work provides a glimpse into the future of tissue engineering with simple chemistries that exhibit complex behavior.

## 2.4 Experimental Details

### 2.4.1 KLD Control Peptide Synthesis

KLD control peptide was synthesized by standard Fmoc SPPS in an AAPPTec Focus XC peptide synthesizer on rink amide MBHA resin. HBTU (N,N,N′,N′-tetramethyl-O-(1H-benzotriazol-1-yl) uronium hexafluorophosphate) was used as the general coupling agent. Each coupling step involved incubation of Fmoc-protected amino acid (3 eq), HBTU (98 mol%, 2.94 eq), and DIPEA (6 eq) in DMF (15 mL) for 2 hr. The N-terminal amine was masked with an acetyl group by incubating acetic anhydride (30 eq) and DIPEA (30 eq) in DMF (10 mL) for 15 min. Peptide cleavage and deprotection was performed in 95:2.5:2.5 (%v/v) trifluoroacetic acid (TFA), triisopropyl silane (TIPS), and H2O, respectively, for 2 hr. TFA was removed from the filtrate via rotary evaporation and the remaining residue was precipitated with cold, anhydrous diethyl ether (3x) and sonication to yield a white solid product.

### 2.4.2 KLD Control Peptide Purification

KLD control peptide was prepared for purification in 5:20:75 acetic acid/water (0.1% TFA)/ acetonitrile (0.1% TFA) via initial dissolution in acetic acid with sonication, followed by addition of acetonitrile then water (final concentration 10 mg/mL). The peptide was purified on a Jupiter Proteo90A Phenomenex column (2050 x 25.0 mm) on an Armen Glider CPC preparatory phase HPLC to yield 95% purity. KLD control peptide was purified using an acidic mobile phase consisting of H2O with 0.1% TFA (Buffer A) and acetonitrile with 0.1% TFA (Buffer B). Gradient:

20-40% over 43 min at 214 nm. KLD control peptide was dialyzed into basic H2O (pH 8-9) prior to lyophilization.

### 2.4.3 Progelator Peptide Synthesis

Charge-conversion peptide progelators, mal-KLD, cit-KLD, and dma-KLD were synthesized in a one-pot step. To a solution of pure KLD control peptide in DMF (40 mg/mL) was added maleic, citraconic, or dimethylmaleic anhydride (30 eq), and dimethylaminopyridine (DMAP) (30 eq). The reaction was stirred 48 hr to yield a black (mal-KLD) or brown (cit-KLD) solution or white precipitate (dma-KLD). mal-KLD and cit-KLD were precipitated with anhydrous diethyl ether (2x) to yield brown and pale-yellow powders, respectively. The dma- KLD reactions were decanted and washed with anhydrous diethyl ether (2x) to yield a white powder. We suspect that observed coloration with mal-KLD and cit-KLD is caused by intramolecular charge transfer complexes between the maleamic acid amide protons with carboxylic acids on the peptide, which increases the molar absorptivity and lowers the absorbance energy barrier. Increased steric hinderance with pendant methyl groups likely limits this interaction leading to decreased sample coloration. Dry peptides were dissolved into basic $H_2O$ (pH 10) and dialyzed into $H_2O$ at pH 8 with 1 kDa cut-off dialysis tubes for 24 hr prior to lyophilization. This procedure yields quantitatively pure peptide and requires no additional purification steps. Peptides were lyophilized for prolonged storage. All stock solutions of progelator peptides were freshly prepared by

reconstitution of lyophilized powder into 1x DPBS (pH 7.4) and sterilized through a 0.2 μm PES filter.

### 2.4.4 Peptide Purity and Mass Spectrometric Characterization

General mass spectra were analyzed on a Bruker AmaZon SL quadrupole ion trap mass analyzer configured with an electrospray ionization (ESI) source. Peptide purity was analyzed via LCMS on a Bruker AmaZon X, which couples an Agilent 1200 Series LC system with a quadrupole ion trap mass analyzer configured with an electrospray ionization (ESI) source. The mal-KLD, cit-KLD, and dma-KLD progelator peptides were run on a Thermo ScientificTM HyPURITYTM C18 HPLC column (3μm particle size), using a slightly basic mobile phase consisting of 0.05% (v/v) $NH_4OH$ in $H_2O$, pH 8 (Buffer A) and acetonitrile (Buffer B). Gradient: 0-30% over 10 min at 214 nm.

### 2.4.5 NMR of Cleavage Kinetics at pH 3.0, 5.5, 6.5 and 7.4

$^1$H NMR control spectra under neutral conditions (pH 7.4) were collected on a Bruker Neo 600 MHz system. Each spectrum was collected as the sum of 16 scans at 298 K. H NMR spectra for kinetic assays under acidic conditions (pH 3.0-6.5) were collected on a 400 MHz Bruker Avance III HD Nanobay system equipped with SampleXpress autosampler. Each spectrum was collected as the sum of 256 scans at 298 K. Buffer stock solutions were prepared as 1M solutions of $d_3$-phosphoric acid (pH 3.0), $d_4$-acetate (pH 5.5), or d-phosphate (pH 6.5 and pH 7.4) in deuterium oxide ($D_2O$) with LiCl (2M) as a chaotropic salt to limit hydrogen bonding of peptides.

Peptides in acidic buffer were pre-dissolved in $D_2O$ with 0.1% NaOD, then diluted 5-fold with buffer stock to generate peptide (5 mg/mL) in either neutral buffer (200 mM buffer, 100 mM LiCl, $H_2O/D_2O$ cosolvent) or acidic cleavage buffer (200 mM buffer, 400 mM LiCl, $D_2O$) solutions. Water suppression was applied for $H_2O/D_2O$ cosolvent conditions. For time course analyses, spectra were recorded at 8, 30, 60, 120, 480, and 720 min after incubation of buffering agent. Spectra were referenced against HOD δ 4.790 ppm.

### 2.4.6 Circular Dichroism (CD) of Peptides

Progelator peptides were incubated for 24 hr at pH 3.0 to unmask lysine residues and dialyzed into $H_2O$ at pH 7 to neutralize and remove excess salt, buffer, and maleic acids. Peptides were lyophilized and re-dissolved at 400 μM in 50 mM phosphate buffer (pH 7.4). Secondary structure of peptide progelators before and after acid treatment were measured on a JASCO 815 Circular Dichroism Spectropolarimeter using the following settings: temperature = 21℃, pathlength = 2mm, scanning speed = 50 nm/min, response time = 2 s, bandwidth = 1 nm, accumulations = 3, and scan range=260-190 nm. Spectra are presented as an average of all accumulations.

### 2.4.7 Transmission electron microscopy (TEM)

Formvar/Carbon-coated 400 mesh Cu grids (Ted Pella, Inc.) were glow discharged for 90 s and spotted with 5 μL peptide sample (100 μM) and set for 5 min. Grids were rinsed with distilled H2O (5 drops), stained with 1% (w/w) uranyl acetate (3 drops), and wicked dry with filter paper. TEM images were acquired on a FEI Tecnai G2 Sphera TEM or Joel ARM200CF Aberration-

Corrected TEM at 200 kV. Acid-treated samples were prepared by incubated at pH 3.0 for 12 hr followed by neutralization.

### 2.4.8 Rheology of Bulk Peptide Solutions at Various Extents of Unmasking

KLD control hydrogel was suspended at 10 mM in 1x DPBS (pH 7.4). Peptide progelators were dissolved at 13.9 mM peptide in $H_2O$ at pH 8.0 and diluted with 5x stock solutions of glycine buffer (1M, pH 3.0), acetate buffer (1M, pH 5.5), or phosphate buffer (1M, pH 6.8 and 7.4) to initiate cleavage (peptide concentration 11.1 mM and buffer concentration 200 mM). Solutions were vortexed for 20 sec, then incubated at 37 °C for 1, 12, or 24 hr. Resulting gels were neutralized with concentrated NaOH and diluted with 10x DPBS to a final concentration of 10 mM for rheological measurements.

All peptide samples were prepared at 10 mM peptide. Viscous and viscoelastic properties were assessed using a stress-controlled rheometer (Anton Paar MCR 302) equipped with a 25 mm diameter parallel plate geometry (PP25). Unless otherwise stated all measurements were taken at an angular frequency of 2.5 rad/s, strain of 0.5%, and temperature of 37 °C. Measurements were performed with a gap height of 1000 μm. To prevent water evaporation, mineral oil was wrapped around the edge of the geometry at the air-sample interface. For viscoelastic measurements the apparatus was used in oscillatory mode. To ensure that measurements were made within the linear viscoelastic regime (LVR), strain sweeps were performed between 0.05-50 % strain at 2.5 rad/s. The dynamic moduli of the hydrogels were measured as a function of angular frequency in the range of 0.25–100 rad/s at a strain of 0.5% (n=3 accumulations). Continuous step-strain oscillations were used to monitor hydrogel healing through disruption (3 min, 100% strain) and

recovery (15 min, 0.5% strain) cycles (n=3). Temperature sweeps were measured by increasing the apparatus temperatures from 21- 40 °C at a ramp rate of 0.5 °C/min. For viscosity measurements the apparatus was used in steady state flow mode. The viscosity of samples was measured as a function of shear rate in the range 0.1–10 s–1 (5% tolerance).

### 2.4.9 In Vitro Catheter Injections of Progelators

In vitro injection of peptide progelators through the 27 G inner Nitinol tubing of a MyoStar catheter was performed, as previously described. Peptide solutions (0.6 mL) were prepared at 10 mM in 1x DPBS (pH 7.4) and loaded into a 1 mL Luer Lock syringe attached to a syringe pump set to a flow rate of 0.6 mL/min. Catheters were inspected for potential clogging during and after injection.

### 2.4.10 Blood Dilutions for Hemocompatibility

Peptide-in-blood dilutions were performed at volume ratios of 1:10000, 1:5000, 1:1000, 1:500, 1:100, and 1:10. These doses indicate peptide dilution in blood given a 10 mM injected dose. Assuming an average cardiac output of 5 L/min at 5 L of blood total, the maximal dosing from a high volume transendocardial catheter injection (6 mL) or intracoronary infusion (10 m) after 1 min of circulation would be 1:830 and 1:500, respectively. This generous estimate assumes that all injected material leaks into the bloodstream and none reaches its intended target tissue. Furthermore, injection via catheter is generally performed over a period of many minutes, which enables further dilution in the blood during delivery.

### 2.4.11 Activated Clotting Time (ACT) Assay with Whole Human Blood

A Hemochron 801 instrument calibrated with an electronic system verification (ESV) device was used to measure activated clotting time (ACT) of whole human blood. Activated clotting times (ACT) were determined using recalcified, citrated whole human blood to minimize variability in starting time points for clotting in all assays. To each Hemochron P214 tube with glass beads was added 4 μL CaCl2 (1.1 M) and 36 μL peptide stock or additive (12.2x final blood concentration). Samples were mixed thoroughly for 30 s to soak the glass beads and incubated for 30 s at 37 °C. Citrated whole human blood (400 μL) was then added (t=0 s), mixed by hand for 10 s, and added to the instrument. Time points at which the magnet was displaced by clot formation were recorded by the instrument. Type I soluble collagen (0.095 mg/mL) was used as a positive control to decrease clotting time. Vehicle (1x DPBS) served as a standard for blood without additive. Samples without calcium, serving as the negative control, exceeded instrument maximum time range (>1500 sec). Each experiment was performed n=5 times with averages and standard error of the mean (SEM) plotted.

### 2.4.12 Hemolysis of Red Blood Cells (RBCs)

Acute toxicity of peptide progelators was measured with an RBC hemolysis assay specific to biomacromolecular drug analysis. RBCs were isolated by centrifugation of 40mL citrated whole human blood at 500 x rcf for 10 min, followed by gentle aspiration of plasma and refilling with 150 mM NaCl solution. After gentle mixing through tube inversion, these steps were repeated 3 x (using 1x DPBS instead of NaCl solution for the last two repeats). To a 49 mL of 1x DPBS (pH

7.4) was added 1 mL of isolated RBCs for a 1:50 dilution. RBCs were lightly agitated prior to use to prevent settling. Briefly, 190 µL of dilute RBCs and 10 µL of peptide stock or additive (20x final concentration) were mixed and added to a clear, flat- bottomed 96-well plate, covered, and incubated at 37 °C for 1 hr. 1% Triton X-100 was used to lyse RBCs as a positive control and untreated vehicle (1x DPBS) was used as a negative control. For each sample, n=6 repeats were prepared. Following incubation, plates were centrifuged at 500 rcf to pellet intact RBCs using a centrifuge equipped with a microplate rotor. Supernatant (100 µL) was transferred to a new 96-well plate, taking care not to disturb the pellet. Absorbance of the supernatant was measured via plate reader at 540 nm (height 7.5 mm, 100 flashes) to detect released hemoglobin from RBC lysis. To calculate % hemolysis, absorbances were corrected for background absorbance from untreated vehicle and then normalized to 1% Triton X-100 treated RBCs to represent 100% hemolysis. %Hemolysis was calculated according to the following equation:

$$\%Hemolysis = \frac{(Abs_{experiemental}) - (Abs_{negative\ control})}{(Abs_{positive\ control}) - (Abs_{negative\ control})}\ x\ 100$$

, where $Abs_{experiemental}$ is the average well absorbance pertaining to RBCs with additive, $Abs_{negative\ control}$ is the average well absorbance for RBCs incubated with vehicle (1x DPBS), and $Abs_{positive\ control}$ is the average well absorbance for RBCs containing 1% Triton X-100. Averages (n=6) and standard error of the mean (SEM) are plotted.

### 2.4.13 Plasma Recalcification Profiles

The intrinsic coagulation pathway was assessed using a plasma recalcification assay. Platelet poor plasma (PPP) was isolated from citrated whole human blood through centrifugation

at 2000 rcf for 10 min and collection of the upper 2/3 layer of PPP. The collected plasma was spun again at 2000 rcf for 10 min and the upper 3/4 layer. Briefly, 100 μL of PPP, 50 μL of peptide stock or additive (4x final concentration), and 50 μL of $CaCl_2$ (50 mM) were added to a clear, flat-bottomed 96-well plate, covered, and loaded into a plate reader incubated at 37 °C for kinetics measurements. Collagen (0.095 mg/mL) which interacts with platelets to decrease coagulation time, was used to confirm proper preparation of PPP to study platelet-independent effects of our peptide. Glass coverslips were used as positive controls for altered coagulation kinetics. Samples without calcium, where no coagulation was observed, served as negative controls. Untreated vehicle (1x DPBS) samples were used as a standard to compare peptide dosing impacts. For each sample, n=6 repeats were conducted. Coagulation profiles were obtained by measuring well absorbance at 540 nm (height 7.0 mm, 100 flashes) at 30 sec intervals for 60 min. Onset to clotting was detected as a sharp increase in sample turbidity. Measurements were all baseline corrected to account for variable turbidity from peptides at different concentrations. The onset of coagulation is indicated by a steep rise in the absorbance vs time curve. A plateau in absorbance was reached within a few minutes and maintained over time, indicating a fully formed, stable clot.

### 2.4.14 Cell Viability of Progelators and Acid-Induced Cleavage Products

The KLD control, progelators, and authentic maleamic acid cleavage products were tested for cytotoxicity in L-929 cells (ATCC). Cells were maintained in EMEM media (ATCC) supplemented with 10% (v/v) horse serum (ATCC), penicillin (100 units/mL) and streptomycin (100 μg/mL) (Mirus Bio), at 37 °C in 5% CO2. Cells were seeded at a density of 4,000 cells per well in clear-bottom, black, 96-well plates for 48 hours prior to incubation. All KLD materials

were stored as lyophilized powder and resuspended immediately prior to use. Stock solutions of peptides (30 mM) and maleic anhydrides (90 mM) were prepared in H2O at pH 8.0. Samples were diluted 1:30 into media to create working solutions at 3 mM with respect to maleamic acid moieties. Working solutions were incubated with L-929 cells at 1:1, 1:2, 1:4, 1:8, 1:16, 1:32, 1:64, and 1:128 dilutions in media for 24 hr. 10% DMSO was used as a positive control for cytotoxicity. The material was removed after 24 hours, and 100 μL of an 80/20 (v/v) mixture of complete growth media to CellTiter-Blue® reagent (Promega) was added to each well and incubated for 1 hour at 37 °C. The fluorescence was measured via plate reader at 590 nm (height 9.5 mm, 75 flashes) and all treatment values were expressed as a percentage of the vehicle (1x DPBS) treated control. Experiments contained 6 replicate wells for each condition and the experiment was performed n=3 times on three separate passages with averages and standard error of the mean (SEM) plotted.

### 2.4.15 Stimuli-Induced Drug Encapsulation with Thioflavin T (ThT) and Congo Red

Thioflavin T and Congo Red were used as fluorogenic and solvatochromatic dyes, respectively, to simulate small molecule drug encapsulation into activated progelator networks. For all experiments, buffers were prepared at pH 3.0 (200 mM glycine-HCl buffer), pH 5.5 (200 mM acetate buffer), pH 6.8 (200 mM phosphate buffer), and pH 7.4 (200 mM phosphate buffer). Fluorescence measurements of ThT were conducted in black, thin-wall 96- well clear-bottom plates with total sample volumes of 100 μL. Spectra were collected at 37℃ with step size of 0.2 nm, 100 flashes, height of 3 mm from bottom, with n=3 accumulations per well. Values were reported as units of F/Fo, where fluorescence signal from ThT + peptide is normalized to fluorescence of ThT only. Absorbance measurements for CR were conducted in clear, 96 well

plates with total sample volumes of 300 μL. Absorbance spectra of CR + peptide solutions were all baseline-corrected to absorbance of the peptide in buffer or buffer only solutions, respectively. Excitation (400-475 nm, λEm = 495 nm) and emission (445-700 nm, λEx = 425 nm) spectra were collected following incubation of ThT (10 μM) with KLD control peptide (1000 μM) at each pH overnight at 37 °C. Values reported as an average of n=3 repeats, in relative fluorescence units (rfu).

Critical aggregation concentrations (CAC) for KLD control were determined by incubating ThT (50 μM) with KLD control peptide (5, 10, 20, 40, 80, 160, 320, or 640 μM) at each pH overnight at 37 °C. Data was reported as normalized fluorescence (F/Fo) with fitted data shown as semi-log lines of normalized fluorescence (F/Fo) with respect to KLD control peptide concentration. The CAC was determined as the intersection of both fits at each pH. Values reported as an average of n=3 repeats.

ThT concentration-dependent signal was determined by incubating variable concentrations of ThT (0 – 100 μM) with KLD control peptide (500 μM) at each pH overnight at 37 °C. Normalized emission spectra (445-700 nm, λEx = 425 nm) were reported as an average of n=3 repeats.

Progelator activation-induced encapsulation of ThT was evaluated by incubation of mal-KLD, cit-KLD, or dma-KLD (500 μM) with ThT (50 μM) at each pH for 10 min at 37 °C, followed by neutralization to pH 7.4. Fluorescence values reported as an average of n=4 repeats. Absorbance spectra of Congo Red were collected following incubation of CR (50 μM) with cit-KLD progelator (500 μM) or KLD control peptide (500 μM) for 1 hr at 37 °C at pH 7.4 or 5.5. Values reported as an average of n=3 repeats.

### 2.4.16 Statistical Analysis

All statistical results are expressed as mean ± standard error (SEM) and all analyses were conducted in Prism. RM one-way ANOVA with multiple comparisons of the mean in each group with that of the vehicle standard was used for analysis of red blood cell (RBC) hemolysis, activated clotting times (ACT), and cell viability. No correction for multiple comparisons (Fisher's LSD test) was performed. Statistics for plasma recalcification profiles were calculated using a "Sigmoidal, 4PL, X is log(concentration)" interpolation function with no handling of outliers and reported with 95% confidence intervals (CI). The Top, HillSlope, and LogIC50 were used as values for coagulation maximal extent, rate, and onset time. Regular two-way ANOVA with multiple comparisons of the mean in each group with that of the standard was used. No correction for multiple comparisons (Fisher's LSD test) was performed. Statistical significance was defined as follows: ns ($p > 0.05$), * ($p \leq 0.05$), ** ($p \leq 0.01$), *** ($p \leq 0.001$), and **** ($p \leq 0.0001$).

# Chapter 3. UV Activable Drug Delivery System with Ultra-high Drug Loading Capacity

This chapter is adapted from the following publication:

Choi, W.†, Battistella, C.†, Gianneschi, N. C. High Efficiency Loading of Micellar Nanoparticles with a Light Switch for Enzyme-induced Rapid Release of Cargo, *Biomaterials Science*, **2021**, 9, 653-657. ("†" denotes authors equally contributed.)

## 3.1 Introduction

Polymeric nanomedicines have the potential to enhance drug solubility and improve selectivity therefore reducing off-target side effects.[106, 107] Such formulations can be designed to hide therapeutics in their core during circulation in the blood stream and deliver it to the desired tissue in a selective and safe manner. Targeting and retention of nanoparticles in the tumor microenvironment (TME) recently emerged as a potential route toward safer delivery of anticancer drugs, immunotherapeutics or combinations.[108-112] However, although TME targeting can enhance selectivity, upon accumulation, nanoparticles mainly remain confined at the edge of the tumor mass, with bigger nanoparticles having lower probabilities to penetrate into the tumor, therefore resulting in low uptake by cancer cells and low treatment efficacy.[113-117] Smaller nanoparticles tends to be more mobile, but are still characterized by low diffusion rates and slow cellular internalization processes as compared to small molecules. This, together with their fast clearance from the TME,[116] makes these formulations less active than the small-molecule counterparts.

Responsive nanoparticles that selectively target the TME and subsequently release the carried anticancer drugs in the TME are a very promising class of drug delivery systems to achieve high safety profiles *via* selective targeting,[117] while maintaining fast drug diffusion, deep tumor penetration, high cellular uptake and therefore optimal treatment outcome. This goal can be achieved by either physical encapsulation or covalent conjugation of the therapeutic of interest into TME-responsive nanoparticles. While physical encapsulation leads to rapid drug release upon particles disruption, this approach can also lead to premature release of therapeutics during storage and blood circulation. Covalent conjugation has received increasing interest owing to the enhanced stability of the formulations as well as the efficient incorporation of diverse drugs at high loadings independently from their hydrophobicity or solvent/polymer affinity. Finally, the possibility to introduce very simple and specific responsive moieties and the implementation of orthogonal linkers offer the opportunity to release drug combinations at different rates and therefore can find application in the most modern combination therapies.[118, 119]

Our laboratory has pioneered a polymeric nanoparticle delivery system that responds to MMPs, which are overexpressed in the TME of many type of cancer,[120 121] to localize and retain nanomaterials within diseased tissues.[122-126] These materials are prepared through the assembly of amphiphilic di-block copolymers to generate spherical micellar nanoparticles. While the therapeutic of interest can be covalently anchored to the hydrophobic block, the hydrophilic portion of the polymer, forming the shell of the micelle, is comprised of MMPs-responsive peptides (Figure 3.1). Enzymatic cleavage of the resulting spherical nanoparticles in the TME results in a transition from small (20-40 nm) spherical nanoparticles to micrometer-scale scaffolds

that are retained in the TME for many weeks, where they can slowly release the loaded therapeutics.[125]

Recently, we demonstrated that this approach can be used to safely target immunotherapeutics to the TME of a 4T1 breast cancer model and slowly release the immunotherapeutic of interest.[126]

However, in the case of anticancer drugs, fast release is generally preferred to maximize intracellular drug concentration and therefore achieve efficacy comparable to that of the free drug. Herein, we developed an MMP-responsive delivery system, in which the model drug 'paclitaxel (PTX)' is conjugated to the polymer backbone *via* a light-sensitive linker (Figure 3.1). Such polymers assemble into inactive micelles (IM) upon solvent switch. Prior use or upon accumulation in the TME, an exogenous trigger such as UV irradiation[127-129] allows PTX release into the micelles hydrophobic pocket and therefore micelles activation. Upon accumulation in the TME, MMPs overexpression can induce morphological switch of the active micelles (AM), followed by burst release of the encapsulated PTX, which is free to diffuse within the tumor mass and penetrate cancer cells efficiently (Figure 3.1). The ability of these nanoparticles to release the drug of interest, while also forming micrometer scale aggregates that are retained in the TME is particularly interesting for combination therapies, where an orthogonal linker can be used to slowly release a second drug from the scaffold and slowly modulate the tumor microenvironment. In this chapter, we describe the synthetic path and demonstrate successful on-demand PTX release upon light activation and enzymatic digestion of active micelles. We investigate nanoparticles morphological transition using multiple imaging techniques and determine PTX activity upon exposure to both endogenous and exogenous triggers in model cancer cell lines.

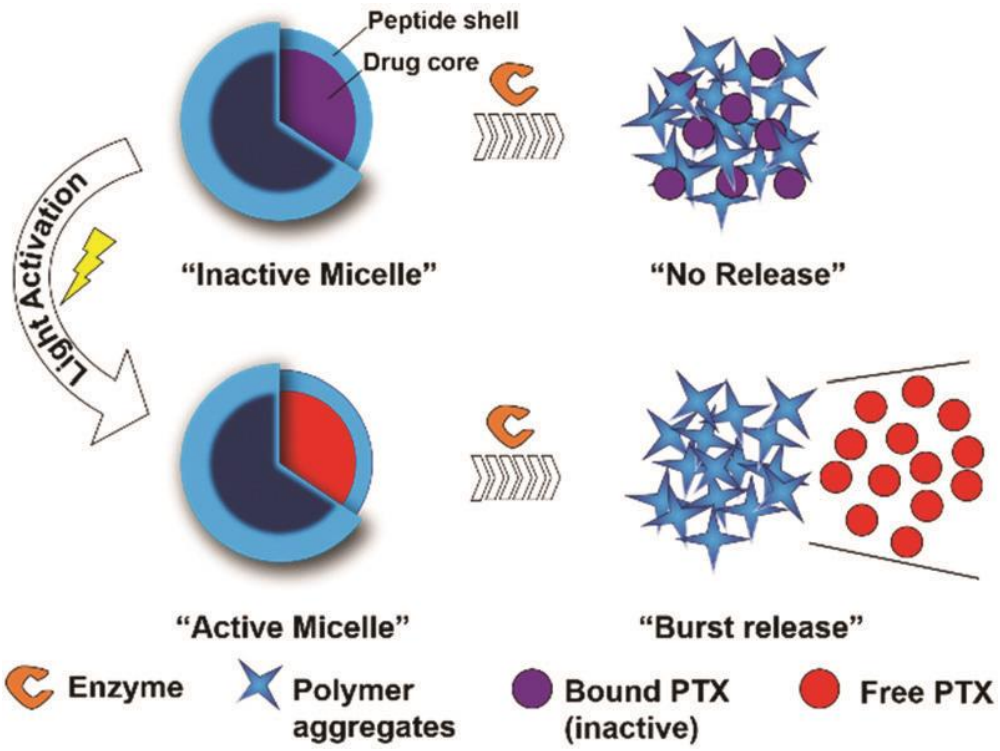


**Figure 3.1** Scheme of light-activable micelle (LAM) for the effective delivery of paclitaxel (PTX) in the tumor microenvironment (TME). Schematic representation of the enzyme-responsive LAM nanoparticles. UV irradiation of inactive micelles (IM) causes PTX cleavage and release into the hydrophobic pocket switching the micelles to active micelles (AM). Cleavage of hydrophilic peptide outer shell by MMP enzymes overexpressed in the tumor microenvironment results in a morphological switch and burst PTX release. Copyright 2020 The Royal Society of Chemistry.[5]

## 3.2 Results and Discussion

### 3.2.1 Synthesis of Light-Activable Block Copolymers

Light-activable block co-polymers (LAP) were designed such that the hydrophobic drug PTX is conjugated to the norbornene monomer *via* the UV-cleavable o-nitrobenzyl ester (ONB) (Figure 3.2 in red).[129-132] The peptide sequence GPLGLAGGERDG was employed as the hydrophilic moiety and as MMP recognition sequence.[126] Ring opening metathesis polymerization (ROMP) was used to polymerize the monomers achieving precise control of the polymer chemistry and subsequent enzymatic response (Figure 3.2). Lengths of the di-block was optimized to obtain stable nanoparticle suspensions that could be stored for several months. An additional monomer containing a NIR Cy5.5 fluorophore (Nor-Cy5.5) was also incorporated at the end of the polymerization allowing imaging of the conformational switch by fluorescence microscopy.[126]

### 3.2.2 Nanoparticle Formation and Enzyme Triggered Morphological Change

Upon polymerization, the resulting polymers were dissolved into DMF and water was added slowly under ultrasonication over a period of a minute. The resulting solution was dialyzed against PBS over two days. Both dynamic light scattering (DLS) and transmission electron microscopy (TEM) (Figure 3.3) confirmed the formation of nano-sized inactive micelle by self-assembly of the block copolymers in Figure 3.1 (Figure 3.3 A and D). Upon 30 min irradiation (365 nm) to cleave PTX from the polymer backbone and release it within the hydrophobic core of the micelles, the generated active micelles (AMs) maintained their spherical shape and comparable size as determined by both DLS and TEM (Figure 3.3 B and E). While Ams maintained their

structure and morphology after UV irradiation (365nm), a change in morphology occurred upon AM treatment with proteolytic enzyme (Figure 3.3 C and F). For these studies, thermolysin was used as a model enzyme as it cleaves in the same position as MMP-9, but is a more robost enzyme for *in vitro* studies.[126]

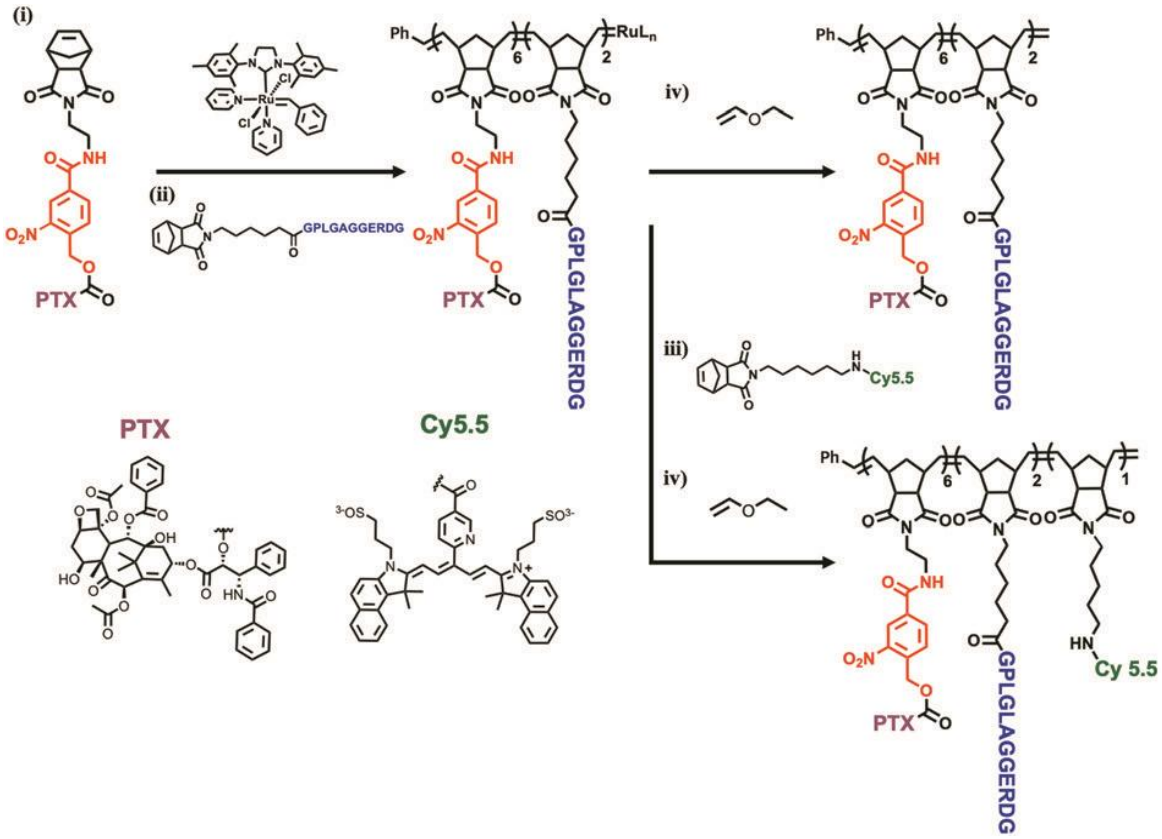


**Figure 3.2** Synthesis of light-activable block copolymers (LAP). Ring-opening metathesis polymerization (ROMP) of functionalized monomers lead to the incorporation of (i) (PTX) linked to the polymer backbone *via* the UV-cleavable linker (red), (ii) MMP-responsive peptide (blue), (iii) NIR fluorescent dye (green). Polymerizations were terminated *via* the addition of (iv) ethyl vinyl ether. Copyright 2020 The Royal Society of Chemistry.[5]

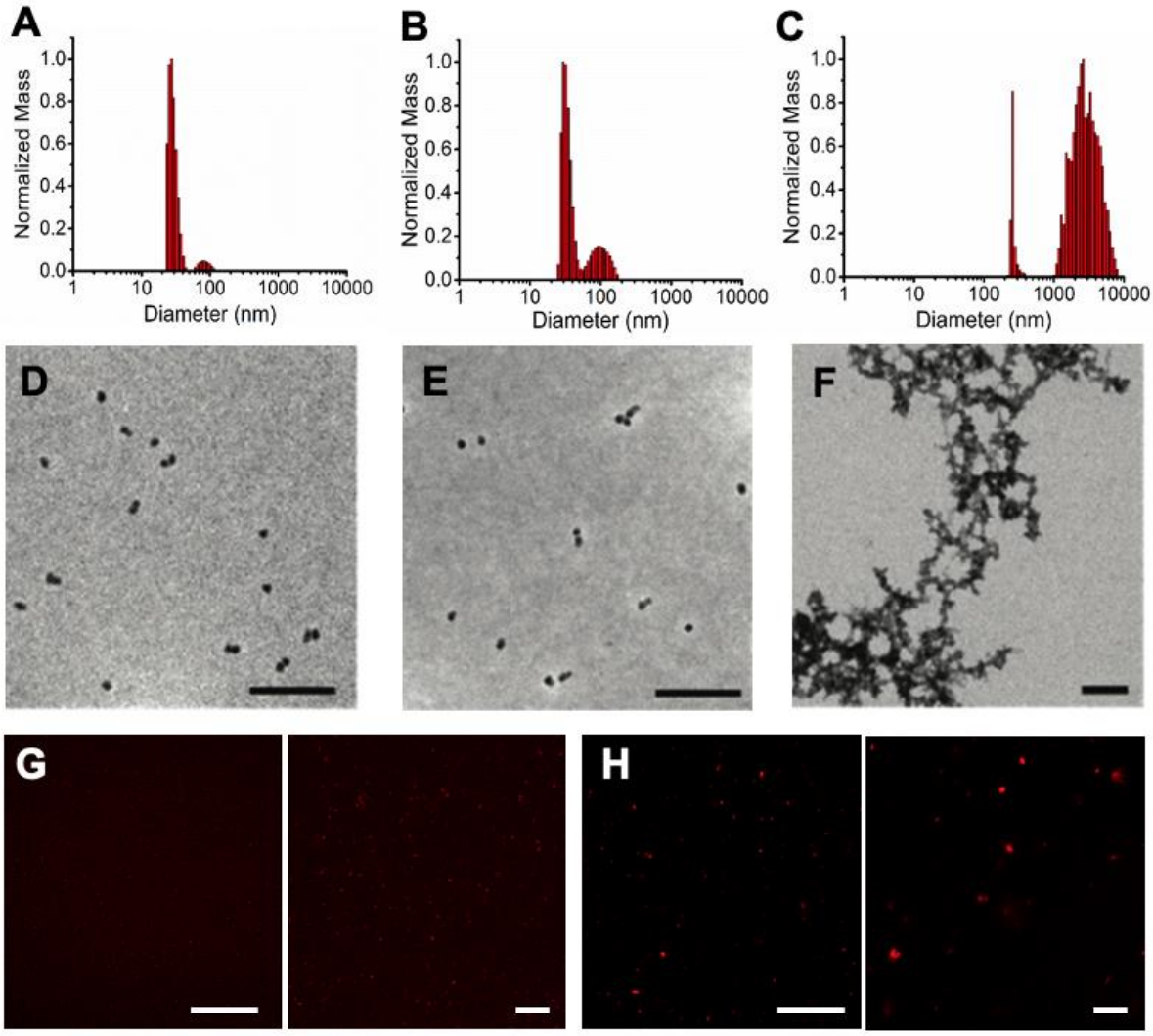


**Figure 3.3** Enzyme-triggered size and morphology switch of LAMs. (A) Size of inactive micelles (IMs), (B) size of active micelles (AMs) before and (C) after 18 h incubation with the model enzyme thermolysin as determined by dynamic light scattering (DLS) measurements. Changes in micelles morphology was investigated *via* both (D-F) dry state transmission electron microscopy (TEM) imaging (scale bars 200 nm), as well as confocal fluorescence microscopy of Cy5.5 labeled micelles in PBS (G) before and (H) after enzymatic cleavage. All settings were kept constant between images. Scale bars 50 µm and 10 µm. Copyright 2020 The Royal Society of Chemistry.[5]

### 3.2.3 Drug Releasement

RP-HPLC analysis (Figure 3.4) confirmed that UV irradiation is required to cleave PTX from the polymer backbone and release it into the AM core. RP-HPLC traces of irradiated AM show a very distinct PTX peak (Figure 3.4 B), also confirmed *via* ESI-MS spectrometry (Figure 3.4 D). In addition, analysis of the filtrate solution upon centrifugal filtration of AMs suggests that UV irradiation did not result in PTX leakage from the AM (Figure 3.4 C).

Efficient micelle disruption and concomitant polymer reorganization upon enzymatic cleavage of the peptide hydrophilic shell was further characterized by fluorescence microscopy of Cy5.5 labeled micelles. Small spherical micelles initially appeared as tiny punctate dots (Figure 3.3 G) and transitioned to microscale fluorescent assemblies upon enzymatic digestion (Figure 3.3 H). This result was further confirmed by the detection of the cleaved peptide fragment in the solution as demonstrated by HPLC and ESI-MS studies. All together these results validate the successful light-induced cleavage of PTX from the polymer backbone and its release and accumulation into the AM core. This represents the first step of a drug delivery strategy where the efficient PTX trapping within hydrophobic pockets is followed by enzyme-directed morphological transition and PTX release.

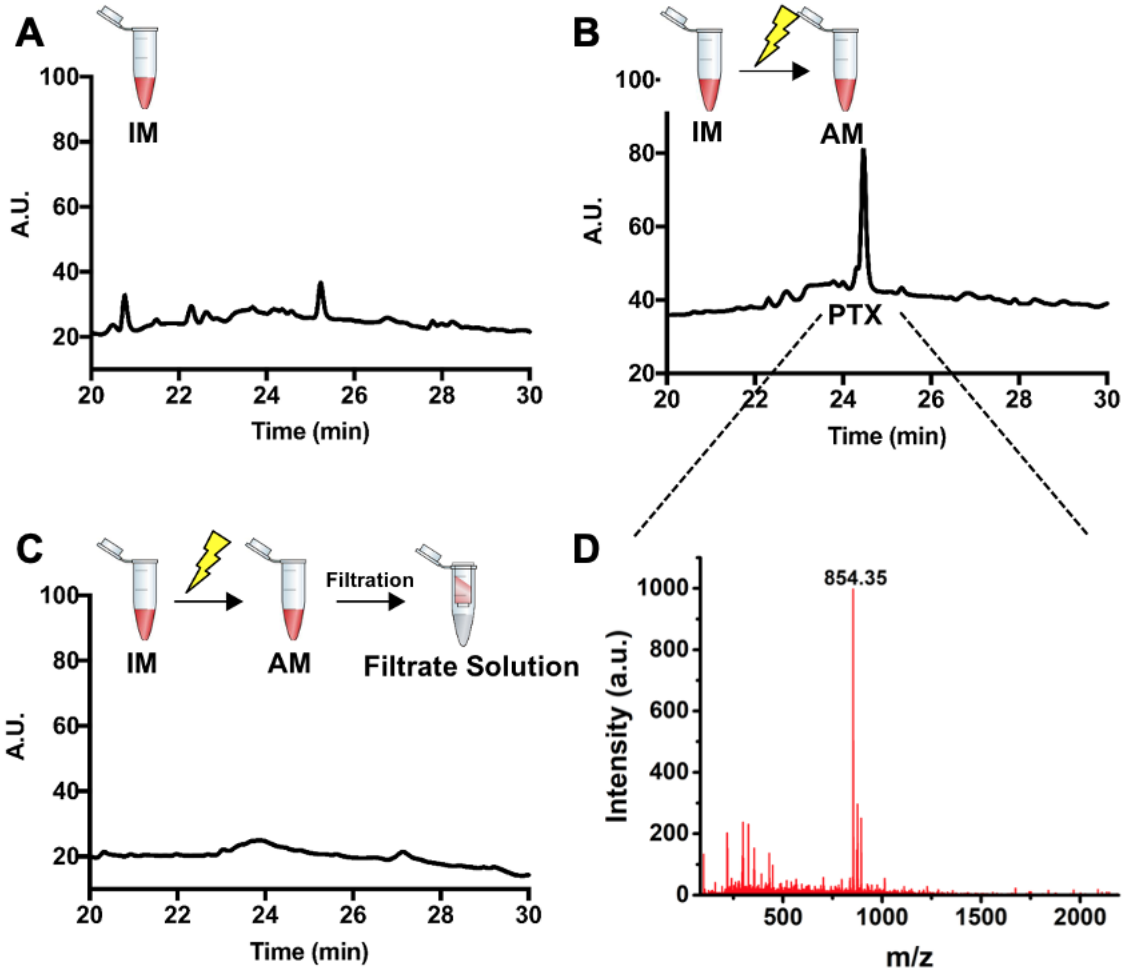


**Figure 3.4** UV irradiation triggers PTX cleavage from the polymer backbone and results in micelles activation. (A) RP-HPLC traces of IMs before and (B) after 30 min UV irradiation at 365 nm (AMs). (C) RP-HPLC traces of the filtrate deriving from AM centrifugal filtration. RP-HPLC gradient: 10 to 80 % acetonitrile in 45 min. (D) ESI-MS spectra of the peak eluted at $R_t$ 24.5 min in the chromatogram reported in (C): PTX $[M+H]^+$ = 854.35. Copyright 2020 The Royal Society of Chemistry.[5]

### 3.2.4 In Vitro Assessment of Light-Activable Micelle in HT1080 cells

To demonstrate the efficacy of such delivery system, *in vitro* activity experiments were performed to evaluate AM cytotoxicity in presence of the enzymatic trigger (Figure 3.5). Efficacy was determined *in vitro via* cell viability assays performed using HT1080 fibrosarcoma cells, which overexpress MMPs and are therefore widely used to evaluate the performance of MMP-responsive drug delivery systems both at the *in vitro* as well as at the *in vivo* level.[113, 123, 133, 134] Ester micelles (EM), in which PTX is covalently conjugated to the hydrophobic portion of the polymer backbone *via* a light stable ester bond were prepared as a control (Figure 3.5 A). Ester bonds have been previously employed to release drugs in a slow and sustained manner.[135] Both control EM and LAM were administered to HT1080 cells either before (inactive micelles, IM) or after light irradiation (active micelles, AM). MMPs released by HT1080 cells into the media was expected to trigger morphological switch of such formulations with consequent PTX release in the case of the light-irradiated AM. Given that MMPs expression within *in vitro* experiments is generally lower than the *in vivo* microenvironments, a positive control in which AM were enzymatically pre-treated was included as a comparison. PTX concentration ranges were selected based on previous studies and polymer concentrations were adjusted based on PTX functionalization.[133] After 72 h, cell viability was determined *via* CTB assay. As expected, while free PTX treatment resulted in a dramatic reduction of cell proliferation already at low nanomolar concentrations, the control EM didn`t show any effect on cell viability for all tested conditions and concentrations, not even upon enzymatic pre-treatment. This result indicates that independently from the formulation (nanoparticle *vs* microscale assembly), the very slow PTX release from

polymer backbone limits its efficacy. On the contrary, UV irradiated AM resulted in lower cell viability, which is comparable to that obtained for cells incubated with free PTX, especially for higher tested concentrations. This effect was also confirmed by analysis of cells incubation with AM that underwent enzymatic pre-treatment.

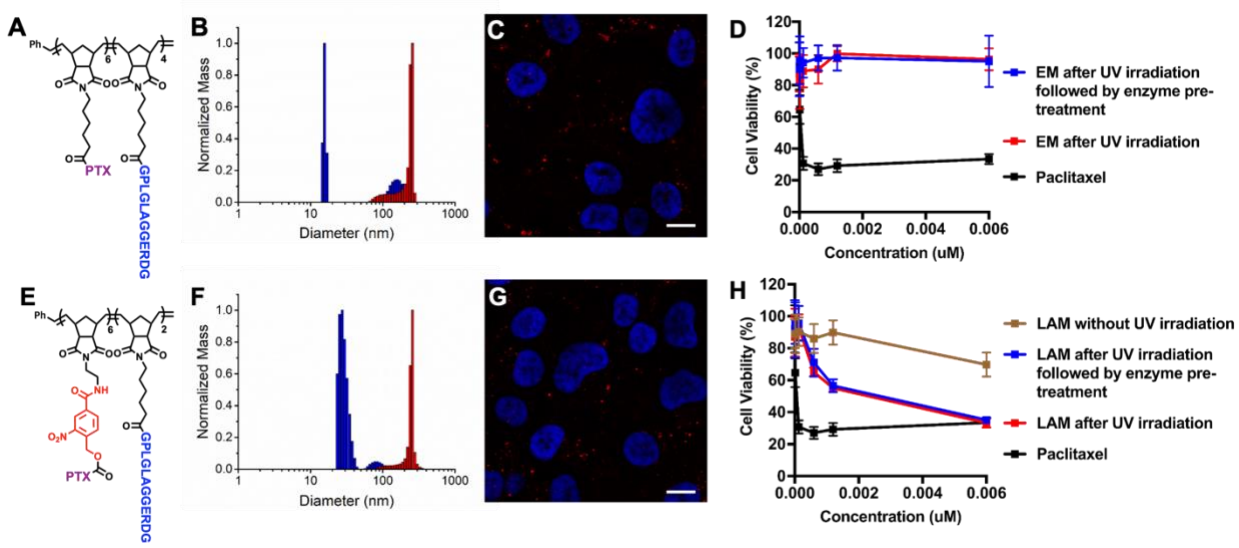


**Figure 3.5** LAMs cytotoxicity in HT1080 cell line is comparable to that of free PTX. (A) Structure of the control ester di-block copolymer (EP) and B) DLS before (blue) and after (red) enzymatic cleavage. (C) Live fluorescence imaging of the resulting Cy 5.5-labeled EMs in cell medium after 24 h incubation with HT-1080 cells. Micelle aggregates are indicated in red (Cy5.5) and the cell nuclei are stained in blue (Hoechst). Scale bars 10 µm. Transmitted light images as well as more examples are reported in Supporting Information. (D) HT1080 cell viability upon treatment with either EMsor free PTX. Cell viability was determined after 72 h *via* Cell Titer Blue (CTB) assay and the reported curves are the result of independent triplicate experiments with each condition performed in triplicate. The same results for LAMs before and after UV or UV and enzymatic degradation are reported in the bottom panel (E-H). Copyright 2020 The Royal Society of Chemistry.[5]

## 3.3 Conclusion

Although active TME targeting can minimize toxicity and side effects arising from conventional cytotoxins treatments, once accumulated into the TME, efficient release of the carried therapeutics is necessary to access deep tumor penetration and efficacy profiles comparable to that of free drug. The ability to synthesize assemblies in which the drug is covalently bound to the polymer backbone in an inactive form, but that undergoes rapid activation and drug release in the TME upon both exogenous and endogenous stimuli is desirable.

*In vitro* analysis of light-activable and MMP-targeted micelles described in this work demonstrated rapid response to both stimuli and efficient morphological transition in presence of MMPs, which effectively impacted the proliferation of the HT1080 fibrosarcoma model cell line. Such constructs can be activated on demand, have the potential to target the TME, can release anticancer drugs quickly and efficiently, which in turn penetrates into the tumor cells and potentially behave as the free small molecule counterparts, locally where cytotoxicity is needed, without perturbing healthy tissues with minimal side effects.

## 3.4 Experimental Details

### 3.4.1 Synthesis of (N-aminoethyl-o-nitrobenzyl)-5-norborene-exo-2,3-dicarboximide (NorENB) conjugated paclitaxel (NorENB-PTX)

(N-4-nitrophenyl ester-4-(hydroxymethyl)-3-nitrobenzoic acid-aminoethyl)-5-norborene-exo-2,3-dicarboximide (4).

(N-4-(hydroxymethyl)-3-nitrobenzoic acid-aminoethyl)-5-norborene-exo-2,3-dicarboximide, 3, was prepared as previously reported.2 4-nitrophenyl chloroformate (125 mg, 0.62 mmol) was slowly added to a solution of 3 (200 mg, 0.52 mmol) in 50 mL THF/pyridine co-solvent in a 100 mL round bottom flask at 0°C in an ice bath. After stirring for 10 minutes at 0 °C, the reaction was stirred for 12 hr at room temperature. Reaction progress was monitored via TLC (5:1 toleuene:diethyl ether, Rf = 0.6). Purification was achieved through extraction with water (1 x 30 mL), followed by 0.5 M HCl (3 x 10 mL), and finally saturated $NaHCO_3$ (3 x 10 mL). The organic phase was dried over $MgSO_4$ and solvent was removed via rotary evaporation followed by purifying with column chromatography (5:1, toleuene:diethyl ether) to give the desired product as a yellow solid.

(N-Paclitaxel ester-4-(hydroxymethyl)-3-nitrobenzyl-aminoethyl)-5-norborene-exo-2,3-dicarboximide (5, NorENB-PTX).

Paclitaxel (225 mg ,0.264 mmol) was added to a solution of 4 (120 mg, 0.22 mmol) and N,N-diisopropylethylamine (46 ul ,0.264 mmol) in 50 mL dry DCM in a 100 mL round bottom flask. The reaction was stirred overnight under N2. Reaction progress was monitored via TLC (1:1 hexane:ethyl acetate, $R_f$ = 0.3). Purification was achieved through extraction with water (1 x 30

mL), followed by 0.5 M HCl (3 x 10 mL), and finally saturated $NaHCO_3$ (3 x 10 mL). The organic phase was dried over $MgSO_4$ and solvent was removed via rotary evaporation followed by purifying with column chromatography (1:1, hexane:ethyl acetate) to give the desired product as a yellow solid. (Yield = 54%)

### 3.4.2 Synthesis of NorAha conjugated MMP-9 responsive peptide (NorAha-GPLGLAGGERDG)

MMP-9 responsive peptide (GPLGLAGGERDG), was synthesized on rink amide resin (loading 0.67 mmol/g) via standard Fmoc-based solid phase peptide synthesis. Fmoc deprotection was performed by agitating resin in 20 % 4-methylpiperidine in DMF for 5 min, draining, and repeating this procedure for another 15 min. Amino acid couplings were carried out for 45 min per amino acid using N,N,N,N',N'-Tetramethyl-O-(1H-benzotriazol-1-yl)uranium hexafluorophosphate (HBTU) and N,N-diisopropylethylamine (DIPEA) (resin/amino acid/HATU/DIPEA 1:3:3:6). Nor-Aha was incorporated at the peptide N-terminus on the resin. Final peptides were cleaved from resin by treatment with trifluoracetic acid (TFA), triisopropyl silane (TIPS), and water (TFA/TIPS/ H2O 9.5% v/v : 2.5% v/v : 2.5% v/v) for 2 hr. Peptides were then precipitated in cold ethyl ether and centrifuged, this procedure was repeated twice. The precipitated peptide products were evaporated in vacuo to give a white crude solid. Peptides were purified by RP-HPLC (20 % to 40 % buffer B over 50 min, retention time = 37 min). ESI MS (mass calculated [M+H]+ =1357.31 m/z; mass observed [M+H]+ = 1356.86 m/z) and lyophilized to afford a pure white solid.

### 3.4.3 Block copolymer synthesis – Light activable polymers (LAPs)

To a stirred solution of NorENB-PTX (25 mg, 19.8 µmol) in dry DMF (2.0 mL), 1.45 mg (2.0 µmol) of catalyst ($(IMesH_2)(C_5H_5N)_2(Cl)_2Ru=CHPh$) was added under N2 atmosphere. The reaction was left to stir under nitrogen for 45 min, after which an aliquot (20 µL) was removed and quenched with ethyl vinyl ether. After 15 min the quenched polymer was precipitated in diethyl ether to give the homopolymer P-$(NorENB\text{-}PTX)_6$ as a white solid which was characterize by SEC-MALS. To the remaining reaction solutions, 8.1 mg (6.0 µmol) of NorAha-GPLGLAGGERDG monomer was added. The mixtures were left to stir under nitrogen for 75 min. After this time, each reaction mixture was split into two portions, half was reacted with ethyl vinyl ether (50 µL) and precipitated in diethyl ether to give the block copolymers P-$(NorENB\text{-}PTX)_6$-$(NorAha\text{-}GPLGLAGGERDG)_2$ as off-white solid. The second solutions were reacted with Nor-Cy5.5 (1.9 mg, 2.0 µmol) for 2 hrs. After this time, ethyl vinyl ether (50 µL) was added to quench the catalyst. After 15 min the solutions were precipitated by dropwise addition to cold anhydrous ethyl ether to give the P-$(NorENB\text{-}PTX)_6$-$(NorAha\text{-}GPLGLAGGERDG)_2$-$(Nor\text{-}Cy5.5)_1$.

### 3.4.4 Synthesis of (N-Cy5.5)-5-norborene-exo-2,3-dicarboximide (Nor-Cy5.5)

25 mg (0.030 mmol) Cy5.5, 11 mg (0.030 mmol) HATU and 62 µL (0.36 mmol) DIPEA were dissolved in 2 mL anhydrous DMF under nitrogen. After 10 minutes, 32 mg (0.12 mmol) N-(hexanediamine)-cis-5-norbornene-exo-2,3-dicarboximide were added and the reaction was stirred overnight. The product was purified by RP-HPLC using a gradient from 40 to 70 % acetonitrile

over 30 minutes (retention time = 30 min). ESI MS (mass calculated $[M+H]^+$ =1063.42 m/z; mass observed $[M+H]^+$ = 1062.99 m/z) and lyophilized to afford a pure white solid.

### 3.4.5 Nanoparticle formulation (LAMs)

Nanoparticles were prepared by sonication method from DMF into DPBS. To this end, a probe sonicator (Fisher scientific) was used at 500 W. 4.2 mg (0.453 μmol) of $(NorENB\text{-}PTX)_6$-$(NorAha\text{-}GPLGLAGGERDG)_2$ and 3.5 mg (0.339 μmol) of $(NorENB\text{-}PTX)_6$-$(NorAha\text{-}GPLGLAGGERDG)_2$-$(Nor\text{-}Cy5.5)_1$ , were dissolved in DMF (7.7 mL, 1 mg/mL). In the case of fluorescent nanoparticles, 60 % (mol) block copolymer without dye and 40 % (mol) block copolymer containing the Cy5.5 dye were dissolved together in DMF. DPBS (7.7 mL) was added dropwise to the polymer solution under sonication over a period of a minute. The solution was left stirring overnight and subsequently dialyzed against DPBS 1X using 3,500 molecular weight cut off (MWCO) SnakeSkin dialysis tubing. The buffer was changed two times per day for 3 days. The nanoparticles were concentrated using EMD Millipore Amiccon Ultra-15 centrifugal filters (10K Nominal Molecular Weight Limit, NMWL) when necessary and filtered through 0.2 μm EMD Millipore sterile filters prior in vitro cell experiments.

### 3.4.6 Enzymatic cleavage of LAMs

LAMs (100 μM, with respect to total peptide) were treated with thermolysin (1 μM) in a total volume of 100 μL for up to 24 hr in DPBS 1X. Experiments were performed at 40 ℃ and at 65 ℃ (optimal reaction temperature for thermolysin). Variation of the nanoparticles size was determined by DLS measurements and the morphological shift was monitored via TEM imaging.

LC-MS studies were performed to detect the cleaved peptide fragment (LAGGERDG) upon enzymatic digestion of the responsive nanoparticles.

### 3.4.7 Synthesis of NorAha conjugated paclitaxel (NorAha-PTX)

To a solution of paclitaxel (100 mg, 117 μmol) and Nor-Aha (38.8 mg, 140 μmol) in 50 mL dry DMF in a 100 mL round bottom flask under $N_2$, was added 4-(dimethylamino)pyridine (1.43 mg, 11.7 μmol). After stirring for 5 minutes at 0°C in an ice bath, *N*,*N*'-dicyclohexylcarbodiimide (26.5 mg, 128.7 μmol) was dripped into the reaction mixture and allowed to stir for 7 hours. Reaction progress was monitored via TLC (1:1 hexane:ethyl acetate, Rf =0.3). The precipitated urea was removed via filtration, and the filter cake was washed with DCM. The solvent was removed via rotary evaporation and the resulting crude product was dissolved in 30 mL $CHCl_3$. Purification was achieved through extraction with water (1 x 30 mL), followed by 0.5 M HCl (3 x 10 mL), and finally saturated $NaHCO_3$ (3 x 10 mL). The organic phase was dried over $MgSO_4$ and solvent removed via rotary evaporation to afford the purified product in 68 % yield solid.

### 3.4.8 Block copolymer synthesis – Ester Polymers (EPs)

To a stirred solution of NorAha-PTX (25 mg, 22.5 μmol) in dry DMF (2.25 mL), 1.64 mg (2.3 μmol) of catalyst ($(IMesH_2)(C5H5N)_2(Cl)_2Ru=CHPh$) was added under N2 atmosphere. The reaction was left to stir under nitrogen for 30 min, after which an aliquot (20 μL) was removed and quenched with ethyl vinyl ether. After 15 min the quenched polymer was precipitated in diethyl ether to give the homopolymer P-$(NorAha\text{-}PTX)_6$ as a solid which was characterize by

SEC-MALS. To the remaining reaction solutions, 9.2 mg (6.75 μmol) of NorAha-GPLGLAGGERDG monomer was added. The mixtures were left to stir under nitrogen for 75 min. After this time, each reaction mixture was split into two portions, half was reacted with ethyl vinyl ether (50 μL) and precipitated in diethyl ether to give the block copolymers P-(NorAha-PTX)$_6$-(NorAha-GPLGLAGGERDG)$_4$ as off-white solid. The second solutions were reacted with Nor-Cy5.5 (2.2 mg, 2.3 μmol) for 2 hrs. After this time, ethyl vinyl ether (50 μL) was added to quench the catalyst. After 15 min the solutions were precipitated by dropwise addition to cold anhydrous ethyl ether to give the P-(NorAha-PTX)$_6$-(NorAha-GPLGLAGGERDG)$_4$-(Nor-Cy5.5)$_1$.

### 3.4.9 Nanoparticle formulation (EM)

Nanoparticles were prepared by sonication method from DMF into DPBS. A probe sonicator (Fisher scientific) was used at 500W. In a model experiment, 3.1 mg (0.240 μmol) of (NorAha-PTX)$_6$-(NorAha-GPLGLAGGERDG)$_4$ was dissolved in DMF (3.1 mL, 1 mg/mL). DPBS (3.1 mL) was added dropwise to the polymer solution under sonication over a period of a minute. The solution was left stirring overnight and subsequently dialyzed against DPBS 1X using 3,500 molecular weight cut off (MWCO) SnakeSkin dialysis tubing. The buffer was changed two times per day for 3 days. The nanoparticles were concentrated using EMD Millipore Amiccon Ultra-15 centrifugal filters (10K Nominal Molecular Weight Limit, NMWL) when necessary and filtered through 0.2 μm EMD Millipore sterile filters prior in vitro cell experiments.

### 3.4.10 Light-induced PTX release of monomers and nanoparticles

Cleavage kinetics of monomers (NorAha-PTX and NorENB-PTX) : Monomer solutions (1 mM) were irradiated by UV light (365nm) for 1hr. Each data was collected at each time points (0min, 10min, 20min, 30min, 60min).

Drug release profile of nanoparticles (EM and LAM) : Nanoparticles solutions were irradiated by UV light (365nm) for 2 hr. The data were collected at different time points. After the irradiation, the solutions were analyzed by RP-HPLC and the resulting peak was compared to that of free PTX (at 18.7 min). Drug release percentage was calculated based on the free drug calibration curve and on the drug concentration in the micelle solutions.

# Chapter 4. Peptide Brush Polymer Backbone Governs Proteolytic Stability of Peptides

## 4.1 Introduction

All living things in nature have evolved chemical digestion mechanisms that involve enzyme-mediated hydrolysis of exogenous biomolecules for food and energy sources.[136] Digestive or hydrolytic enzymes are ubiquitous in human body, from intracellular organelle, such as lysosome, to organs and tissues including digestive systems and blood plasma. Such enzymes play critical roles in the regulation, growth, and defense of cells and tissues.[137] Despite the essential biological functions of digestive enzymes, their *in vivo* ubiquity has posed a long-standing challenge for the development of therapeutic biomolecules which suffer from rapid degradation and very short half-lives upon systemic (intravenous or oral) delivery.[138-140] This is particularly true in the clinical translation of therapeutic peptides over the past century. Indeed, of potentially millions of sequences possibly related to active fragments of proteins very few (<60) peptide-based drugs are successfully used clinically, where a tremendous effort has been made to increase the half-life of therapeutic peptides.[141] Multiple examples of proteolytically stable peptides relying on chemical modification of the amino acid composition and sequence have been developed.[142-145] In these modification methods such as cyclization and *N*-methylation, peptides are rendered unrecognizable by, or inaccessible to the protease active sites. Nevertheless, the therapeutic efficacy of modified peptides is typically decreased in view of the change in chemical identity and connectivity of amino acid sequence.[143] It would be ideal to impart enhanced proteolytic stability

into this important class of biomolecular therapeutics without otherwise compromising the bioactivity.

By arranging multiple peptide strands on a nanoscale scaffold, proteolytic stability and bioactivity of pendant peptides can be potentially strengthened simultaneously.[146] Peptide brush polymers (PBPs) represent an emerging class of peptide therapeutics which adopt a three-dimensional spatial arrangement of side-chain peptides along the polymer backbone. In comparison with free peptides, the multivalent display of peptide strands in PBPs has demonstrated enhanced ligand-receptor binding, cell penetration, and improved proteolytic stability.[147, 148] Moreover, PBPs would hold promise to mitigate the issue of rapid renal clearance because of their characteristic of high molecular weights.[149] In the quest for a generalizable approach to peptide brush polymers, our laboratory has developed a class of peptide brush polymers with polynorbornene backbone *via* functional group tolerant ring-opening metathesis polymerization (ROMP). [147, 148] Every norbornene repeating unit of such PBPs consists of a side-chain peptide, leading to the maximum graft density of peptides. Critically, PBPs with the polynorbornene backbone were shown to resist proteolytic digestion while retaining bioactivity. Interesting questions then arise as to the physiochemical and biological properties of PBPs with other polymer backbones: (*i*) Could other polymer backbone analogues resemble polynorbornene and confer proteolytic stability on pendant peptides? (*ii*) What are the conformations of PBPs with varying polymer backbones? (*iii*) What structural parameters of polymer backbones can elicit the proteolytic stability of side-chain peptides? Understanding the structure of PBPs can provide

insights into their interactions with proteases, as well as the design of multivalent peptide-polymer conjugates with tunable proteolytic stability and bioactivity.

Here, a library of peptide brush polymers with structurally different polymer backbones that enables the mechanistic study of side-chain peptide stability are described. We demonstrate that an increased hydrophobicity of the polymer backbone can lead to enhanced proteolytic stability of side-chain peptides against relevant proteases. All-atom explicit solvent molecular dynamics (MD) simulations reveal the micellar configurations of PBPs, and as the hydrophobicity of polymer backbone increases, peptide cleavage sites are more embedded within the PBP`s three dimensional structure. This results in less exposure of peptide cleavage sites to proteases, and consequently weaker interactions between cleavage sites of peptides and the active sites of protease evidenced by coarse-grained MD simulations. Finally, we evaluated the impact of proteolytic stability on the bioactivity of PBPs by showing that the pro-apoptotic PBP with a more hydrophobic backbone, upon pre-treatment with protease, preserved a significantly higher degree of bioactivity than that of the PBP with a less hydrophobic backbone. Our findings illustrate the structural effects of PBPs on their proteolytic stability, highlighting an exciting potential for leveraging peptide brush polymers in the design of peptide therapeutics with tunable properties.

## 4.2 Results and Discussion

### 4.2.1 Proteolytic Resistance of Peptide Brush Polymers (PBPs) with Different Backbones

To explore the role of polymer backbones in the proteolytic stability of PBPs, we first designed PBPs with four different polymer backbones and the same peptide sequence, that is,

GPLGLAGGWGERDGS, which is a thermolysin substrate (Figure 4.1 A and B). A library of peptide monomers was prepared by solid-phase peptide synthesis protocol, giving rise to peptide acrylamide (PepAm), peptide methacrylamide (PepMAm), peptide norbornylamide (PepNorAm), and peptide norbornylimide (PepNorIm). Electrospray ionization mass spectrometry (ESI-MS) and reversed-phase high-performance liquid chromatography (RP-HPLC) verified the identity and purity of the monomers. Moreover, the RP-HPLC elution time of monomers increases in the order of PepAm, PepMAm, PepNorAm, and PepNorIm, suggesting an upward trend in their hydrophobicity, which is in line with the all-atom explicit solvent MD simulations.

Next, state-of-the-art controlled polymerization techniques including ROMP and photoinduced reversible addition-fragmentation transfer radical polymerization (photo-RAFT) were harnessed to access well-defined PBPs. The excellent functional group tolerance of ROMP and photo-RAFT enabled the access to poly(PepNorIm), poly(PepNorAm), poly(PepMAm), and poly(PepAm) with the same degree of polymerization as well as narrow molecular weight distribution. Nuclear magnetic resonance (NMR) analyses confirmed the full disappearance of monomer signals in the final solution. Additionally, organic-phase gel permeation chromatography (GPC) demonstrates that the molecular weights of all the PBPs are on par with their theoretical values, supporting good control in ROMP and photo-RAFT polymerizations. To further unveil if PBP chains aggregate in water, aqueous-phase GPC was utilized to assess the molecular weights of PBPs in phosphate-buffered saline (PBS) buffer (Figure 4.1 C). The obtained molecular weights of PBPs agree well with their theoretical molecular weights, suggesting that PBPs are presented as sing-chain state rather than aggregation in PBS buffer. Moreover, dynamic light scattering (DLS)

analysis further corroborate the non-aggregated PBPs by revealing the sub-10 nm hydrodynamic diameters of all the PBPs.

Because the side-chain peptide sequence of PBPs is a thermolysin substrate, we next examine the susceptibility of this peptide against thermolysin. ESI-MS analysis confirmed that thermolysin can selectively cleave the amide bond between *C*-terminus of glycine (G) and *N*-terminus of leucine (L), leading to the liberation of two fragments including GPLG and LAGGWEGRDGS. Fast proteolysis kinetics of free peptides was depicted by HPLC analysis that 93% of original peptide signal diminished after 10 min. The proteolysis kinetics of PBPs was further studied under the same conditions (Figure 4.1 D). Impressively, all the PBPs exhibit enhanced proteolytic stability than free peptides (Figure 4.1 E). Poly(PepNorIm$_{15}$) in particular underwent slow digestion kinetics, as confirmed by less than 2% cleavage of pendant peptides after 50 min (Figure 4.1 E). In contrast, thermolysin-induced digestion of other PBPs was significantly faster than poly(PepNorIm$_{15}$) and resulted in more than 70% peptide cleavage within 50 min. The catalytic efficiency ($k_{cat}/K_m$) of thermolysin in digesting PBPs gradually decreased as the hydrophobicity of polymer backbone increases (Figure 4.1 F and Table 4.1). These results clearly demonstrate that the proteolytic stability against thermolysin drops from poly(PepNorIm$_{15}$) to the other PBPs investigated here, and then to the free peptide.

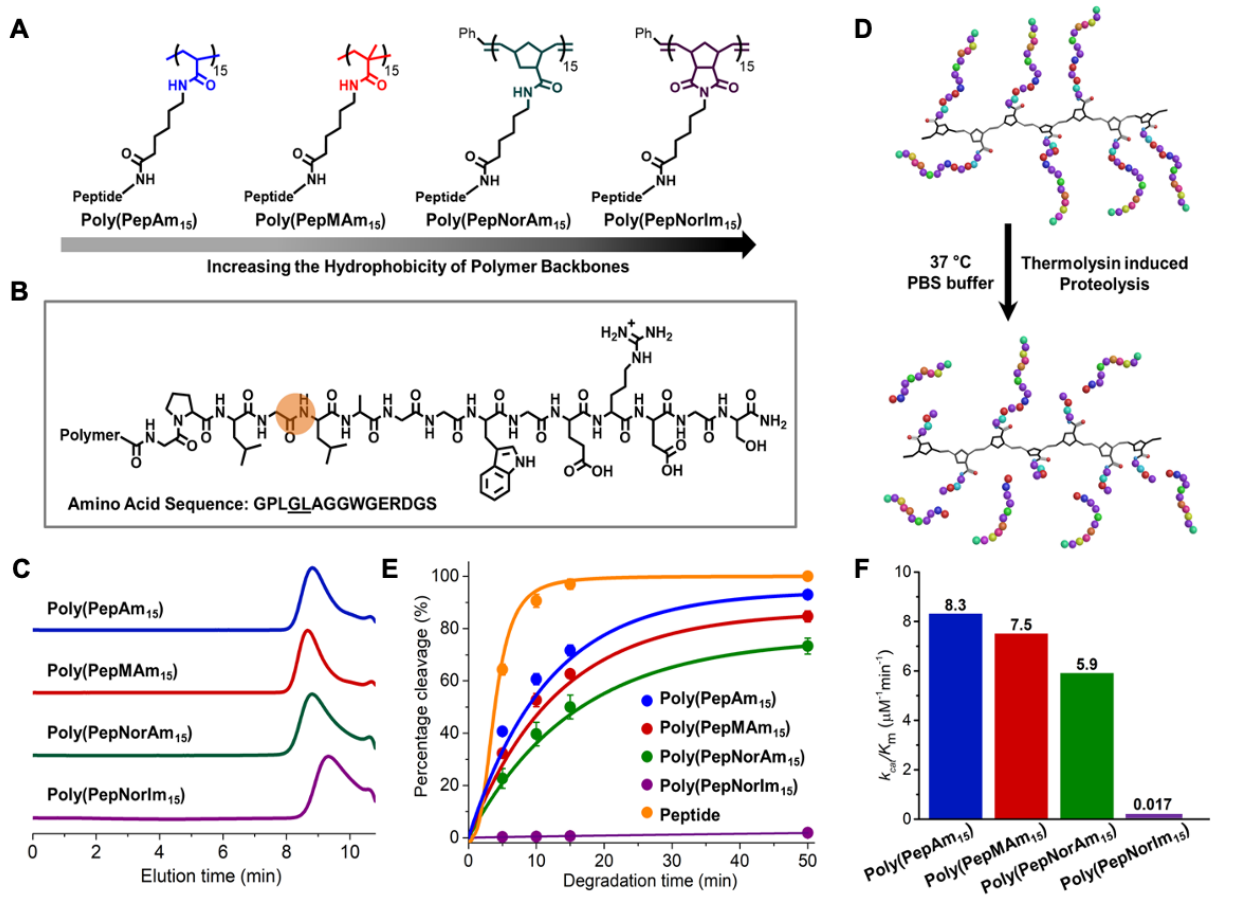


**Figure 4.1** Polymer backbones of peptide brush polymers determines proteolytic resistance of side-chain peptides. (A) Chemical structures of a library of PBPs (DP = 15) consisting of different molecular structures in their polymer backbones. (B) Chemical structure of the peptide (amino acid sequence: GPLGLAGGWGERDGS) used in this study. This peptide is a thermolysin substrate which can be selectively cleaved between glycine and leucine with the cleavage site highlighted in orange. (C) GPC traces of PBPs using PBS buffer as the mobile phase. The molecular weights of polymers in PBS buffer are similar to their theoretical values, indicating the predominance of single polymer chains in PBS buffer (See supplementary Table 1 for detailed molecular weight information). (D) Schematic illustration of proteolytic digestion of peptide brush polymers in the presence of thermolysin using a representative polymer poly(PepNorAm$_{15}$). (E) Proteolysis kinetics of PBPs and free peptide revealed by HPLC (See supplementary Figs. 19-23 for raw HPLC data). The molar concentrations of peptide substrate and thermolysin are 200 μM and 0.05 μM, respectively. Poly(PepNorIm$_{15}$) exhibits the highest proteolytic stability among all the polymers. Data displayed as mean ± standard deviation of three independent experiments. (F) Catalytic efficiency ($k_{cat}/K_m$) of thermolysin in proteolysis of PBPs derived from non-linear Michaelis-Menton Kinetics (See **Table 4.1** for details). Catalytic efficiency of poly(PepNorIm$_{15}$)

is markedly lower than all other polymers, indicative of the slowest proteolysis of poly(PepNorIm$_{15}$) against thermolysin.

| | Poly(PepAm$_{15}$) | Poly(PepMAm$_{15}$) | Poly(PepNorAm$_{15}$) | Poly(PepNorIm$_{15}$) |
|---|---|---|---|---|
| $K_m$ (μM) | 21 | 19 | 25 | 37 |
| $V_{max}$(μMmin$^{-1}$) | 8.6 | 6.9 | 7.6 | 0.031 |
| $k_{cat}$ (min$^{-1}$) | 173 | 139 | 152 | 0.62 |
| $k_{cat}/K_m$ (μM$^{-1}$min$^{-1}$) | 8.3 | 7.5 | 5.9 | 0.017 |

**Table 4.1** Summary of half maximum velocity concentration ($K_m$), maximum proteolysis velocity ($V_{max}$), turnover number ($k_{cat}$), and catalytic efficiency ($k_{cat}/K_m$) of thermolysin-sensitive peptide brush polymers with different polymer backbones. The values of $K_m$ and $V_{max}$ were obtained using non-linear, michaelis-menten fitting of Prism 7 software. $k_{cat} = V_{max}/[E]_o$, where enzyme concentration $[E]_o = 0.05$ μM.

### 4.2.2 Computational Analysis

To gain insight into the mechanism of the varying proteolytic resistance of PBPs, we first conducted all-atom explicit solvent MD simulations to investigate the morphology of PBPs and the distribution of the PBP cleavage sites (glycine and leucine). The equilibrated PBPs exhibit roughly globular micellar structure (Figure 4.2). The side-chain peptides are structureless as evidenced by the predominance (> 94%) of the random coil secondary structure for all the PBPs (Supplementary Table 4). Inspection of the PBP cleavage sites (orange beads in Figure 4.2) indicates that the cleavage sites of poly(PepNorIm$_{15}$) are partially embedded in the interior of the globular structure, whereas the cleavage sites of the other three PBPs are more dispersedly distributed. Using a protein-sized probe with a radius of 3.14 nm,[148] the exposure of the PBP cleavage sites described through the solvent-accessible surface area (SASA) was found to decrease

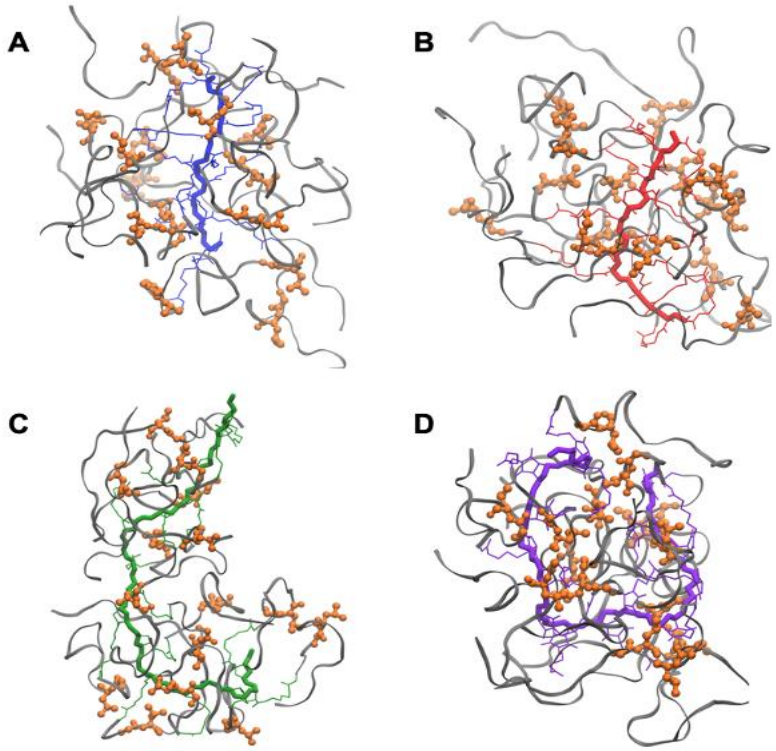


**Figure 4.2** Configurations of PBPs in an aqueous solution of 0.14M NaCl. The side-chain peptides (GPLGLAGGWGERDGS) are structureless and illustrated with gray ribbons and the cleavage sites (GL) with orange beads. The polymer backbones of (A) poly(PepAm15), (B) poly(PepMAm15), (C) poly(PepNorAm15), and (D) poly(PepNorIm15) are colored blue, red, green, and purple, respectively. PBP hydrogen atoms, water, and salt ions are omitted for display.

following the order: poly($PepAm_{15}$) > poly($PepMAm_{15}$) > poly($PepNorAm_{15}$) > poly($PepNorIm_{15}$) (Figure 4.3 A). This agrees with the increase in the PBP backbone hydrophobicity: poly($PepAm_{15}$) < poly($PepMAm_{15}$) < poly($PepNorAm_{15}$) < poly($PepNorIm_{15}$). These simulation results thus support that an increase in polymer backbone hydrophobicity condenses the side-chain peptides of PBP, leading to the less exposure of the peptide cleavage sites. Specifically, poly($PepNorIm_{15}$) displayed the strongest hydrophobicity, which drives the cleavage sites to be the least exposed to

the surrounding environment. The least exposure of the poly(PepNorIm$_{15}$) cleavage sites is also supported by their strongest aggregation, as evidenced by the strong primary correlation peak at the distance of around 4.2 Å on the radial distribution function between the cleavage sites (Figure 4.3 B).

To understand the proteolytic stability of the PBPs, we carried out MARTINI coarse-grained explicit solvent MD simulations on PBP-thermolysin complexes in an aqueous solution with 0.14 M NaCl for two PBPs of poly(PepNorIm15) and poly(PepMAm15). The obtained interaction energies between PBPs and thermolysin conclude that the cleavage sites of poly(PepNorIm15) negligibly interact with thermolysin active sites (-0.02 ± 0.02 kJ/mol), whereas much stronger interactions (-0.9 ± 0.7 kJ/mol) exist between poly(PepMAm15) cleavage sites and thermolysin active site (Figure 4.3 C and D). This is in line with the experimental observations that poly(PepNorIm15) displays a lower PBP-thermolysin affinity than poly(PepMAm15) (Figure 4.1 E and F). The weaker interactions between poly(PepNorIm15) cleavage sites and thermolysin active sites (the lower poly(PepNorIm15)-thermolysin affinity) can be ascribed to the less exposure of the poly(PepNorIm15) cleavage sites (Figure 4.2). In each PBP-thermolysin system, the simulation last 18 μs, the last 9 μs of which was performed using the GōMartini 2.2 protein model 15 to investigate a possible structural change in protein structure upon the binding of PBP to thermolysin. Detailed calculations before and after the PBP-thermolysin binding event reveal that the structures of both proteins and PBPs were highly preserved, as evidenced by the negligible changes in root-mean-square deviation of the backbones of the whole protein and its active site alone, as well as the molecular size (radius of gyration and end-to-end distance) of the PBP chains. Therefore, the exposure of the PBP cleavage sites obtained by the all-atom simulations in the

absence of protein (Figure 4.2 A) might be employed in ranking the interactions between PBP cleavage sites and protein active sites (Figure 4.2 C), which are associated with the proteolytic resistance of PBPs against proteases. The structure-property relationship is thus established that an increase in PBP backbone hydrophobicity leads to a decreased exposure of the PBP cleavage sites, which decreases their interactions with proteases, giving rise to the enhanced proteolytic stability.

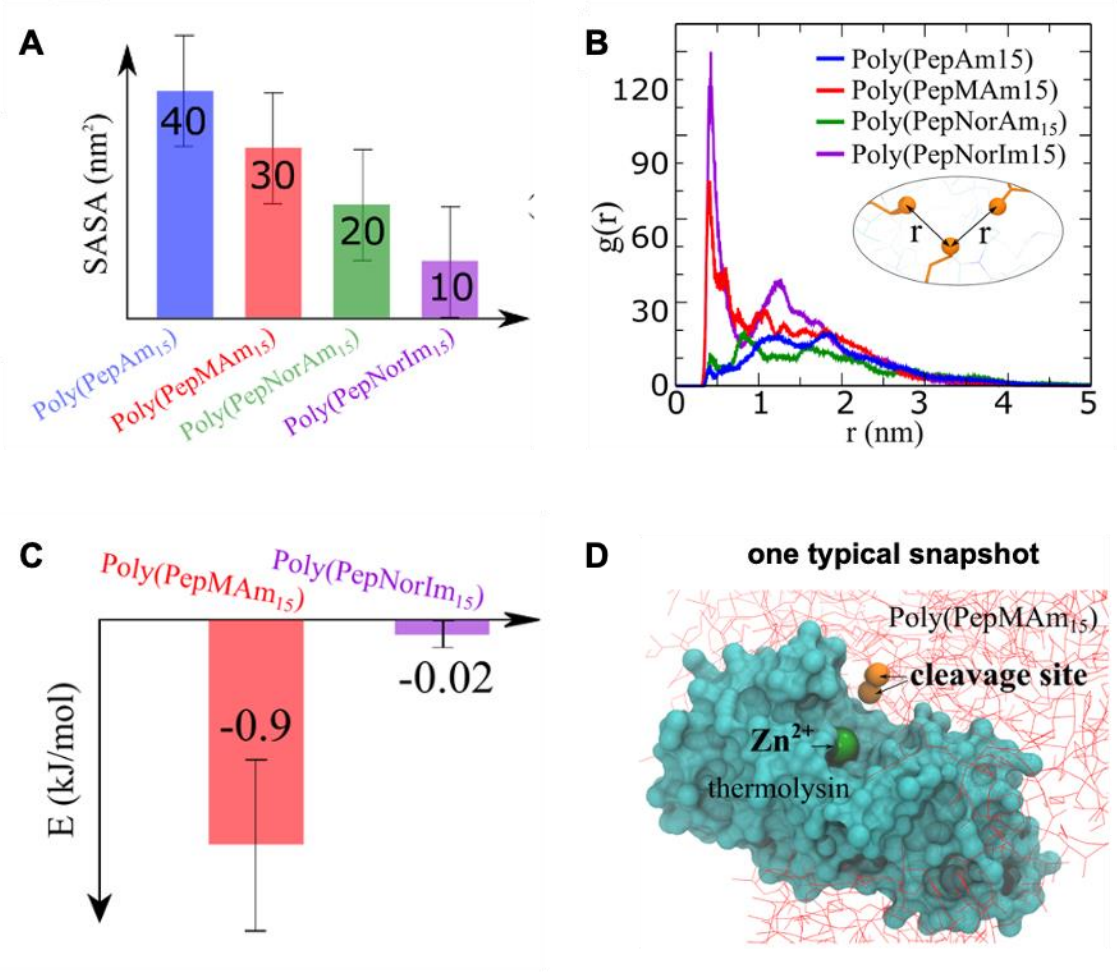


**Figure 4.3** Computational analysis of peptide brush polymers. (A) Solvent-accessible surface area of PBP cleavage sites calculated using a protein-sized probe (B) Radial distribution function of the last tail carbons of leucine (see the inset) on PBP cleavage sites. (C) Potential energy between PBP cleavage sites and thermolysin active sites from the MARTINI coarse-grained simulations, with one typical snapshot presented in (D), where the PBP cleavage sites are colored in orange and the thermolysin $Zn^{2+}$ ion in green. Poly(PepNorIm$_{15}$) cleavage sites display the less exposure than that of poly(PepMAm$_{15}$), leading to weaker interactions with thermolysin active sites.

### 4.2.3 Proteolytic Stability of PLPs Against Other Two Enzymes

To interrogate whether the established relationship between the polymer backbone and proteolytic stability is general, we examined two more proteases: α-Chymotrypsin and pepsin, which are digestive proteases and belong to the subsets of serine proteases and aspartyl proteases, respectively. In light of the prevalence of α-chymotrypsin and pepsin in human digestive systems, developing peptide delivery systems which are stable against these proteases would have promise in the oral administration of therapeutic peptides. We designed a series of PBPs, the peptides on which can be selectively cleaved by α-chymotrypsin (Figure 4.4 A), and pepsin (Figure 4.4 C), respectively. Proteolysis kinetic study reveals that the stability of PBPs with poly(NorIm) backbone consistently outperform PBPs with other polymer backbones (Figure 4.4 B and D). Moreover, the proteolytic stability of all the PBPs is noticeably higher than their corresponding low-molecular-weight peptide monomers (Figure 4.4 B and D). These results are in good agreement with our experimental observation in the case of thermolysin (Figure 4.1). Given that the investigated peptide cleavage sites range from nonpolar (GL in Figure 4.1) to charged (RG in Figure 4.4 A), and to modestly polar (MS in Figure 4.4 C) amino acids, this work verifies that our theory of polymer backbone effect on PBP stability is general to a wide variety of peptide substrates and proteases.

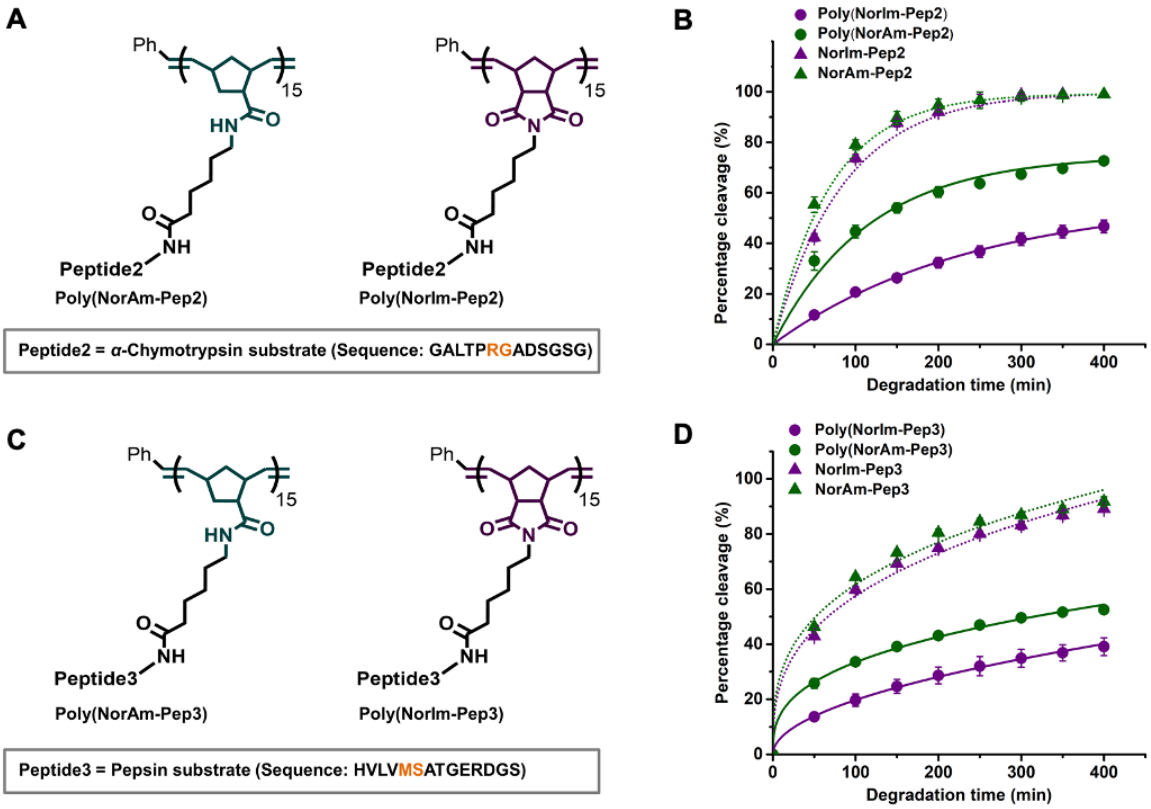


**Figure 4.4** Proteolytic stability of peptide brush polymers against a serine protease (α-chymotrypsin) and an aspartyl protease (pepsin) (A) Chemical structures of peptide brush polymers with different polymer backbones. A chymotrypsin substrate GALTPRGADSGSG is pendent on the side-chains of peptide brush polymers. The cleavage site (RG) is highlighted in orange. (**C**) Chymotrypsin-catalyzed proteolysis kinetics of peptide brush polymers and their respective monomers. The molar concentrations of peptide substrate and chymotrypsin are 200 μM and 1 μM, respectively. Poly(NorIm-Pep2) demonstrated the highest proteolytic resistance in comparison with other polymers and monomers. (C) Chemical structures of peptide brush polymers featuring a pepsin substrate: HVLVMSATGERDGS. The cleavage site (MS) is highlighted in orange. (D) Pepsin-triggered proteolysis kinetics of peptide brush polymers and their respective monomers. The molar concentrations of peptide substrates and pepsin are 200 μM and 0.2 μM, respectively. The proteolytic stability of poly(NorIm-Pep3) is higher other polymers and monomers. Data displayed as mean ± standard deviation of three independent experiments.

### 4.2.4 Retention of PLP Bioactivity Upon the Pretreatment of Enzyme

High proteolytic resistance is a prerequisite for therapeutic peptides to retain their bioactivity in a complex environment, such as blood serum and digestive systems, where proteases are abundant. Since the proteolytic stability of poly(NorIm)-based PBPs is higher than other analogues, we reasoned that the poly(NorIm)-based PBPs would exhibit preservation of their bioactivity to a greater extent than other PBPs in a protease-containing environment . To examine our hypothesis, we designed two proof-of-concept PBPs including poly(MAm-KLA) and poly(NorIm-KLA), which consist of pro-apoptotic peptides (amino acid sequence: KLAKLAKKLAKLAK, abbreviated as KLA) (Figure 4.5 A and B). KLA peptide is well-known for promoting apoptosis in cancer cells via disruption of mitochondrial membrane (Figure 4.5 C). Moreover, KLA peptide is typically fused with a cell penetration peptide such as TAT peptide (sequence: YGRKKRRQRRR), giving rise to TAT-KLA, which can render KLA peptide

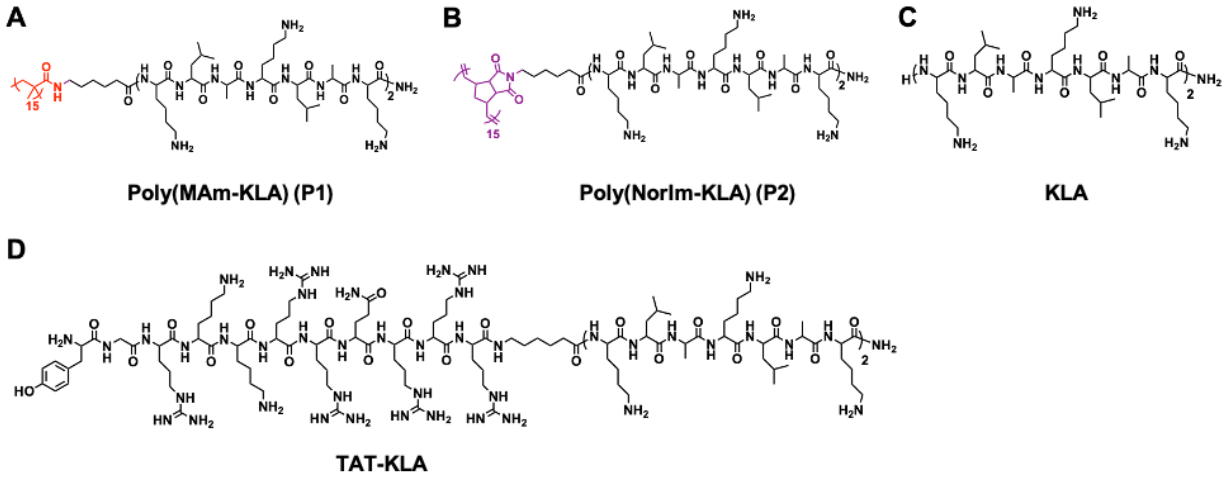


**Figure 4.5** Chemical structures of proapoptotic peptide brush polymers (A) Poly(MAm-KLA) (P1), (B) Poly(NorIm-KLA) (P2) and peptide analogues (C) KLA peptide and (D) TAT-KLA peptide featuring a side-chain amino acid sequence: KLAKLAKKLAKLAK, which can induce apoptosis in cancer cells.

permeable to cell membranes. Therefore, we further prepared TAT-KLA as a positive control (Figure 4.5 D) to compare its bioactivity, that is, pro-apoptotic efficacy, with poly(MAm-KLA) and poly(NorIm-KLA) (Figure 4.5).

To evaluate the apoptotic process of the cancer cells (HeLa cell line), we performed annexin V/propidium iodide (PI) staining assay to quantify the percentage of apoptotic cells upon the incubation with poly(MAm-KLA), poly(NorIm-KLA), TAT-KLA and KLA peptide and their respective analogues, which were pretreated by α-chymotrypsin (Figure 4.6). Notably, both poly(MAm-KLA) and poly(NorIm-KLA) demonstrated a higher pro-apoptotic efficacy than that of TAT-KLA, as evidenced by higher percentages of apoptotic cells in the cases of poly(MAm-KLA) and poly(NorIm-KLA). The enhanced bioactivity of PBPs compared to free peptides is

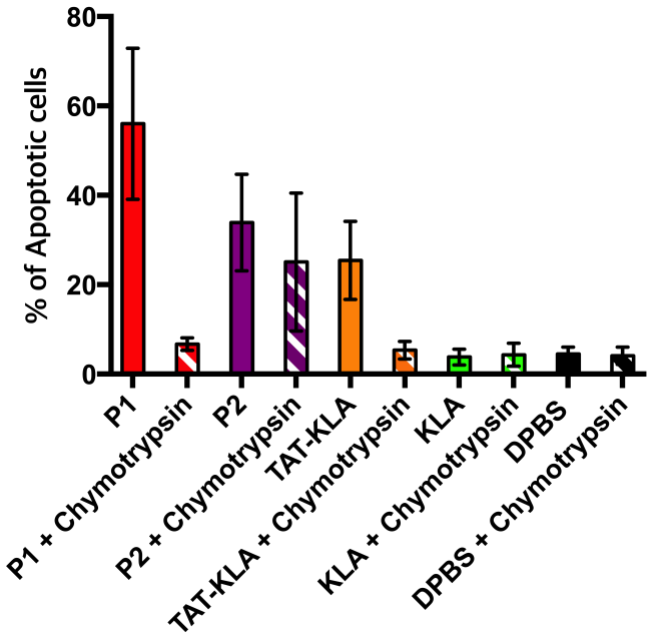


**Figure 4.6** Percentage of apoptotic cells analyzed by an annexin V/propidium iodide (PI) staining assay. HeLa cells were incubated with Poly(MAm-KLA) (P1), Poly(NorIm-KLA) (P2), TAT-KLA, KLA, DPBS and the respective chymotrypsin-pretreated materials at a concentration of 25 μM with respect to peptide for 24 hours.

attributed to the multivalent effect of PBPs, which stems from their brush architecture. However, the treatment of chymotrypsin pretreated poly(MAm-KLA) and TAT-KLA led to a marked decrease in their pro-apoptotic efficacy, suggesting a significant extent of proteolysis of these KLA-containing materials (Figure 4.6). On the contrary, chymotrypsin-pretreated poly(NorIm-KLA) demonstrated a much higher retention of bioactivity than poly(MAm-KLA) and TAT-KLA. Additionally, the cytotoxicity of KLA-containing materials to cancer cells was evaluated (Figure

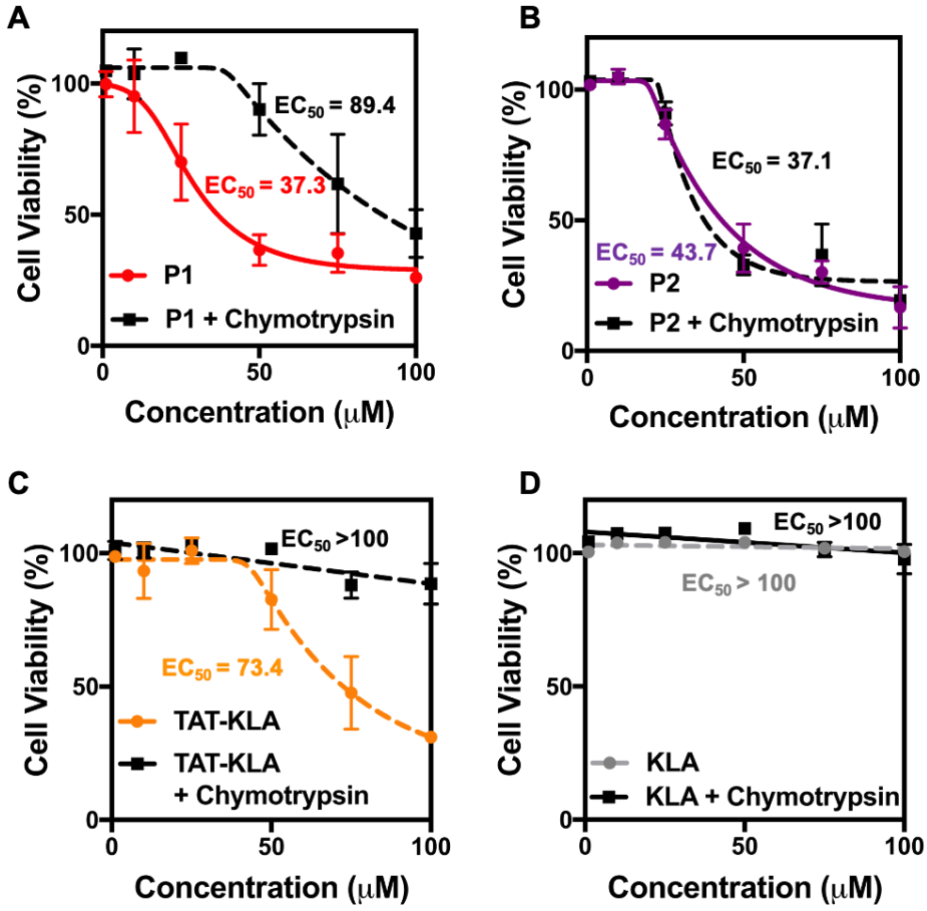


**Figure 4.7** Cell viability assay of HeLa cells incubated with original KLA-containing materials and chymotrypsin-pretreated materials. (A) Poly(MAm-KLA) (P1), (B) Poly(NorIm-KLA) (P2) and peptide analogues (C) TAT-KLA and (D) KLA. The concentration of the x-axis was calculated with respect to peptide. Data are presented as means ± SD (n = 3).

4.7). The half maximal effective concentrations (EC50) of original poly(NorIm-KLA) and poly(MAm-KLA) were found to be similar, whereas both are lower than that of TAT-KLA. Upon the pretreatment with chymotrypsin, poly(NorIm-KLA) has preserved its EC50 value while the EC50 values of poly(MAm-KLA) and TAT-KLA have dramatically increased, consistent with the cell apoptosis assay in Figure 4.6.

To discern the mechanism of cell apoptosis, we performed the mitochondria function assay using the turn on JC-1 probe to evaluate the mitochondrial membrane potential, which is a key feature of mitochondrial health (Figure 4.8). The JC-1 probe is a green-fluorescent carbocyanine that can form red-fluorescent JC-1 aggregates after accumulation in the healthy mitochondria with a normal membrane potential. In light of this, we used confocal laser scanning microscopy to compare the green and red fluorescence at the same excitation wavelength at 488 nm (Figure 4.8). As expected, Hela cells incubated with original poly(NorIm-KLA) and poly(MAm-KLA) showed weak red fluorescence, similar to cells treated with TAT-KLA, indicating that mitochondria membrane was disrupted by the KLA-containing materials. Nevertheless, chymotrypsin-induced digestion of poly(MAm-KLA) and TAT-KLA resulted in significant loss of their pro-apoptotic function, as proved by the appearance of red fluorescence, which is associated with healthy mitochondria (Figure 4.8). The behavior of poly(NorIm-KLA) was approximately unaltered after the digestion, validating that poly(NorIm-KLA) exhibits a high proteolytic stability against chymotrypsin. Altogether, this proof-of-concept in vitro study suggests the critical role of hydrophobic polymer backbone, that is, poly(NorIm), in achieving a high proteolytic stability, as well as retaining bioactivities of PBPs in protease-rich environments.

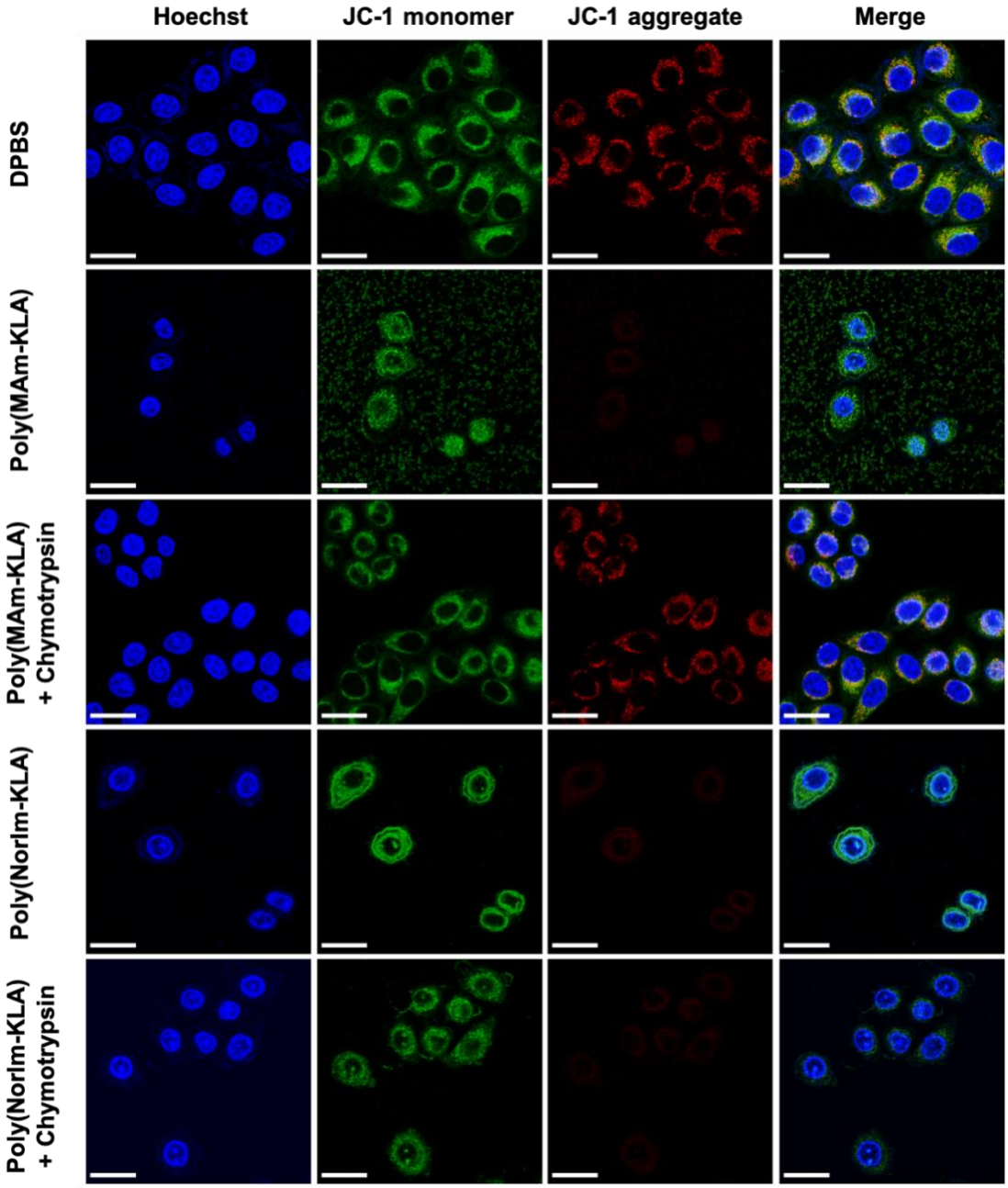


**Figure 4.8** Mitochondria function assay of HeLa cells using Live-cell confocal microscope and JC-1 probe. The cells were incubated with Poly(MAm-KLA), Poly(NorIm-KLA), and respective chymotrypsin-pretreated analogues at a concentration of 25 μM with respect to peptides for 48 hours. Prior to imaging, cells were stained with 2 μM of JC-probe (green, monomer, $\lambda_{ex/em}$ = 488 nm/510-550 nm; red, J-aggregates, $\lambda_{ex/em}$ = 488 nm/585-649 nm) and then Hoechst (blue, $\lambda_{ex/em}$ = 358 nm/ 461 nm). Scale bar, 20 μm.

## 4.3 Conclusion

In summary, we have unraveled the relationship between the polymer backbone and proteolytic stability of pendant peptides in peptide brush polymers. While all the peptide brush polymers, regardless of the polymer backbone, demonstrate higher stability in comparison to their respective free peptides, the hydrophobicity variation in different polymer backbones leads to distinguishable resistance performance of PBPs against proteases. An increase in polymer backbone hydrophobicity bestows PBPs with elevated proteolytic resistance. Multiscale computer simulations further corroborate the experimental observations by deciphering the conformations of PBPs, which reveals a decrease in the exposure of peptide cleavage sites as polymer backbone hydrophobicity increases, which consequently weakens the interactions between peptide cleavage sites and protease active site. Furthermore, the impact of proteolytic stability on the biological performance of PBPs is assessed, showing that the pro-apoptotic PBP with a more hydrophobic poly(NorIm) backbone, upon exposure to protease, retained a much higher degree of bioactivity than that of the PBP with a less hydrophobic poly(MAm) backbone. Given the substantial promise of therapeutic peptides in biomedical applications, we envision that the mechanistic insights in this study will shed light on the future development of proteolytically stable peptide delivery systems with high retention of bioactivity.

## 4.4 Experimental Details

### 4.4.1 Synthesis of Poly(PepMAm) and Poly(PepAm) via Photo-RAFT Polymerization.

Homopolymers of PepMAm and PepAm were achieved by photo-initiated reversible addition-fragmentation transfer (photo-RAFT) polymerization. In a typical aqueous photo-RAFT polymerization for making poly($PepMAm_{15}$) targeting a DP of 15, peptide methacrylamide monomer (30 mg, 15 equiv.) were dissolved in 150 µL of DPBS buffer. Then, water-soluble RAFT agent, 4-((((2-carboxyethyl)thio)carbonothioyl)thio)-4-cyanopentanoic acid (0.38 mg, 1.0 equiv.) was added into the reaction mixture. Following that, 19 µL of the SPTP stock solution (0.3 equiv., 6.0 mg in 1 mL of DPBS buffer) was added. The solution was degassed by $N_2$ flow for 30 min and then placed into the photo-reactor (λmax = 365 nm, 3.4 mW/cm2) for 12 h. Upon the polymerization, the polymer solution was further purified via dialysis into deionized water. Finally, the polymer product was obtained by lyophilization.

### 4.4.2 Synthesis of Poly(PepNorIm) and Poly(PepNorAm) via ROMP

Homopolymers of PepNorIm and PepNorAm were achieved by ring-opening metathesis polymerization (ROMP) under nitrogen gas in a glove box. In a typical ROMP protocol for preparing poly(PepNorIm15), PepNorIm (20 mg, 15.0 equiv.) was dissolved in 300 µL of degassed DMF (1 M LiCl). Next, 287 µL of the olefin metathesis initiator $(IMesH_2)(C_5H_5N)_2(Cl)_2Ru{=}CHPh$ stock solution (1.0 equiv., 2 mg/mL in DMF) was quickly added into the monomer solution. The solution was left to stir for 5 h until the full consumption of monomers. After the polymerization,

the polymer solution was further purified via dialysis into deionized water. Finally, the polymer product was obtained by lyophilization.

### 4.4.3 Evaluation of the Stability of Peptide Brush Polymers Against Thermolysin

For thermolysin-induced cleavage experiments, the molar concentration of thermolysin was set to 0.1 μM. The concentration of side-chain peptides (GPLGLAGGWGERDGS) varied in the range of 50-200 μM. Moreover, the temperature was set to 37 °C to match the body temperature. In a typical experiment, poly(PepNorIm$_{15}$) (1.65 mg**,** 1 μmol with respect to side-chain peptides) was dissolved in 5 mL of DPBS solution, leading to the stock polymer solution with a peptide concentration of 200 μM. Next, 3.5 μL of thermolysin stock solution (1.0 mg/mL) was added into 1 mL of the polymer solution which was subsequently stirred in a preheated oil bath at 37 °C. In this case, the molar ratio of peptide substrate to thermolysin was 2000: 1. During the cleavage, aliquots were taken for HPLC analysis at predetermined time points. Each degradation experiment was repeated three times.

### 4.4.4 Evaluation of the Stability of Peptide Brush Polymers Against α-Chymotrypsin

For chymotrypsin-induced cleavage experiments, the molar concentrations of chymotrypsin and peptide substrate (GALTPRGADSGSG) were set to 1.0 μM and 200 μM, respectively. In addition, the temperature was set to 37 °C to match the body temperature. In a typical experiment, poly(NorIm-Pep2) (1.40 mg**,** 1 μmol with respect to pendant peptides) was dissolved in 5 mL of DPBS solution, leading to the stock polymer solution with a peptide concentration of 200 μM. Next, 25 μL of chymotrypsin stock solution (1.0 mg/mL) was added

into 1 mL of the polymer solution which was subsequently stirred in a preheated oil bath at 37 °C. In this case, the molar ratio of peptide substrate to thermolysin was 200: 1. During the cleavage, aliquots were taken for HPLC analysis at predetermined time points. Each degradation experiment was repeated three times.

### 4.4.5 Evaluation of the Stability of Peptide Brush Polymers Against Pepsin

For pepsin-triggered cleavage experiments, the molar ratio of pepsin to peptide substrate (HVLVMSATGERDGS) was set to 1: 1000. The temperature was set to 37 °C to match the body temperature. For example, poly(NorIm-Pep3) (1.72 mg**,** 1.0 μmol with respect to peptides) was dissolved in 5 ml of HCl solution (pH = 2), leading to the stock polymer solution with a peptide concentration of 200 μM. Then 7.2 μL of pepsin stock solution (1 mg/mL) was added into 1 mL of the polymer solution which was subsequently stirred in a preheated oil bath at 37 °C. During the cleavage, aliquots were taken for HPLC analysis at predetermined time points. Each degradation experiment was repeated three times.

### 4.4.6 Cell Viability Assay

HeLa cells were grown in Dulbecco's modified Eagle medium (DMEM) supplemented with 10 % fetal bovine serum (FBS), 1% penicillin−streptomycin. Cells were maintained at 37 °C and 5% $CO_2$ with a relative humidity of 95%. HeLa cells were plated in 96-well plates at a density of 5000 per well and then left to attach for 24 h. Subsequently, the cells were treated with the polymers of various concentrations for 72 h followed by washing 3 times with PBS buffer. Then CellTiter-Blue® at 20% (v/v) in complete media was added to each well and incubated for 2 h to

allow the live cells to convert resazurin to fluorescent resorufin. The fluorescent signal (Excitation wavelength: 560 nm; Emission wavelength: 600 nm) was then analyzed by a plate reader. Three replicates were performed for each independent sample. 10% DMSO was used as a positive control and untreated cells in complete medium as a negative control. Viability is reported as a percentage of untreated cells.

### 4.4.7 Cell Apoptosis Assay via Flow Cytometry Analysis

HeLa cells were seeded in 6 well plate (2 x 105 cells per well) for 24 h. Then, the cells were treated with 25μM of KLA containing materials with respect to peptide. For the chymotrypsin pretreated materials, the materials (1000 μM) were pretreated with α-chymotrypsin(1 μM) for 10 min and quenched at 65 °C for 10 min. After treatment for 24 h, the cells were washed and resuspended to the binding buffer, followed by staining with FITC-annexin V/ propidium iodide (PI) for 15 min. The stained cells in each well were analyzed by flow cytometry.

### 4.4.8 Mitochondria Membrane Potential of HeLa cells

HeLa cells were seeded in 4-well, glass bottom dishes (1 x $10^4$ cells per well) for 24 h. Then, the cells were treated with materials for 24 h. The cells were stained with 2 μM of JC-1 probe (green, monomer, $\lambda_{ex/em}$ = 488 nm/510-550; red, JC-1 aggregate, $\lambda_{ex/em}$ = 488nm/585-650nm) at 37 °C for 15 min, washed with PBS buffer to remove any membrane-bound, non-internalized fluorophores, and returned to complete medium. Before the live-cell confocal microscopy observation, 1 drop of Hoechst 33342 dye (blue, $\lambda_{ex/em}$ = 405 nm/420-480 nm) was added to stain

the nuclei. Live-cell confocal microscopy was employed to observe the fluorescence of JC-1 monomer, JC-1 aggregate and Hoechst dye.

### 4.4.9 All-Atom Explicit Solvent Simulations on Peptide Brush Polymers in the Absence of Protein

Classical all-atom explicit solvent molecular dynamics (MD) simulations were performed to study the morphology of peptide brush polymers (PBPs) in aqueous solutions. The package GROMACS (version 2016.3) [150] was used. The CHARMM 36m potential [151] was employed for amino acids, $Na^{+,}$ and $Cl^{-}$ ions. The CHARMM 36m potential was improved from the previous version of CHARMM 36 to better describe disordered proteins, which is of strong relevance to the present work, where most of the peptides favor disordered structures. The recommended CHARMM TIP3P water model [152] was applied with the structures constrained via the SETTLE algorithm. [153] The CHARMM General Force Field (CGenFF 4.0) [154-156] was employed for PBP backbone atoms.

Four PBPs were investigated, including poly($PepNorIm_{15}$), poly($PepNorAm_{15}$), poly($PepMAm_{15}$), and poly($PepAm_{15}$). For each simulation, one PBP chain was initially dissolved in a water box with an edge length of 12 nm in each dimension. A salt concentration of [NaCl] = 0.14 M was employed to mimic the phosphate-buffered saline (PBS) buffer. Periodic annealing simulations [157, 158] were performed for a duration of 200 ns to remove the impact of initial structures. During the annealing process, the system temperature was increased from 298 K to 353 K within 1 ns, maintained at 353 K for a duration of 19 ns, and then cooled down to 298 K within 1 ns. The system temperature was then maintained at 298 K for another 19 ns. Therefore, each annealing

process lasted 40 ns, which was reported 5 times (200 ns in total). In the annealing simulations, the other parameters were the same as those in the subsequent production simulations at 298 K.

In the production simulations, the periodic boundary conditions were employed in all the dimensions. The neighbor searching was calculated up to 12 Å using the Verlet particle-based method and was updated every 20 time steps. The Lennard-Jones (LJ) 12-6 interactions were switched off from 10 to 12 Å via the potential-switch method in GROMACS. The short-range Coulomb interactions were truncated at the cut-off distance of 12 Å, and the long-range interactions were calculated using the Smooth Particle Mesh Ewald (PME) algorithm. [159, 160] The NPT ensemble (constant number of particles, pressure, and temperature) was employed. The temperatures of PBP, ions, and water were separately coupled using the Nosé-Hover algorithm (reference temperature 298 K, characteristic time 1 ps). The isotropic Parrinello-Rahman barostat was employed with the reference pressure of 1 bar, the characteristic time 4 ps, and the compressibility $4.5\times10^{-5}$ $bar^{-1}$. All the covalent bonds were constrained, which supported an integration time step of 2.5 fs. These parameters were recommended for the accurate reproduction of the original CHARMM simulation on lipid membranes,[161] and have been verified in simulation on proteins [162-165] and lipid membranes. [166]

The short-range potential energy between PBP backbones, and between PBP backbones and water molecules were calculated. The Coulomb and LJ interactions were calculated up to the cut-off distance of 1.2 nm employed in the all-atom simulations. A positive Coulomb potential energy and a larger ratio of E(LJ)/E(Coul.) together support the increase in the hydrophobicity of the PBP backbone: poly($PepAm_{15}$) < poly($PepMAm_{15}$) < poly($PepNorAm_{15}$) < poly($PepNorIm_{15}$).

The solvent-accessible surface area (SASA) was calculated using the GROMACS program *gmx sasa*. [167] A probe with a radius of 3.14 nm was employed to represent a protein-sized probe, which was employed to calculate the SASA of PBP molecules in an early work. [148] A small water-sized probe with a radius of 0.14 nm was also employed.

### 4.4.10 Development of MARTINI CG Force Field Parameters for PBP Backbones

The MARTINI CG force field has been extensively employed for proteins,[168, 169] polymers,[170, 171] lipids,[172] and others. [173, 174] In the MARTINI potential, four heavy atoms are generally coarse-grained into one bead (the four-to-one mapping rule). Four interaction types (polar = P, intermediate polar = N, apolar = C, charged = Q) and some subtypes were employed based on the hydrogen bonding capability or the degree of polarity. The MARTINI potential has been proven to be capable of semi-quantitatively reproducing experimental and atomistic simulation results at a longer time scale and larger length scale than atomistic simulations could afford. [165, 175]

The MARTINI force field parameters have been reported for amino acids,[168, 169] but are missing for the PBP backbones investigated here. We thus developed the MARTINI 2.2 parameters for the PBP backbones for poly(PepNorIm$_{15}$) and poly(PepMAm$_{15}$). The bond length and angles were obtained from the corresponding all-atom structure. The force constant of 5000 kJ/mol/nm$^2$ was employed for the covalent bonds, and the force constants for the angles were slightly adjusted to better reproduce the PBP structures (see below).

In the MARTINI simulations, each system included one PBP chain and 0.14 M NaCl dissolved in a water box with an edge length of around 12 nm. The system compositions are the

same as those in the all-atom simulations for side-by-side comparison. For all the MARTINI simulations in this work, around 10% of water particle (W) was replaced with the antifreeze water (WF) to prevent the freezing of the MARTINI water beads at room temperature. [172]

In the production simulations, the recommended parameters [176] for the MARTINI 2.2 potential were employed, which are summarized here. The short-range Coulomb interactions were calculated up to 1.1 nm with the reaction field approach (relative permittivity of 15) for the long-range electrostatic interactions. The LJ 12-6 potential interactions were truncated at 1.1 nm. The NPT ensemble was applied. The temperatures of PBPs, water, and ions were separately coupled at 298 K using the velocity rescaling method. The isotropic pressure coupling (reference pressure 1 bar, time constant 12.0 ps, compressibility $3\times10^{-4}$ $bar^{-1}$) was employed using the Parrinello-Rahman algorithm. The leapfrog integration time step of 20 fs was employed. Each production simulation lasted 0.5 μs. We calculated the radius of gyration for the whole PBP and the PBP backbone particles, and the end-to-end distance for the PBP backbone. All these calculations agreed well with the corresponding all-atom simulation results. This thus supports the employment of the MARTINI simulations on PBP-thermolysin complexes below.

### 4.4.11 Comparison of The MARTINI ElNeDyn2.2 and GōMartini2.2 Models on Thermolysin

For protein studies using the MARTINI potential, two models are generally employed to preserve folded protein structures at the CG resolution: the ElNeDyn (elastic network) model [177] and the GōMartini model. [178] The former could well preserve protein structure, while the latter is required for protein activity study. To investigate if the PBP binding could deform the protein

thermolysin, and affect protein activity, we are focusing on the GōMartini 2.2 model in the present work.

In the MARTINI CG potential, the secondary structures of amino acids are pre-defined and fixed throughout the simulations. Generally, an elastic network model (ElNeDyn) is applied to preserve protein structures, [177] where the neighboring noncovalent CG particles up to a cutoff distance, *e.g.*, 0.9 nm, are structurally constrained using a harmonic bond potential with the force constant of 500 kJ/mol/nm$^2$. The harmonic potential was not allowed to break by nature. The elastic network model was initially designed to preserve protein structures but has limited applications for protein activity studies due to the unbreakable feature of the harmonica potential.

In contrast, the GōMartini approach [178] was recently proposed to take into account the flexibility of proteins, which are required for protein activity studies. In the GōMartini model, such harmonic potential was replaced with the LJ 12-6 potential, which could break and reform, enabling the change in protein conformation. Remarkably, it has been very recently demonstrated that the GōMartini 3 model is capable of protein configuration change for several mutations of copper, zinc, superoxide dismutase, a protein associated with neurodegenerative disorder amyotrophic lateral sclerosis.[179]

The crystal structure of protein thermolysin at the all-atom resolution (PDB ID 1KEI) was first coarse-grained into the MARTINI CG resolution. For the ElNeDyn2.2 model, the recommended force constant of 500 kJ/mol/nm2 was employed along with the upper distance of 0.9 nm for neighboring noncovalent contacts. The elastic network model was also applied to the $Zn^{2+}$ and $Ca^{2+}$ ions of thermolysin. The topology files for the GōMartini 2.2 model was generated using the program go_martinize.py [178] and the epsilon value of 9.414 kJ/mol. [180] The program

go_martinize.py was modified such that the neighboring contact map was built up to a cut-off distance of 1.1 nm. [179, 180] The GōMartini model was also applied to the $Zn^{2+}$ and $Ca^{2+}$ ions of thermolysin.

### 4.4.12 MARTINI CG Simulations on PBP-Thermolysin Complexes

Provided the force field developed for the PBP chains and the model in protein activity study, the MARTINI CG simulations were subsequently carried out to study the binding behavior of thermolysin and PBPs. In each of the systems, there existed one protein and 12 PBP chains, which were dissolved in a water box with 0.14 M NaCl. The ratio of 1 thermolysin to 12 PBP chains agreed with the experimental concentrations. Two PBPs, poly(PepNorIm$_{15}$) and poly(PepMAm$_{15}$), were investigated here.

The thermolysin protein was first put at the center of a cubic box with an edge length of 16 nm. 12 PBP chains were randomly inserted in the box, which was then filled with MARTINI water molecules and 0.14 M NaCl. During the equilibration, the protein backbone particles were restrained to their initial positions. A simulation of 2 ps was first performed with the integration time step of 2 fs and position restraint force constant of 1000 kJ/mol/nm$^2$, which was followed by a simulation of 10 ps with the time step of 10 fs and the position restraint force constant of 200 kJ/mol/nm$^2$, then by a simulation of 15 ps with the time step of 15 fs and the position restraint force constant of 50 kJ/mol/nm$^2$, and lastly by a simulation of 10 ps with the time step of 20 fs and the position restraint force constant of 10 kJ/mol/nm$^2$. Subsequently, the position restraints were removed, and each simulation lasted 18 μs. The ElNeDyn2.2 model was employed for thermolysin for the first 9 μs, which stabilized the binding of PBP chains and protein while preserving the

protein structure. The GōMartini 2.2 model was then applied for the last 9 μs, which was employed to take into account possible protein configuration change upon PBP binding. The simulation parameters were the same as those employed in developing the MARTINI parameters for the PBP backbone particles. The convergence of the simulations was validated by the calculated potential energies between protein and PBP peptides and between protein and PBP backbones.

Further calculations demonstrated that the PBP-thermolysin binding showed no noticeable impacts on the thermolysin structure and the PBP structures. Therefore, the SASA obtained from the all-atom simulations on PBPs in the absence of protein could be employed in predicting their interactions with proteins.

# Chapter 5. Bioactive Peptide Brush Polymers via Photoinduced Reversible-Deactivation Radical Polymerization

This chapter is adapted from the following publication:

Sun, H.†, Choi, W.†, Zang, N., Battistella, C., Thompson, M. P., Cao, W., Zhou, X., Forman, C., Gianneschi, N. C. Bioactive Peptide Brush Polymers via Photoinduced Reversible-Deactivation Radical Polymerization, *Angew. Chem. Int. Ed.*, **2019**, 58, 17359-17364. ("†" denotes authors equally contributed.)

## 5.1 Introduction

The convergence of photochemistry and controlled polymerization techniques has led to the development of new living polymerization systems, post-polymerization modifications, and production of advanced materials.[181-185] In comparison with common triggers for polymerizations such as heat and chemicals, light has shown unique advantages including mild reaction conditions, non-invasiveness, and the ability to provide spatiotemporal control over the polymerizations.[186-189] The toolbox of photo-induced controlled polymerization techniques is expanding, giving rise to photo-induced reversible deactivation radical polymerization (photo-RDRP), photo-induced ring-opening metathesis polymerization (photo-ROMP),[190] photo-controlled cationic polymerization,[191-193] and photo-triggered ring opening polymerization (photo-ROP) of cyclic esters or *N*-carboxyanhydride.[194] Among these photo-induced polymerization methods, photo-RDRP techniques have received the most interest due to their broad vinyl monomer scope and relatively mild reaction conditions conducted at room temperature, in a metal-free systems, and

with high tolerance to oxygen and water.[195] We reasoned that these mild conditions should provide a route for the incorporation of peptide-based vinyl monomers into bioactive, highly functionalized polymers, and polymeric materials. The mild conditions would minimize side reactions and thus retain the integrity of the biomolecules during polymerization and provide clean materials following polymerization.[196]

Photo-electron transfer reversible addition-fragmentation transfer polymerization (PET-RAFT) represents a powerful tool in the arsenal of photo-RDRP approaches.[182] This technique can be performed under visible blue or green light in the presence of a biocompatible organo-photocatalyst such as eosin Y.[186] More generally, RAFT polymerization has proven tolerance towards many functional groups pendent on monomers.[197] Therefore, we postulated that PET-RAFT could serve as an ideal photo-RDRP approach to explore photo polymerization of peptide-containing vinyl monomers.

The multi-valent display of peptides as side chains in brush polymers can lead to materials with enhanced biological activities such as higher binding affinity and cell-penetration.[198-200] Examples include peptide brush polymers prepared via ROMP and atom transfer radical polymerization which involve the use of ruthenium and copper-based catalysts.[201, 202] The possibility of residual heavy metals remaining after synthesis raises concerns in biomedical applications. Herein we demonstrate a metal-free photo-RDRP approach to peptide brush polymers (Figure 5.1). Two bioacitive peptide vinyl monomers featuring enzyme-responsive and pro-apoptotic amino acid sequences were successfully copolymerized with dimethylacrylamide (DMA) via PET-RAFT protocol in both organic and aqueous solutions. The incorporation of DMA comonomer not only lessened the steric hindrance from peptide macromonomer, but also

facillitated the preparation of peptide brush polymers with different grafting densities. Furthermore, the robust nature of the PET-RAFT technique allowed access to various architectures including brush and linear-brush diblock polymers consisting of enzyme-responsive peptide side chains. Linear-brush diblock copolymers self-assembled into micelles, capable of further morphing into worm-like structure upon treatment with thermolysin. By variation of the grafting density of pro-apoptotic peptide, the cellular endocytosis efficiency and cytotoxicity of peptide brush polymers can be controlled, revealing the crucial role of architecture (i.e., grafting density) in governing the bioactivities of polypeptide brushes. These results highlight the potential of photo-RDRP for the design of peptide brush polymer materials with well-defined structures and highly tunable properties in biomedical applications.

## 5.2 Results and Discussion

### 5.2.1 Synthesis of Bioactive Peptide Monomers

Peptide monomers containing an acrylamide moiety, which serves as the polymerizable group for radical polymerization were synthesized by addition of acrylic acid to an amino-hexanoic spacer unit on the *N*-terminus of the peptide chain (Figure 5.1).

Two amino acid sequences were chosen to prepare two proof-of-concept systems. The first is the sequence GLPGLAGG, a known substrate for various proteolytic enzymes including thermolysin.[19] The other is a sequence KLAKLAKKLAKLAK, which, when internalized, triggers apoptosis of cancer cells by mitochondrial membrane disruption.[203] The chemical structure and purity of the peptide monomers (PepAm and KLAAm in Figure 5.1) were verified by high

performance liquid chromatography (HPLC), $^{1}$H NMR spectroscopy, and electrospray ionization mass spectrometry (ESI-MS).

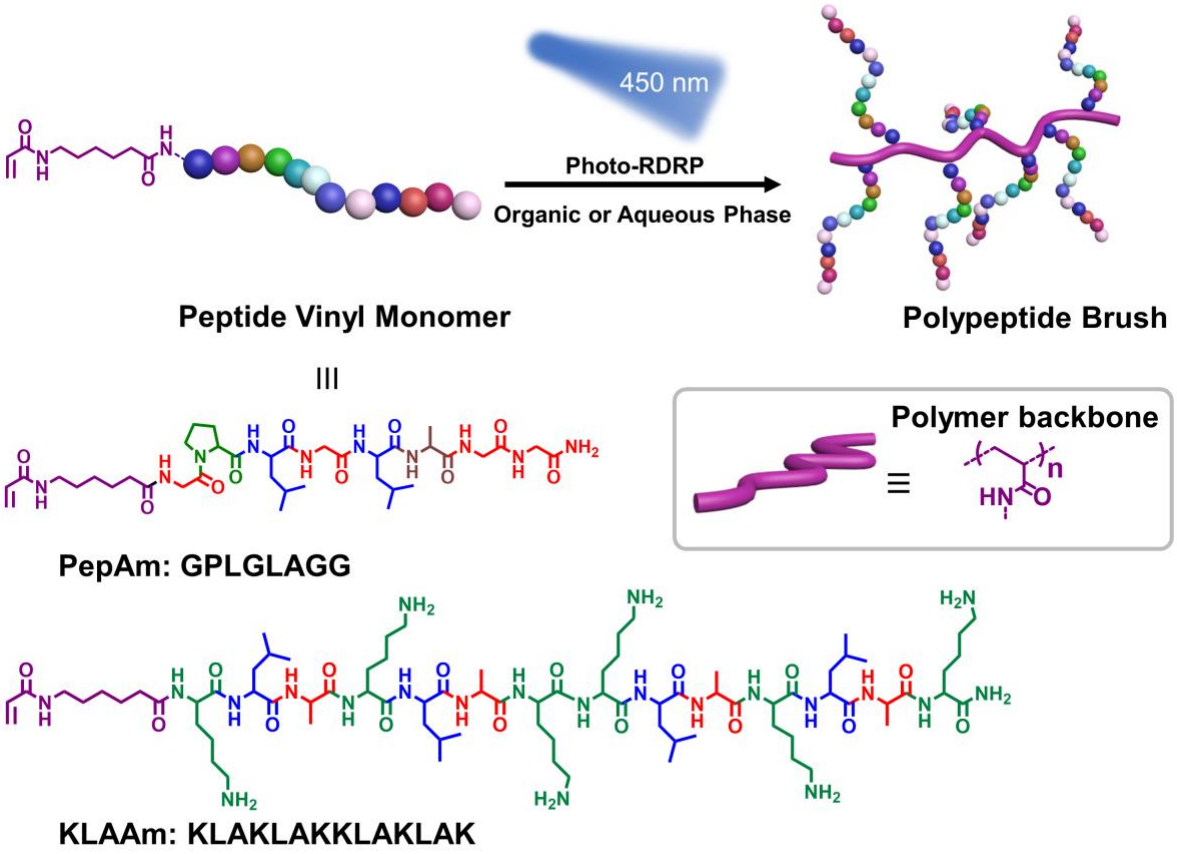


**Figure 5.1** Schematic of the synthesis of peptide brush polymers *via* photo-RDRP. Two bioactive peptide vinyl monomers are designed and presented in this study, including thermolysin-responsive amino acid sequence GPLGLAGG, and pro-apoptotic peptide KLAKLAKKLAKLAK. Copyright 2019 Wiley-VCH Verlag GmbH & Co. KGaA, Weinheim.[1]

### 5.2.2 Photo-RDRP of PepAm and DMA in organic solvent

Due to the steric bulk of the peptide macromonomers, we reasoned that random copolymerization with a spacer monomer would enhance overall monomer conversions as well as improve control over the course of photo-RDRP. To examine this, the homopolymerization of PepAm in DMSO was first conducted. According to the kinetics, no polymerization was observed after 18 hours, suggesting that steric hindrance stemming from the peptide side chains significantly hampered the photo-RDRP process. In view of this, a comonomer, dimethyl acrylamide (DMA) was employed in the preparation of enzyme-responsive polypeptide brushes. DMA was chosen due to its similar vinyl substructure (i.e., acrylamide) in comparison with the peptide monomer (Figure 5.2)

To understand the composition and distribution of PepAm and DMA in the polymers, $^{1}$H NMR was used to study the rate of polymerization and conversion of the two monomers in photo-RDRP under blue LED. According to $^{1}$H NMR analysis (Figure 5.2 B), both the peptide monomer and DMA comonomer had similar propagation rates, indicative of statistic distribution of peptide grafts on the polymer backbone. Gel permeation chromatography (GPC) analysis demonstrated the narrow molecular weight distribution of all polypeptide brushes with different grafting densities (Figure 5.2 C). Moreover, theoretical molecular weights of all polymers are on par with those from GPC results, suggesting good control over the photo polymerizations. While full monomer conversions were not achieved, residual PepAm and DMA monomers were effectively removed by dialysis of the crude polymer mixtures in water, as confirmed by its disappearance in the GPC trace. Natural sun-light was also able to trigger the photo polymerization of PepAm, leading to well-defined polypeptide brushes.

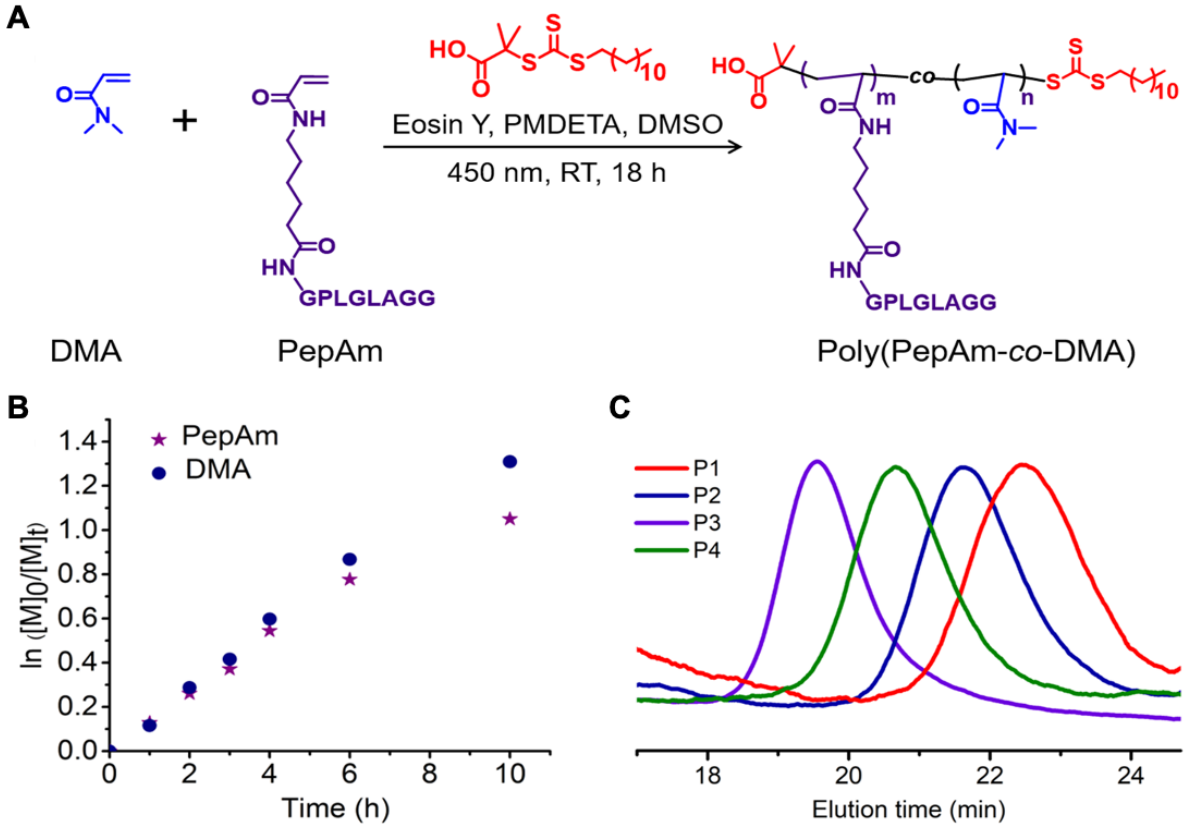


**Figure 5.2** Copolymerization of PepAm and DMA monomers in organic solvent. (A) Photo-RDRP of PepAm and DMA in DMSO. (B) Kinetic plot of concentration versus time for PepAm and DMA over the course of photo-RDRP. (C) GPC traces of enzyme-responsive peptide brush polymers with different grafting densities. Copyright 2019 Wiley-VCH Verlag GmbH & Co. KGaA, Weinheim.[1]

### 5.2.3 *In Vitro* Assessment of poly(PepAm-co-DMA) : Enzyme Responsive Shape-Shifting Nanoparticles

To examine the bio-activity of polypeptide brushes, polymer poly(PepAm$_{21}$-*co*-DMA$_{71}$) (P4) was treated with thermolysin, an enzyme that can selectively cleave the amide bond between glycine (G) and leucine (L) (Figure 5.3). HPLC was employed to monitor the cleavage experiment,

and showed that the polypeptide brushes were rapidly cleaved within 1 hour under the investigated condition. The cleaved peptide fragment was analyzed by ESI-MS and shown to have the identical mass to that of the genuine synthetic cleavage fragment LAGG. These results clearly indicate that the side-chain peptides remain accessible and reactive towards enzyme cleavage following polymerization.

To capitalize on this accessibility to substrate, amphiphilic block copolymers were prepared by chain extension of poly(methyl methacrylate) or poly(n-butyl acrylate) based macro chain transfer agents with PepAm and DMA. The resulting amphiphilic diblock copolymers assembled into micelles in water. For example, $PMMA_{90}$-*b*-poly($PepAm_{21}$-*co*-$DMA_{63}$) (P8) were spherical micelles, 24 nm in diameter as characterized by transmission electron microscope (TEM), in good agreement with the hydrodynamic diameter (28 nm) determined by dynamic light scattering (DLS) (Figures 5.3 B and D).

The critical packing parameter (CPP) dictates the thermodynamic morphology of amphiphilic block copolymers. In principle, a higher CPP (> 1/3) can lead to the formation of higher order morphologies such as cylinders and bilayer vesicles.[204] Since polypeptide brush polymer P4 showed rapid cleavage in the presence of thermolysin (vide supra), we suspected that the micelles formed from polypeptide containing diblock polymers could respond to thermolysin, resulting in truncation of the hydrophilic polypeptide corona and thus a reduction in interfacial curvature (i.e., increment in CPP), leading to a change in morphology. Indeed, TEM and DLS showed that the spherical micellar structure of P8 underwent metamorphosis into a worm-like phase upon treatment with thermolysin (Figures 5.3 C and D). By contrast, no change in diameter was observed for particles treated under the same cleavage conditions using deactivated

thermolysin which had been pretreated with ethylenediaminetetraacetic acid (Figure 5.3 D). In addition, similar morphological transformations were observed in other block copolymer micelles including PMMA$_{90}$-*b*-poly(PepAm$_{9}$-*co*-DMA$_{30}$) (P7) and PnBA$_{200}$-*b*-poly(PepAm$_{36}$-*co*-DMA$_{123}$) (P9), demonstrating the versatility of this approach to enzyme-responsive shape-shifting nanoparticles.

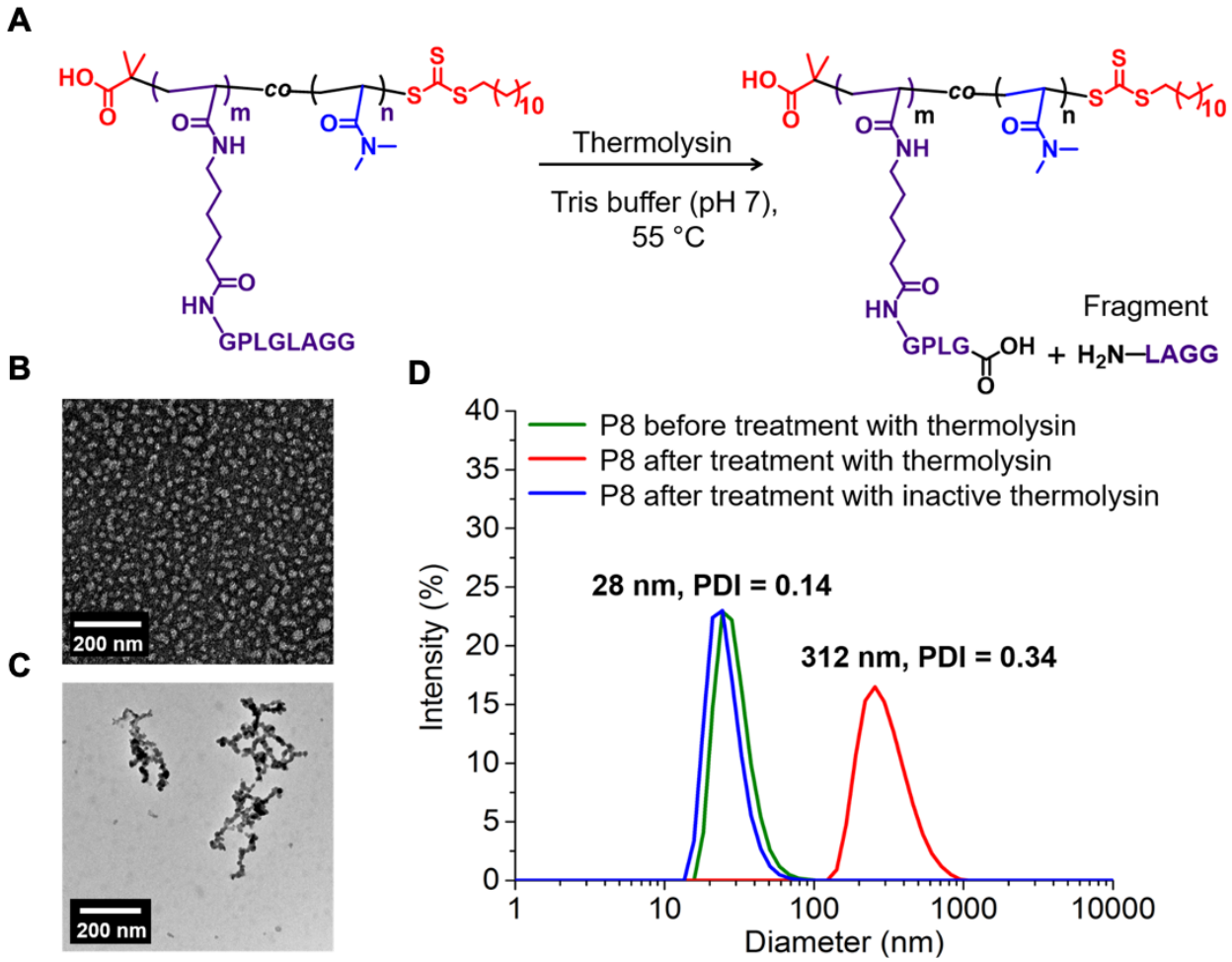


**Figure 5.3** Enzyme responsiveness of poly(PepAm-co-DMA). (A) Schematic of thermolysin-promoted cleavage of poly(PepAm$_{21}$-*co*-DMA$_{71}$) (P4) (b) TEM micrograph of PMMA$_{90}$-*b*-poly(PepAm$_{21}$-*co*-DMA$_{63}$) based micelles (P8) before treatment with thermolysin. (C) TEM micrograph of PMMA$_{90}$-*b*-poly(PepAm$_{21}$-*co*-DMA$_{63}$) based micelles (P8) after treatment with thermolysin. (D) DLS traces of P8 based nano-objects before and after thermolysin-induced cleavage. Copyright 2019 Wiley-VCH Verlag GmbH & Co. KGaA, Weinheim.[1]

### 5.2.4 Photo-RDRP of PepAm and KLAAm in aqueous solvent.

The ability to conduct polymerizations directly in water is of significant interest to the field of biomedical polymer materials, as it not only avoids the use of toxic organic solvents but also eliminates the time-consuming step of transferring the polymeric materials from the organic to aqueous phase. To explore the feasibility of aqueous photo-RDRP of peptide monomers, we examined the photo-RDRP of both enzyme-responsive peptide acrylamide (PepAm) and pro-apoptotic KLA peptide acrylamide (KLAAm) in water. Table 5.1 summarizes the polymerization results for PepAm and DMA, indicating dramatically higher monomer conversions in water compared to those obtained by photo-polymerizations in DMSO. We hypothesize that this is due to the enhanced solubility of PepAm in aqueous solution. Polymers (P10-P12) were analyzed by GPC and NMR and showed molecular weights that were in good agreement with theoretical values, confirming that photo-RDRP of PepAm was unaffected under aqueous conditions.

| | Equiv. to CTA | | | Conv. (%) | | | | |
|---|---|---|---|---|---|---|---|---|
| Entry | PepAm | DMA | $[M]_0$ | PepAm | DMA | $M_{n,theo}$ (g/mol) | $M_{n,GPC}$ (g/mol) | $Đ$ |
| [a]P10 | 50 | 50 | 0.36 M | 60% | 64% | 27 685 | 26 100 | 1.06 |
| [a]P11 | 50 | 100 | 0.54 M | 87% | 85% | 44 230 | 48 700 | 1.01 |
| [a]P12 | 50 | 150 | 0.72 M | 92% | 94% | 51 388 | 55 400 | 1.04 |

**Table 5.1** Aqueous photo-RDRP of PepAm and DMA. In each polymerization, 200ul of DIW was used. [M]/[CTA]/[EY]/[PMDETA] = X/1/0.05/1. [a]The polymerizations were triggered by blue LED.

For the KLAAm monomer, which contains abundant amine groups, acetate buffer (pH 5) was utilized to fully protonate the amine groups, reducing their nucleophilicity (pKa = 9) and thus precluding undesired aminolysis of the chain transfer agents (Figure 5.4). By adjusting the feed ratio of DMA to KLAAm, polypeptide brushes with various grafting densities of KLA side chains were prepared. Based on NMR analysis, monomer conversions were quantitative for all random copolymerizations of DMA and KLAAm. However, the homopolymerization of KLAAm only led to a modest monomer conversion (40%) possibly due to the steric bulk of the KLA peptide macromonomer. The narrow and symmetric GPC traces of KLA based polypeptide brushes indicates good control over the aqueous photo-RDRP of KLAAm (Figure 5.4 B). Furthermore, the secondary structure of KLA peptides and brush polymers were assessed by circular dichroism (CD) spectroscopy, which showed a mixture of α-helix and random coil. More importantly, the spectra of the KLA monomer and resulting polymers are identical, suggesting the polymerization process does not alter the secondary structure of the peptide (Figure 5.4 C).

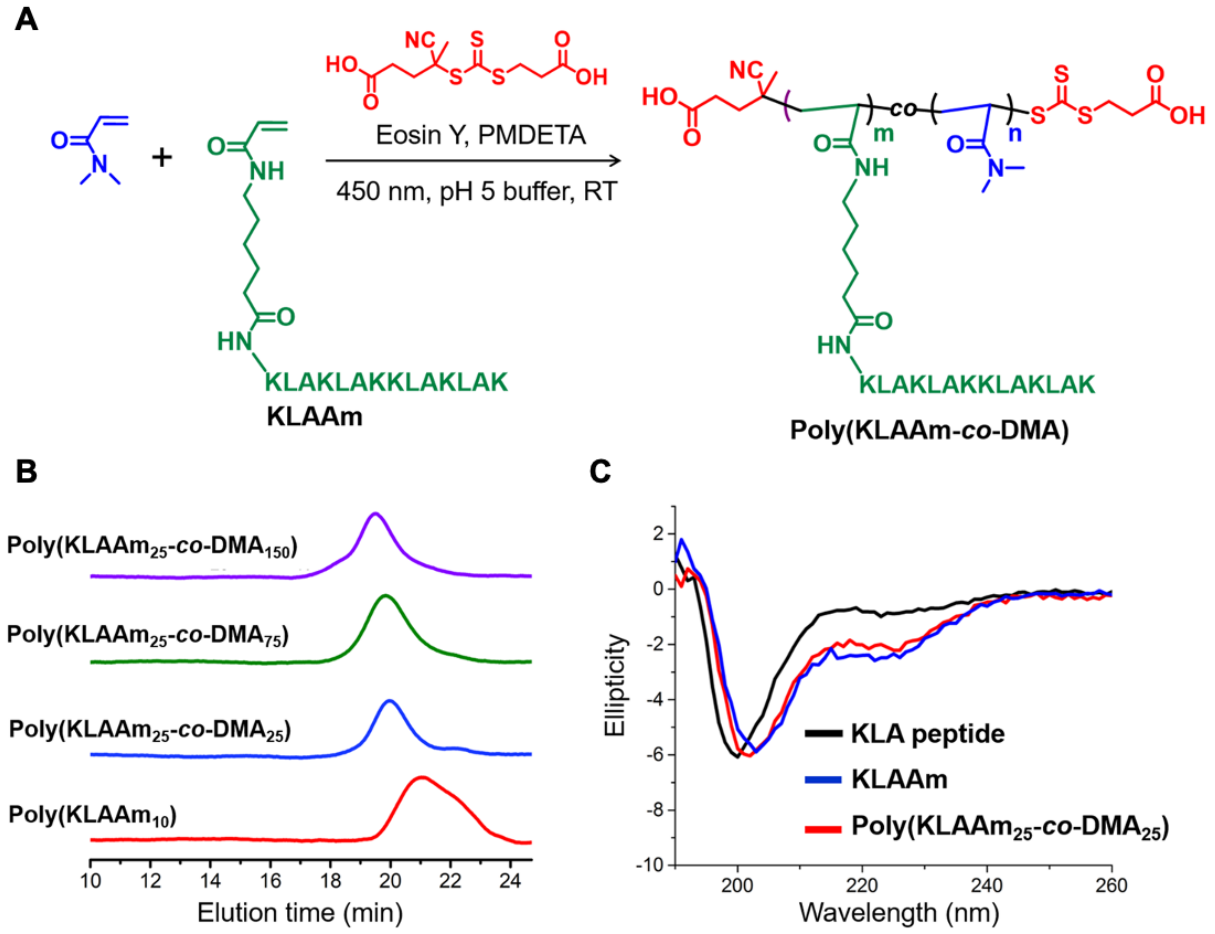


**Figure 5.4** Polymerization of KLA monomers in aqueous solvent. (A) Aqueous photo-RDRP of KLAAm and DMA in acidic buffer (pH 5) (B) GPC traces of KLA based peptide brush polymers with different grafting densities (P13-P16) (C) Circular dichroism spectra of KLA peptide, KLAAm, and poly(KLAAm$_{25}$-*co*-DMA$_{75}$). Copyright 2019 Wiley-VCH Verlag GmbH & Co. KGaA, Weinheim.[1]

### 5.2.5 *In Vitro* Assessment of poly(KLAAm) : Pro-Apoptosis of poly(KLAAm)s with Different Grafting Density

The KLA peptide sequence used in these studies is a known pro-apoptotic peptide which is capable of inducing cell apoptosis via disruption of mitochondrial membranes.[205] It is typically fused with a cell-penetrating peptide because of its poor cell uptake. The KLA based brush polymers, while lacking a cell-penetrating peptide moiety, possess a great number of cationic charges which could enhance the affinity to the negatively charged cell membrane and consequently promote delivery of the KLA based polymer brushes into cells. To elucidate the role of KLA grafting densities in governing the cellular uptake and cytotoxicity of KLA brush polymers, we conducted *in vitro* cell studies of different brush polymers (P13-P16) in HeLa cells (Figures 5.5-5.7). Flow cytometry assay was utilized to quantify the cell uptake efficiency of brush polymers. All KLA peptide brush polymers show significantly more cellular uptake compared to the free peptide. This observation is consistent with the multivalency effect of KLA peptides stemming from polypeptide brushes, which enhanced the affinity and cell uptake of KLA containing materials. In addition, cell internalization of densely grafted polypeptides including poly($KLAAm_{25}$-*co*-$DMA_{25}$) and poly($KLAAm_{10}$) clearly outperformed those loosely grafted polypeptide brushes such as poly($KLAAm_{25}$-*co*-$DMA_{75}$) (Figures 5.5). The cell uptake behaviors of KLA peptide and polymer brushes were further studied by confocal laser scanning microscopy (CLSM). Cells treated with rhodamine labeled KLA peptide showed no uptake even at a high concentration (50 μM with respect to peptide). On the other hand, the cellular uptake of all the KLA peptide brush polymers was clearly visible at the same peptide concentration, as evidenced

by the increase in rhodamine fluorescence inside the Hela cells (Figures 5.6). Finally, cytotoxicity assays demonstrated that KLA based polymer brushes had significantly higher cytotoxicity than either the free KLA peptide or the KLAAm monomer (Figure 5.7). Notably, the cytotoxicity of polypeptide brushes was dependent on the grafting densities of KLA peptides. As the grafting density of KLA peptide increased and the polymer brushes became more compact, the IC50 values decreased. Those cytotoxicity results unequivocally corroborate cell uptake behavior of KLA brush polymers bearing different grafting densities.

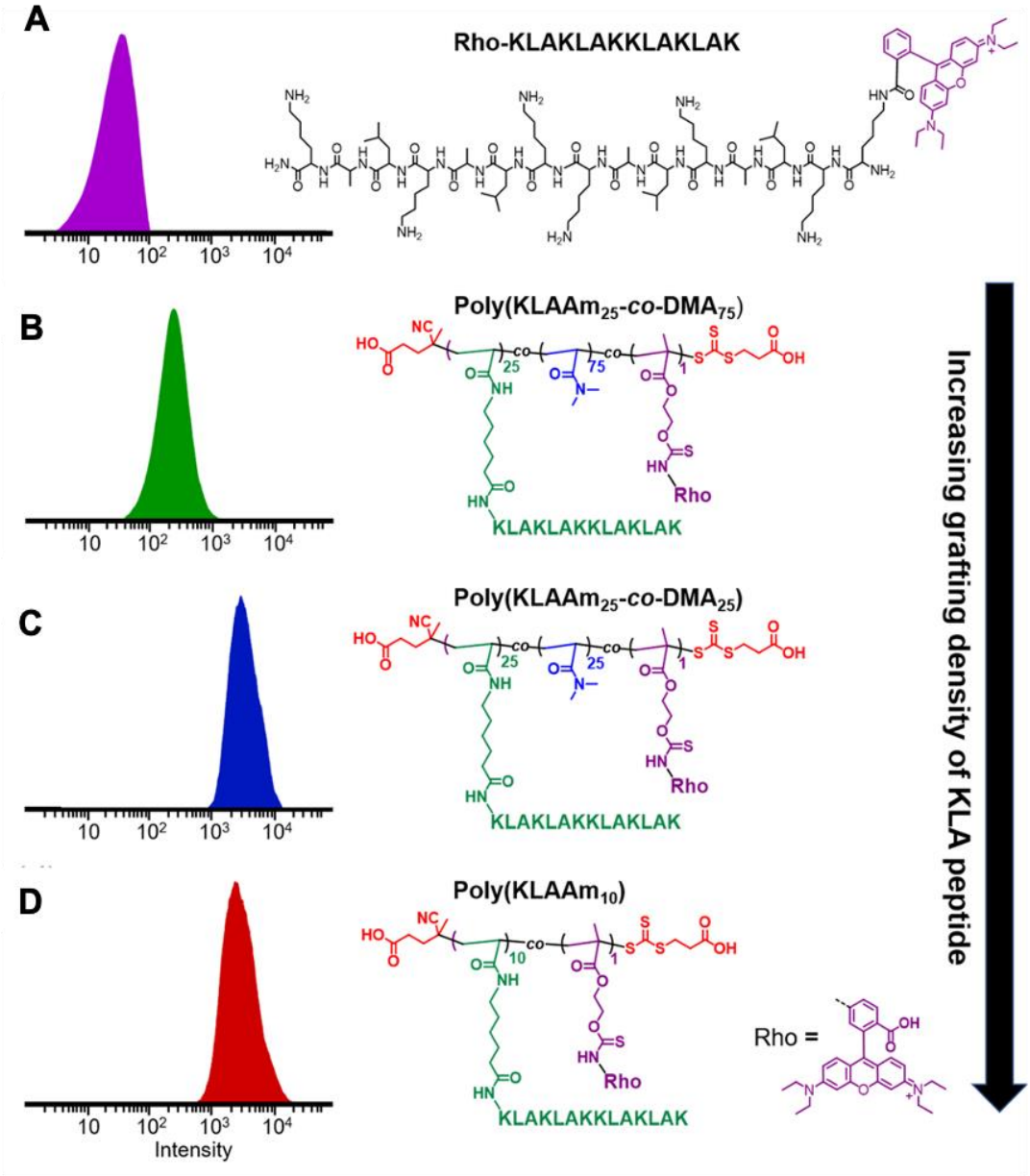


**Figure 5.5** Flow cytometry analysis of HeLa cells incubated with rhodamine labeled KLA peptide and polymers. (A) rhodamine B-labeled KLA peptide, (B) poly(KLAAM$_{25}$-*co*-DMA$_{75}$), (C) poly(KLAAM$_{25}$-*co*-DMA$_{25}$), and (D) poly(KLAAM$_{10}$) at a concentration of 0.25 μM with respect to the dye. Chemical structures of each dye-labeled materials are shown adjacent to the corresponding histogram. KLA based peptide brush polymers possessed markedly higher cell uptake ability than that of KLA peptide. Copyright 2019 Wiley-VCH Verlag GmbH & Co. KGaA, Weinheim.[1]

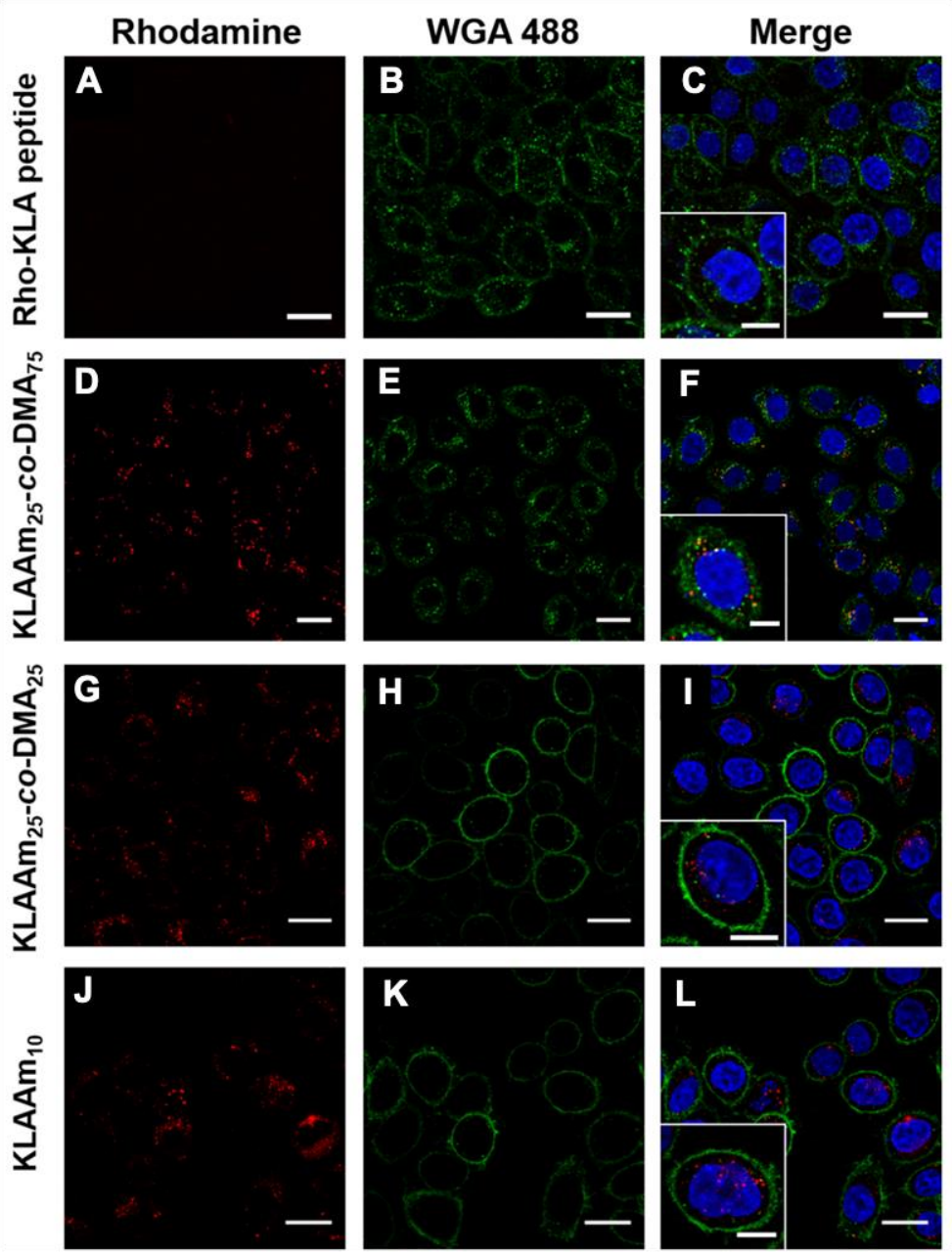


**Figure 5.6** Confocal laser scanning microscopy images of Hela cells treated with rhodamine-labeled peptide based materials. From top to bottom: KLA peptide (A-C), poly(KLAAm$_{25}$-*co*-DMA$_{75}$) (D-F), poly(KLAAm$_{25}$-*co*-DMA$_{25}$) (G-I), and poly(KLAAm$_{10}$) (J-L). Cell nuclei were stained with DAPI. Cell membrane was stained with WGA 488. Scale bar: 20 µm, inset scale bar 10 µm. Copyright 2019 Wiley-VCH Verlag GmbH & Co. KGaA, Weinheim.[1]

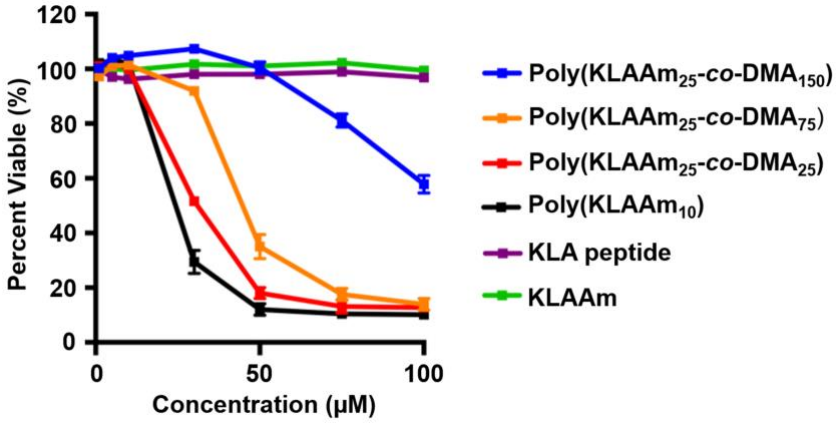


**Figure 5.7** Cytotoxicity assay of KLA peptide, KLAAm, and a library of KLA based peptide brush polymers with different grafting densities. KLA peptide and KLAAm did not exhibit cytotoxicity to Hela Cells even at a concentration of 100 μM. The IC 50 value of peptide brush polymers decreased as the grafting density of peptide brush polymer increased, indicating a higher cytotoxicity of KLA peptide brush polymers with a more compact brush architecture. Copyright 2019 Wiley-VCH Verlag GmbH & Co. KGaA, Weinheim.[1]

## 5.3 Conclusion

In summary, we present several examples of photo-RDRP of peptide acrylamide monomers. This is a robust synthetic approach to prepare bioactive polypeptide brushes under mild conditions using visible light, in aqueous solution, and at room temperature. We envision that a wide variety of other functional peptide monomers will be compatible with this technique. Moreover, we demonstrated the important role that the architecture (i.e., grafting density) of peptide brush polymers has on functions such as cell penetration and cytotoxicity to cancer cells. Given the widespread interest in peptides as therapeutics and targeting moieties in biomedicine, we envision these mild synthetic procedures will open the door to entirely new peptide brush polymer materials.

## 5.4 Experimental Details

### 5.4.1 Preparation of Peptide Monomers via Solid-Phase Peptide Synthesis (SPPS)

Peptides were synthesized on Rink resins (0.67 mmol/g) using standard FMOC SPPS procedures on an AAPPTec Focus XC automated synthesizer. A typical SPPS procedure included deprotection of the *N*-terminal Fmoc group with 20 % 4-methyl-piperidine in DMF (1 × 20 min, followed by 1 × 5 min), and 30 min amide couplings (twice) using 3.0 equiv. of the Fmoc-protected amino acid, 2.9 equiv. of HBTU and 6 equiv. of DIPEA. After that, peptide monomers were prepared by amide coupling to Fmoc-6-aminohexanoic acid, followed by Fmoc deprotection and final amidation with acrylic acid (3 equiv.) in the presence of HBTU (2.9 equiv.), and DIPEA (6 equiv.).

### 5.4.2 Photo-Polymerization in DMSO

In a typical organic phase photo-induced polymerization (P1), peptide (GPLGLAGG) acrylamide monomer (30 mg, 50 equiv.) and DMA (3.7 mg, 50 equiv.) were dissolved in 150 μL of DMSO. Then 10 μL (1.0 equiv.) of DDMAT stock solution (2.7 mg in 100 μL of DMSO) was added into the reaction mixture. Following that, 10 μL (0.05 equiv.) of eosin Y disodium salt stock solution (2.6 mg in 1 mL of DMSO) and PMDETA (0.13 mg, 1.0 equiv.) were added. The solution was degassed by $N_2$ flow for 30 min and then placed into the photo-reactor (450 nm, 2.8 mW/cm$^2$) for 24 h. Upon the polymerization, the polymer product was purified by dialysis into DIW, followed by lyophilization.

### 5.4.3 Photo-Polymerization in Aqueous Solution

In a typical aqueous photo-induced polymerization (P14), KLA peptide (KLAKLAKKLAKLAK) acrylamide monomer (30 mg, 25 equiv.) and DMA (1.8 mg, 25 equiv.) were dissolved in 150 μL of acetate buffer (0.1 M, pH 5). Then 10 μL (1.0 equiv.) of water-soluble RAFT agent stock solution (2.2 mg in 100 μL of acetate buffer) was added into the reaction mixture. Following that, 10 μL (0.05 equiv.) of eosin Y disodium salt stock solution (2.5 mg in 1 mL of acetate buffer) and PMDETA (0.12 mg, 1.0 equiv.) were added. The solution was degassed by $N_2$ flow for 30 min and then placed into the photo-reactor (450 nm, 2.8 mW/cm$^2$) for 24 h. Upon the polymerization, the polymer product was purified by dialysis into DIW, followed by lyophilization.

### 5.4.4 Preparation of Rhodamine-Labeled Polymers

In all the cases of preparing rhodamine-labeled polymers, one equiv. of rhodamine B to RAFT agent was used, ensuring that average one dye was attached per polymer chain. In a typical polymerization (rhodamine-labeled P14), KLA peptide (KLAKLAKKLAKLAK) acrylamide monomer (30 mg, 25 equiv.), DMA (1.8 mg, 25 equiv.), and methacryloxyethyl thiocarbamoyl rhodamine B (0.48 mg, 1.0 equiv.) were dissolved in 150 μL of acetate buffer (0.1 M, pH 5). Then 10 μL (1.0 equiv.) of water-soluble RAFT agent stock solution (2.2 mg in 100 μL of acetate buffer) was added into the reaction mixture. Following that, 10 μL (0.05 equiv.) of eosin Y disodium salt stock solution (2.5 mg in 1 mL of acetate buffer) and PMDETA (0.12 mg, 1.0 equiv.) were added. The solution was degassed by $N_2$ flow for 30 min and then placed into the photo-reactor (450 nm,

2.8 mW/cm$^2$) for 24 h. Upon the polymerization, the polymer product was purified by dialysis into DIW, followed by lyophilization.

### 5.4.5 *N*-Acetylation of poly(KLAAm-*co*-DMA)

In a typical procedure, poly(KLAAm-*co*-DMA) (1.0 equiv. with respect to free amines) was dissolved in DMF and then treated with 50 equiv. of acetic acid in the presence of 50 equiv. of EDC•HCl and 5 equiv. of 4-DMAP. The reaction mixture was stirred for 12 hours, followed by dialysis into DIW wand lyophilization.

### 5.4.6 Thermolysin-Induced Cleavage Experiments

For enzyme-triggered cleavage experiments, the molar ratio of thermolysin to peptide was set to 1: 300. Moreover, the temperature was set to 55 °C to achieve the optimal activity of thermolysin. For example, poly(PepAm$_{21}$-*co*-DMA$_{24}$) (P4, 1 mg, 0.87 µmol with respect to peptides, 300 equiv.) was dissolved in 1 ml of DPBS solution. Then thermolysin (0.1 mg, 2.9 nmol, 1 equiv.) was added into the polymer solution which was stirred in a preheated oil bath at 55 °C. In the case of control experiment which involved using deactivated thermolysin, EDTA (100 equiv. to thermolysin) was utilized to capture the zinc and calcium ions, resulting in denaturing of thermolysin.

### 5.4.7 Cell Culture

Hela cells were purchased from ATCC. Cells were cultured at 37 $^o$C under 5% $CO_2$ in phenol-red containing Dulbecco`s Modified Eagle Medium (DMEM; Gibco Life Tech., cat.

#11960-044) supplemented with 10% fetal bovine serum (Omega Scientific, cat. #11140-050), sodium pyruvate (Gibco Life Tech., cat. #35050-061), L-glutamine (Gibco Life Tech., cat. #35050-061), and the antibiotics penicillin/streptomycin (Corning Cellgro, cat. #30-002-C1). Cells were grown in T75 culture flasks and subcultured at ~75-80% confluency.

### 5.4.8 Cell Viability Assay

The cytotoxicity of materials was assessed using the CellTilter-Blue assay. HeLa cells were plated at a density of 5000 cells per well of a 96 well plate 18 hours prior to treatment. Materials were dissolved in DPBS with desired concentration and added to the wells along with a 10% DMSO positive control. Cells were incubated for 72 hours at 37 ºC. Note that the concentration of all the materials is respected to the peptide concentration to ensure that all peptides and polymers are fairly compared with respect to their therapeutic components. The medium was removed and 80 μL of new medium without phenol red was added followed by adding 20 μL of CellTilter-Blue reagent. The cells were incubated for 3 hours at 37 ºC. The fluorescence was measured at 560 nm excitation and 590 nm emission wavelength.

### 5.4.9 Confocal Laser Scanning Microscopy for Uptake in HeLa cells

HeLa cells were plated in a 4-chamber 35mm round glass-bottom dishes at a density of 50,000 per well. Cells were incubated for 24 hours in a 5% $CO_2$ atmosphere at 37 ºC. 500 μL of of KLA peptide, Poly(KLAAm$_{25}$-*co*-DMA$_{75}$), Poly(KLAAm$_{25}$-*co*-DMA$_{25}$), and Poly(KLAAm$_{10}$) (0.25 μM with respect to rhodamine for each material) in 10% FBS DMEM medium without phenol red were incubated with the cells for 24 hours, respectively. After washing with DPBS to

remove the residual peptides and polymers, 500 µL of Wheat Germ Agglutinin (5 µg/mL) conjugated with Alexa Fluor 488 was added to each well, then fixed with a 4% paraformaldehyde solution for 15 min at room temperature. The cells were washed with DPBS and stained by DAPI for 20 min at room temperature.

### 5.4.10 Flow Cytometry for Uptake Ability in HeLa cells

For cellular uptake measurement, HeLa cells were plated in 12-well plates at a density of 1,000,000 per well and incubated for 24 hours in a 5% $CO_2$ atmosphere at 37 $^oC$. 500 µL of 0.25 µM (with respect to rhodamine) KLA peptide, poly(KLAAm$_{25}$-*co*-DMA$_{75}$), poly(KLAAm$_{25}$-*co*-DMA$_{25}$), and poly(KLAAm$_{10}$) in 10% FBS DMEM medium without phenol red were incubated with the cells for 24 hours respectively. After triple washing with DPBS, 500 µL of 0.25% Trypsin-EDTA was added to each well for 10 min at 37 $^oC$. Cells were fixed with a 4% paraformaldehyde solution for 15 min at room temperature.

# Chapter 6. Protein-like Polymers for the Therapeutic Application : Neovascular Age-Related Macular Degeneration (nAMD)

## 6.1 Introduction

Neovascular age-related macular degeneration (nAMD) currently affects 11 million people in the US with approximately 90% of vision loss attributed to choroidal neovascularization (CNV), the key pathology of nAMD. CNV is characterized by the abnormal growth of blood vessels either underneath the retinal pigment epithelium (RPE) or at the sub-retinal space on top of the RPE. Vascular endothelial growth factors (VEGF) have been shown to be responsible for driving the growth of new blood vessels during nAMD. Current medication involves injections of anti-angiogenic VEGF antibodies into the vitreous cavity. Although this approach has found clinical success, several challenges remain: i) monthly anti-VEGF medications are expensive with an annual cost of $4.6 billion in the US, ii) only ~30% of patients treated with VEGF antagonists show significant improvement in vision, and iii) global prevalence of nAMD is projected to double in the next decade which will lead to greater number of patients with no improvement in visual acuity despite monthly anti-VEGF treatment.

TSP1 is an extracellular matrix protein that interacts with cell surface receptors and modulates several *in vivo* processes including angiogenesis. In immunohistochemical studies of post-mortem eyes, TSP1 is expressed in the retinal pigment epithelium (RPE), bruch`s membrane (BM), and choriocapillaris (CC), and its levels are reduced with age and further reduced in late stages of AMD,[206] shifting the balance toward a pro-angiogenic milieu. As the first endogenous protein inhibitor of neovascularization to be discovered, TSP1 inhibits angiogenesis in a variety of

different pathways: i) acting as a VEGF antagonist, ii) inducing cell apoptosis, and iii) modulation of cell proliferation and migration.[207] Notably, TSP1 limits neovascularization in vascular endothelial cells by inducing receptor-mediated apoptosis. CD36 is a membrane protein that mediates the uptake of oxidized lipids and regulates the anti-angiogenic activity of TSP-1. CD36-TSP1 interaction down-regulates the VEGF receptor-2 and antagonizes VEGF function.[208] Amongst the multifunctional domains within TSP1, the type-1 repeats domains bind to CD36. ABT898 is a synthetic peptide which mimics the TSP1 type-1 repeat. Synthetic peptides, such as ABT898, that mimic TSP-1 therapy, could inhibit angiogenesis. However, there are several challenges that limit the clinical use of therapeutic peptides. Peptides are prone to proteolysis, demonstrate rapid renal clearance, and are unable in many cases to cross cell membranes. To address these challenges, we highlight below a new innovative peptide packaging and delivery strategy to address challenges in nAMD therapies.

We propose a new methodology for protecting active peptides from proteolysis, while vastly improving pharmacokinetics, bioavailability and maintaining strong bioactivity. The approach packages peptides together as high-density brush polymers PLPs. These moieties have a globular, peptide-based structure, assembled around a hydrophobic core. These are brush polymers, with high density display of peptides for recognition and function. PLPs are generated by graft through polymerization of peptide-modified monomers. Polymerization of peptide-based monomers consisting of natural *L*-amino acids results in materials with peptides that resist proteolysis entirely for hours and days, versus minutes in the case of their monomeric analogues (i.e. ordinary, linear peptides). Computer modeling of PLPs shows that their globular nature serves to protect the peptides from being accessible to proteolytic enzymes.[198] In addition, the peptides

maintain their bioactivity, can be taken up by the cells and can function in the cytosol. This means that while proteases regard them as poor substrates, they can still engage target proteins, both intra- and extracellular. Given these observations, we hypothesize that polymerized peptides, while protected from proteolysis, maintain their intended biological function and that this phenomenon is a general feature of peptides arranges in this manner. If so, such an approach would provide a general, accessible route to the development of proteolytically-resistant peptides capable of performing functions inherent to the peptide, such as binding a receptor or ligand, initiating a signaling pathway, penetrating a cell, or inducing a therapeutic effect. We envision that such a strategy provides a feasible route for the preparation and delivery of peptides as therapeutics. Herein, we will seek to deploy this innovative technology for treatment of nAMD. These drugs will establish ABT898 as alternative therapeutic pathway for nAMD patients that our efforts in this project aim to address the critical need of (i) long-acting therapies for the treatment of nAMD, and ii) new therapies for patients that show no improvement in visual acuity after anti-VEGF medication.

## 6.2 Results and Discussion

### 6.2.1 Synthesis of ABT898 PLPs

We have synthesized four norbornene modified ABT898 (GVi(allo)SQIRP) sequences with different linkers and additional arginine amino acids (Figure 6.1). Different linkers were incorporated to compare the bioactivities of the cleavable (Ester PLP and Ester RR PLP) and non-cleavable (Amide PLP and Amide RR PLP) PLPs. Cell penetrating peptides, e.g. TAT sequences,

are short sequences that are rich in arginine residues and aid the cellular penetration of cargo via endocytosis. Therefore, to enhance the cellular penetration capacity of the PLPs we modified the C-terminus with arginine moieties (Ester RR PLP and Amide RR PLP). These norbornene functionalized ABT898 peptide sequences were then subjected to standard ring opening metathesis polymerization (ROMP) conditions to yield four different ABT898 PLPs.

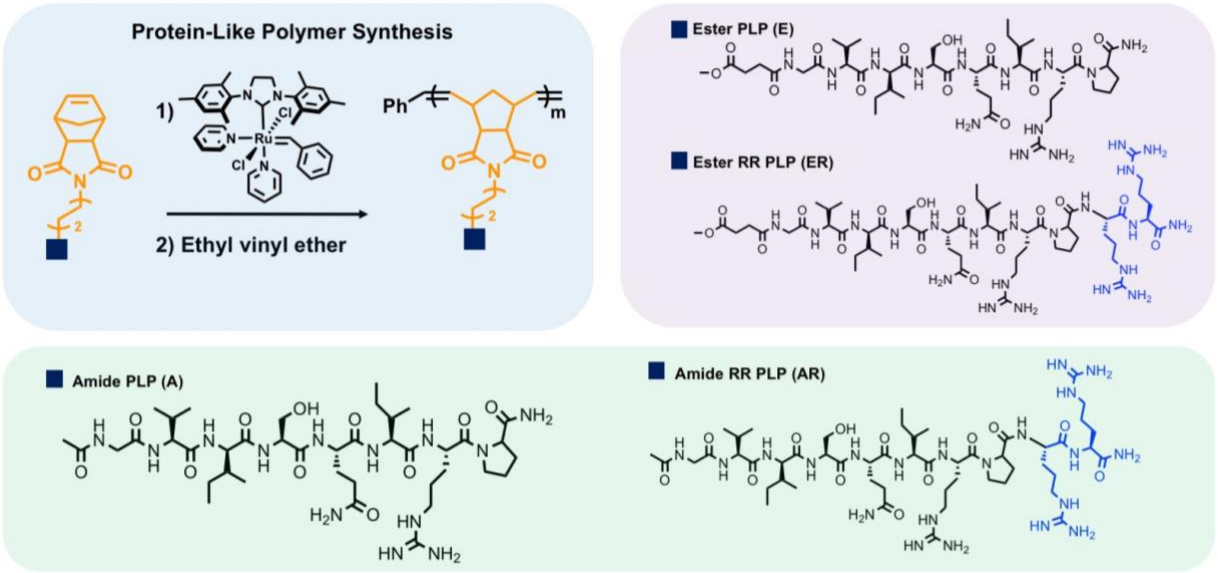


**Figure 6.1** Chemical structure and synthesis of Protein-like Polymers (PLP) with different ABT898 peptide monomers. Different linkers were incorporated; Amide (A) and Amide RR (AR): Non-cleavable amide linker, Ester (E) and Ester RR (ER): cleavable ester linker. Additional two arginines (blue) were incorporated in the original sequence to achieve increased cell penetration. Degree of polymerization, m, is 15 to 20.

### 6.2.2 Bioactivity Assessment of PLPs : Ex Vivo Choroidal Sprouting Assay

To determine the anti-angiogenic properties of the ABT898 PLPs, we performed an ex vivo choroidal sprouting assay. Briefly, eyes are enucleated, dissection is performed to remove the cornea, iris, lens, retina, and vitreous. The peripheral RPE-choroid-sclera complex is plated in

Matrigel, angiogenesis develops spontaneously over Day 4 – Day 7, and can be quantitated using reverse phase brightfield microscopy (Figure 5.2 A). ABT898 peptide had no effect upon choroidal angiogenesis (Figure 5.2 B). In addition, hydrolysable E and ER PLPs reduced angiogenesis only by 24% and 33%, respectively. In contrast, non-hydrolysable A and AR PLPs significantly decreased angiogenesis by 81% (A) and 91% (AR), respectively. This indicates that the non-cleavable, arginine modified ABT898 PLP has improved bioactivity compared to the original peptides. We believe this is because the peptide alone is degraded in the Matrigel milieu. In addition, AR PLP was far more anti-angiogenic than scrambled PLP and commercial aflibercept (Figure 5.2 D), indicating that the specific peptide sequence plays a crucial role in determining the extent of anti-angiogenic function.

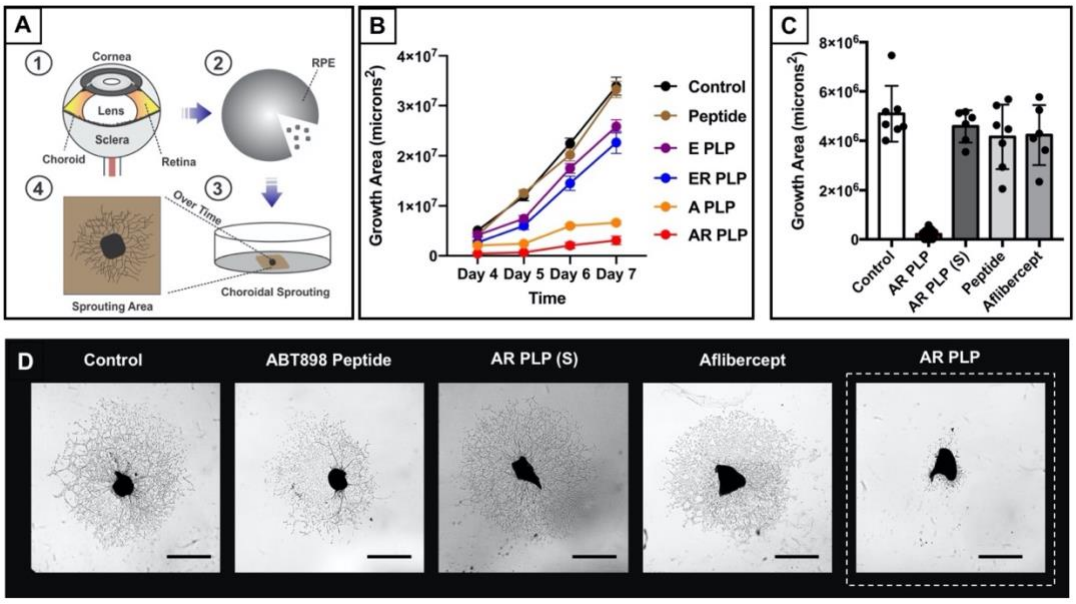


**Figure 6.2** Ex vivo choroidal sprouting assay. (A) Schematic illustration of the assay. (B) Time dependent assay of the growth area measured after the treatment of PLPs and peptides. (C) Growth area upon the treatment of PLP, scramble version of PLP (AR PLP(S)), peptide, and aflibercept at day 4. (D) Raw data: Light microscopy images of choroidal tissue upon treatment with buffer only, with parent peptide, scrambled PLP sequence, aflibercept, and the highly active ABT898 PLP with the amide linkage and two arginine residues included (AR PLP). Scale bar: 1 mm.

### 6.2.3 Enzyme Degradation Kinetics

An important feature of the PLP platform is that the globular structure of peptides arranged on a polymeric scaffold impart high proteolytic resistance. We performed an enzyme resistance assay to confirm that the PLP is resistant to proteolysis as compared to the peptide alone. Both peptide and PLP stock solutions (200 uM) were treated with thermolysin enzyme (0.1 uM) and their degradation profiles were monitored using high performance liquid chromatography (HPLC). We observed rapid degradation of the peptide to yield a fragment peak over time. However, the PLP peak does not change over time. We calculated the area under the peak at each time point to construct the percent cleaved and plotted it against time for both peptide and PLP (Figure 6.3).

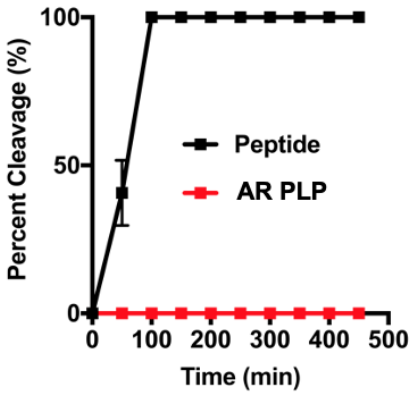


**Figure 6.3** Enzyme degradation kinetics of ABT898 peptide and AR PLP.

### 6.2.4 Binding Interaction of PLPs to CD36 Protein

Quantifying the ligand-receptor binding interaction is an important step in the development of these PLPs. Similar to surface plasmon resonance, bio-layer interferometry (BLI) is an optical method used to measure the affinity of ligand-receptor binding. BLI has three key advantages over existing techniques: i) samples can be easily recovered, ii) it uses less sample, and iii) it is high throughput. We proceeded to study the interaction of CD36 receptor with ABT898 peptide, A PLP, and AR PLP. Aqueous solutions of A PLP and AR PLP at various concentrations were assayed to study their binding with the CD36 receptor (Figure 6.4 B and C). As a negative control, we measured the binding of a ABT898 peptide. We recorded a dissociation constant in the$10^{-9}$ M range for AR PLP , $10^{-8}$M range for A PLP and $10^{-7}$ M for the ABT898 peptide (Figure 6.4 D). These data indicate that the PLPs have stronger affinity for CD36 receptor than ABT898 peptide, demonstrating the multivalent effect of PLP system.

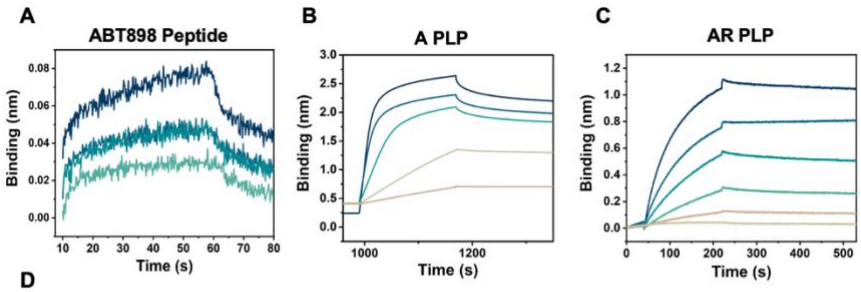


D

| | Peptide | A PLP | AR PLP |
|---|---|---|---|
| Dissociation Constant ($K_D$) | 2.4 x $10^{-7}$ (M) | 1.2 x $10^{-8}$ (M) | 5.6 x $10^{-9}$ (M) |
| On-rate ($k_a$) | 1.3 x $10^{5}$ (1/Ms) | 7.0 x $10^{4}$ (1/Ms) | 2.6 x $10^{4}$ (1/Ms) |
| Off-rate ($k_d$) | 3.2 x $10^{-2}$ (1/s) | 8.2 x $10^{-4}$ (1/s) | 1.5 x $10^{-4}$ (1/s) |

**Figure 6.4** Binding affinity of peptide and PLPs measured by bio-layer interferometry. Binding kinetics of (A) ABT898 peptide, (B) A PLP and (C) AR PLP were measured using CD36 protein. (D) Dissociation constants, on-rates and off-rates from BLI were summarized in the table.

### 6.2.5 Fatty Acid Uptake assay

Fatty acid (FA) uptake is an important cellular function and play important roles in the metabolic regulation. Especially, CD36 facilitates a major fraction of fatty acid uptake by key tissues.[209] One of the mechanism of TSP1 protein as an anti-angiogenesis factor is to prevent the nitric oxide signaling by inhibiting myristic acid uptake of CD36 transmembrane protein.[210]

As a mechanistic study, we performed the fatty acid uptake assay (Figure 6.5). In this experiment, we have prepared the fatty acid dye ($C_1$-BODIPY-$C_{12}$ fatty acid) to measure the intracellular fluorescence via flow cytometry. Low intracellular fluorescence signal indicates more inhibition of fatty acid uptake, while high intracellular fluorescence signal indicates less inhibition of fatty acid uptake. We have measured the mean fluorescence with different concentration of peptide/PLP. For both HT1080 and MCF7 cell lines, which overexpress the CD36 proteins, the AR PLP showed less mean fluorescence than the ABT898 peptide (Figure 6.5 B and C). This represents higher binding affinity of AR PLP than ABT898 peptide to the CD36 protein, which confirms previous BLI experiment results.

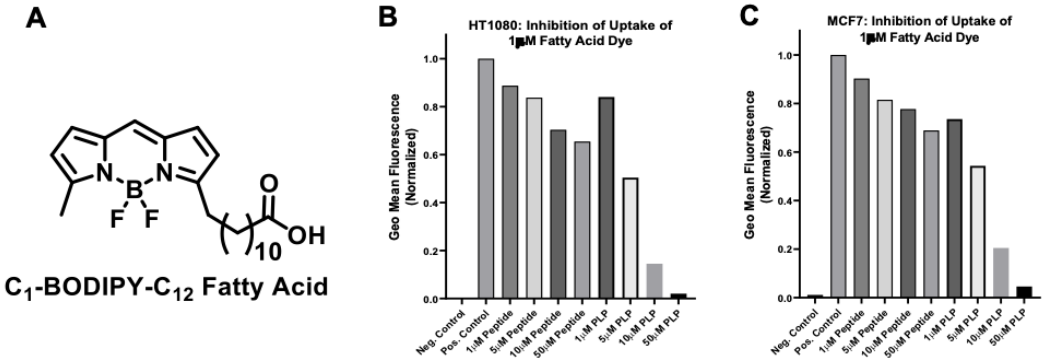


**Figure 6.5** Fatty acid uptake assay. (A) Chemical structure of $C_1$-BODIPY-$C_{12}$ fatty acid (B) Mean fluorescence measurement upon the co-treatment of C1-BODIPY-C12 fatty acid (1uM) and ABT898 peptide or AR PLP with different concentration.

## 6.3 Conclusion

In summary, we present the protein-like polymer (PLP) system for the treatment of neovascular age-related macular degeneration (nAMD). ABT898 peptide is an anti-angiogenic peptide that mimics the TSP-1 protein. Although, the daily intravitreal treatment of ABT898 peptide to the laser induced CNV mice model with TSP1-deficiency (TSP1 -/-) decrease significantly the CNV area, there are still remaining obstacles that limit the translational application as peptide drug, such as multiple injection and low cost-effectiveness mainly due to the degradation and renal clearance of the peptides.

AR PLP, in which the ABT898 peptides with two additional arginines are linked to the polymer backbone with amide bond, shows higher stability to the enzymes and higher binding affinity to the CD36 target protein than the original peptide sequence. Also, AR PLP inhibits the fatty acid uptake with higher extent than the peptide in the CD36 transmembrane protein overexpressed cell lines. In the ex vivo choroidal sprouting assays, AR PLP exhibit great anti-angiogenic efficacy compared to peptide and hydrolysable E and ER PLPs, demonstrating their extensive stability in biomimetic hydrogel. In addition, more anti-angiogenesis was detected in the case of AR PLP than the scramble version of AR PLP. This examines the specificity of ABT898 peptide sequence retained in the PLP platforms.

Overall, we demonstrate the PLP system as a potential peptide drug platform for the treatment of nAMD disease. We are planning to perform the *in vivo* study with laser-CNV mice model.

## 6.4 Experimental Details

### 6.4.1 Polymerization of Library of ABT898 PLPs.

ABT898 PLPs were achieved by ring-opening metathesis polymerization (ROMP) under nitrogen gas in a glove box. Norbornene conjugated peptide monomers (20 mg, 15.0 equiv.) were dissolved in degassed DMF. Next, the olefin metathesis initiator $(IMesH_2)(C_5H_5N)_2(Cl)_2Ru{=}CHPh$ stock solution (1.0 equiv., 20 mg/mL in DMF) was quickly added into the monomer solution. The solution was left to stir for 5-6 h until the full consumption of monomers. After the polymerization, the polymer solution was further purified via dialysis into deionized water. Finally, the polymer product was obtained by lyophilization.

### 6.4.2 Ex Vivo Choroidal Sprouting Assay.

Animals were checked for responses and euthanized by cervical dislocation after injection of Avertin. Eyes were enucleated and kept in ice-cold medium immediately before dissection. After removing the cornea and the lens from the anterior of the eye, the central or peripheral choroid-scleral complex was separated from the retina and cut into approximately 1 mm x1 mm fragments. Choroid/sclera fragments were isolated with and without RPE removal by peeling RPE away with forceps and placed in growth factor-reduced MatrigelTM (BD Biosciences, Cat. 354230) seeded in 24 well plates. 30 mL of matrigel was used to coat the bottom of 24 well plates without touching the edge of the well. The thickness of the matrigel was approximately 0.4 mm. After seeding the choroid, plates were incubated in a 37°C cell culture incubator without medium for 10 minutes in order for the MatrigelTM to solidify. 500 mL of medium was then added to each well

and incubated at 37°C with 5% $CO_2$ for 48 hr before any treatment. Medium was changed every 48 hr. Phase contrast photos of individual explants were taken daily using a ZEISS Axio Oberver.Z1 microscope. The areas of sprouting were quantified with computer software ImageJ.[211]

### 6.4.3 Enzyme Degradation Assay

For the enzyme degradation assay, we chose thermolysin as a model enzyme. The molar concentration of thermolysin was set to 0.1 μM. The concentration of side-chain peptides (GVi(allo)SQIRP) was set to 200 μM with respect to peptide. Also, the temperature was set to 37 °C to match the body temperature. In a typical experiment, ABT898 peptide and AR PLP were dissolved in 500ul of DPBS solution respectively. Next, 5 μL of thermolysin stock solution (10 uM) was added into the peptide/PLP solution which was subsequently stirred on the heating plate at 37 °C. In this case, the molar ratio of peptide substrate to thermolysin was 2000: 1. During the cleavage, aliquots were taken for HPLC analysis at predetermined time points. Each degradation experiment was repeated three times.

### 6.4.4 Bio-Layer Interferometry (BLItz) Binding Assay

Binding affinity were measured by using BLItz instrument. The amine reactive sensor (ARG2) was hydrated before the installation. After the sensor installation to the BLItz instrument, the sensors were modified with fresh activation solution (40mM of 1-1-Ethyl-3-[3-dimethylaminopropyl] carbodiimide hydrochloride (EDC) solution and 20mM of N-hydroxysulfosuccinimide(s-NHS) solution). CD36 proteins (50 ug/ml in sodium acetate buffer at pH6.5) were immobilized on the sensor and passivated by 1M ethanolamine. ABT898 peptide, A

PLP and AR PLP were dissolved in the Tris buffer (pH 8.4) with range of concentration (1uM, 500nM, 250nM, 100nM, 50nM). Using BLItz instrument, the dissociation constant ($K_D$), on-rate ($k_a$) and off-rate ($k_d$) of each analyte were measured.

### 6.4.5 Fatty Acid Uptake Assay

Cell are seeded in 1e5 in a 24 well plate, with a working volume of 500 microliters. Following 24 hours to allow for adherence, plating media was removed and replaced with 500 uL reduced serum media (Gibco™ Opti-MEM™) and left to sit over 24-hours to allow for basal conditions. For cells treated with peptide or PLP for 24 hours, the 500uL media contained the therapeutic at its respective concentration. Following 24 hours, without removing media, cells were treated with 500uL BODIPY-C12 fatty acid dye in 1% BSA (w/v) in DPBS, where the final concentration of dye is 1uM. Cells were then left to incubate with the 1uM BODPOY dye for 5 minutes. After 5 minutes of incubation, all contents of the wells were aspirated off, and cells were washed 3x with ice cold 1% BSA (w/v) DPBS (-) solution to stop uptake and scavenge residual fatty acid dye. After, cells were treated with 200 uL 0.25% tryspin solution for 5 minutes. After detachment, trypsinization was stopped by adding 500uL DMEM to each well, and the contents were transferred to Eppendorf tubes. The tubes were spun down at 0.2x 1000 gravity for 5 minutes, and the media and trypsin were aspirated off. The cell pellet was resuspended in 200 uL of ice-cold 10%FBS (v/v) DPBS (-) and transferred to a 96-well plate for FACS.

# Chapter 7. Protein-like Polymers for the Therapeutic Application: Huntington's Disease

## 7.1 Introduction

Huntington's disease (HD) is an autosomal dominant, fatal neurodegenerative disease affecting approximately 30,000 individuals in the United States with at least 150,000 other Americans with a 50% risk of developing the disease.[212] The disease affects anywhere from 4 to 13 individuals per 100,000 in Western populations.[213-215] Disease epidemiologists tracking the disease have noticed its prevalence increasing, and still no cure has been developed.[216] HD is characterized by motor dysfunction, involuntary movements, dystonia, cognitive decline, intellectual impairment and emotional disturbances.[212, 215-218] Symptoms are usually adult onset, beginning between 30-50 years of age with the course of the disease lasting 15-20 years.[212, 219] HD is terminal upon diagnosis, as the expansion of the CAG codon within the mutant huntingtin gene causes mitochondrial dysfunction.[212, 213, 215, 217-220] Mutant huntingtin protein (mtHtt) within the mitochondria binds to valosin containing protein (VCP) erroneously, marking the mitochondria for autophagy and resulting in neuronal cell death.[213-215, 220] Neuronal loss is particularly prominent in the striatum, where atrophy has significant impact on motor function and motor planning, causing chorea or involuntary movement.[212-215, 217, 219, 220] Although the HTT gene has been identified and a genetic test is available to identify those individuals who carry the mutation and will succumb to the disease, there is currently no therapy to slow or prevent disease progression, only symptomatic treatments with limited impact.[212, 217] Recent developments of therapeutics targeting the striatum via injection are invasive, have low efficacy, and are not

sustainable.[218] A clear and present barrier to treating HD remains to be solved, and this work proposes to overcome that obstacle. If the engineered peptides have the anticipated inhibitory effects *in vivo*, they will provide novel direction for therapeutic explorations and may ultimately guide the development of long-awaited neuroprotective therapeutics for HD.

Pathogenesis of HD initiates in neuronal mitochondria when mtHtt binds to VCP, resulting in mitochondrial autophagy as a mechanism of cell death.[213-215, 220] Recently, a peptide known as HV-3 has been shown *in vivo* to block VCP translocation to mtHtt in the mitochondria, rescuing neurons from mitochondrial destruction. While this peptide is effective in animal models, poor pharmacokinetics result in the need for continuous high dosing over long periods of time significantly limiting the practical utility of HV-3 in the clinic.[220] Of course, this kind of problem plagues peptides generally. That is, many peptides have been explored as easily synthesized biocompatible, target-specific therapeutic agents, but fail in translation.[221-224] A major factor is that their inherently low molecular weight means peptides are readily renally cleared. Coupled with this is that they further undergo rapid degradation by proteolytic enzymes *in vivo* (in cells, tissues, body fluids). Therefore, high injected doses are needed to achieve therapeutic concentrations.[223-225] We offer the development and optimization of a new, therapeutic version of HV-3 that blocks mutant Huntingtin (mtHtt) from binding VCP, thus ameliorating Huntington's Disease pathology.[220]

Protein-Like Polymers (PLPs), globular, peptide-based structures, assembled around a hydrophobic core (synthetic polymer), displaying active amino acids for recognition and function in a controlled, precise manner. We propose this as a new class of "polypeptide" where peptides form side chains of the main backbone of a polymer framework, in contrast to the classical,

biological, linear polypeptide configuration. Peptide monomers are polymerized into macromolecular chains of high density known as brush polymers that protect the peptide from degradation and prolong circulation without compromising bioactivity.[198, 199, 226] We envision that this PLP platform will provide a general, accessible route to the development of proteolytically-resistant peptides capable of performing the functions inherent to the peptide, such as inducing a therapeutic effect.

## 7.2 Results and Discussion

### 7.2.1 Synthesis of HV3 PLPs

We have designed various candidates for HD therapeutics featuring peptides with the HV-3 sequence and positive amino acids arginine or lysine to assist in cell penetration. Instead of the original sequence of the HV-3 peptide (HVLVMCAT), we substituted cysteine to serine (HVLVMSAT) due to the possibility of disulfide bond formation between the monomers. Four different monomers were polymerized using ring opening metathesis polymerization (ROMP) with a ruthenium initiator (Figure 7.1). Different numbers of positive amino acids (Figure 7.1, blue) were introduced to each monomer to investigate the cell penetrating effect, thus replacing cell penetrating peptide (TAT) of the original sequence for the HV3 peptide.

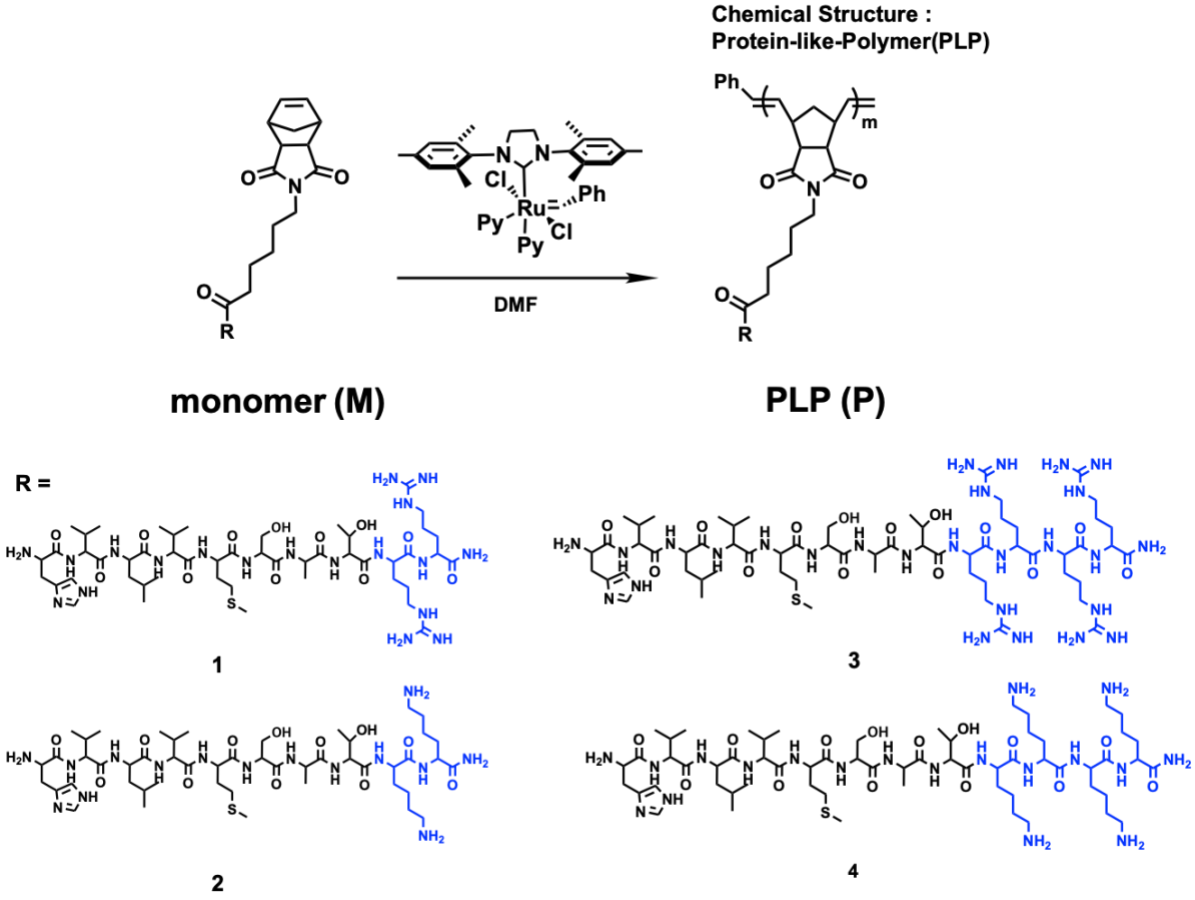


**Figure 7.1** Structure of Protein-Like Polymer (PLP). HV3 peptide analogs with different number of positive charged amino acids (blue) were polymerized into PLPs using ROMP polymerization technique.

### 7.2.2 Mortality Assessment of Mutant Striatal Cells

We conducted *in vitro* assays to examine the bioactivity of the PLPs. HD mouse striatal HdhQ111 (mutant) cells were used to profile the cell viability upon treatment of PLPs (Figure 7.2). The cell viability was over one hundred percent upon treatment of HV3 peptide and PLPs, which indicates that both HV3 peptide and PLPs recue the serum-starved mutant cells. We have reasoned that the HV3 peptide showed higher cell viability than PLPs due to the protective characteristics of the highly dense peptide monomers in the polymer sidechains. P3 was excluded from further tests as a candidate as it had the lowest success in increasing cell viability.

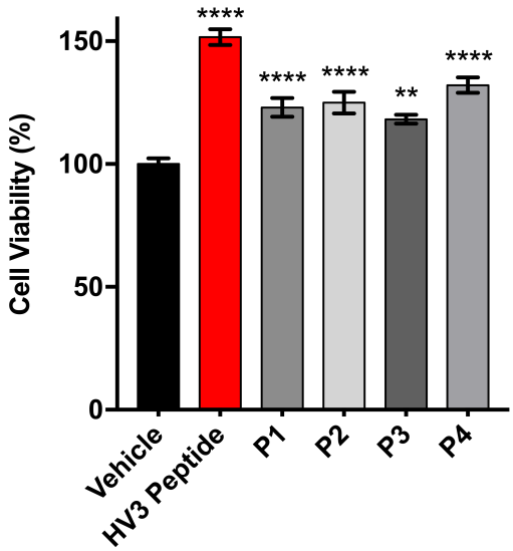


**Figure 7.2** Cell viability of different PLPs. HV3 peptide and PLPs were treated to the HD cells once a day for 3 days. Concentration was 3uM with respect to peptide.

### 7.2.3 Association of HV3 PLPs to the VCP Protein

To prove whether the PLPs engage the expected target (VCP) comparably to the original monomeric peptide, HV-3, we conducted protein binding assays. Immunoprecipitation analysis was used to confirm binding of PLP to VCP, blocking binding to mtHtt (Figure 7.3). This indicates the PLPs are viable therapeutic agents in that they successfully block the VCP binding to mtHtt that triggers neuronal mitophagy and ultimately cell death. HV3 peptide, P1 and P4 exhibit better prevention of VCP association to the mtHtt than the vehicle, while P2 exhibits similar extent of prevention as the vehicle. These results exclude the P2 for the mitochondrial fragmentation assessment.

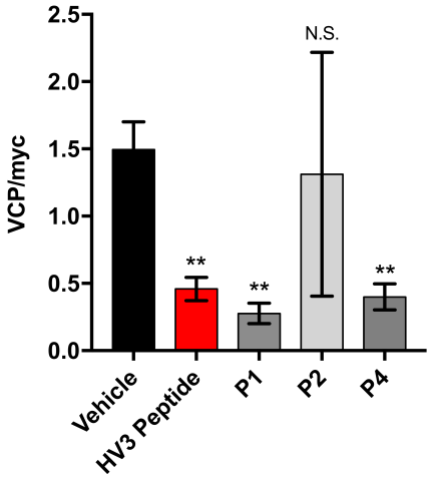


**Figure 7.3** Prevention of association of VCP to mtHtt. Association of VCP to mtHtt was quantified by immunoprecipitation (IP) followed by western blot upon treatment of HV3 peptide and PLPs. Each HV3 peptide and PLPs were treated with 3 uM of concentration.

### 7.2.4 Assessment of Mitochondrial Fragmentation

Mitochondrial fragmentation is the decisive hallmark of mtHtt striatal cells. Preventing the mitochondrial fragmentation is a pivotal process for the health of striatal cells. To demonstrate the ability of PLP to prevent the mitochondrial fragmentation, the mitochondrial morphology was assessed by confocal fluorescent imaging (Figure 7.4). Whilst fragmented mitochondria were observed with vehicle treatment, less fragmented mitochondria were identified upon treatment of HV3 peptide, P1 and P4, indicating they can rescue the mtHtt cells from cell death. Although both P1 and P4 exhibited the prevention of mitochondrial fragmentation, we chose P1 for the rest of the studies due to the higher core peptide drug sequence (HVLVMSAT) loading in the PLP platform.

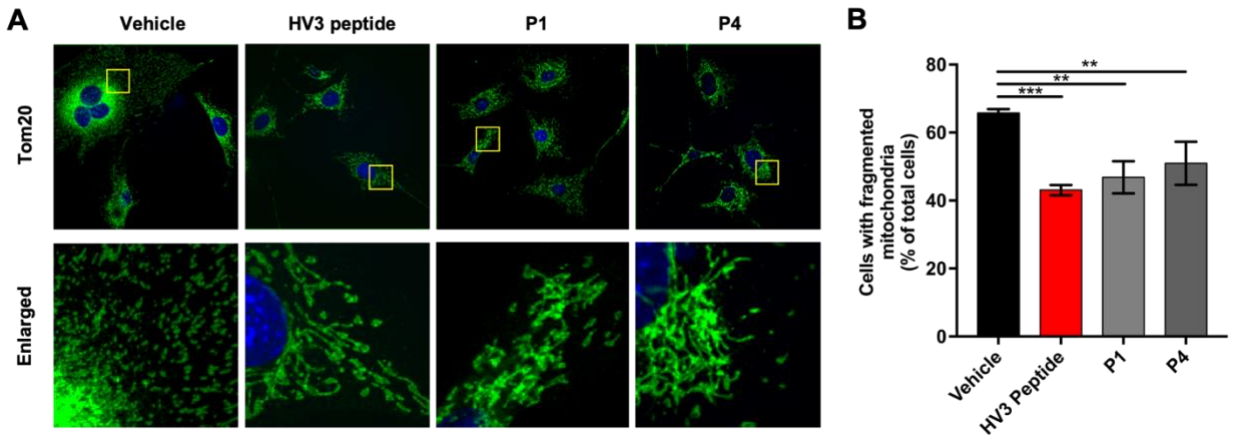


**Figure 7.4** Mitochondrial fragmentation assay. (A) Mitochondrial morphology was determined by staining cells with anti-Tom20 antibody (Green). (B) The percentage of cells with fragmented mitochondria relative to the total number of cells was quantitated. At least 100 cells per group were counted.

### 7.2.5 Assessment of Cellular Uptake

Poor membrane permeability is a major drawbacks of peptide drug. Many peptide drugs fail to be delivered to the intracellular targets. As our target of interest, VCP, associates to the mtHtt bound to the membranes of mitochondria, it's crucial to prove that P1 can be translocated into the cell. First, we evaluated the cellular uptake by confocal microscopy. Both HV3 peptide and P1 were labeled rhodamine dye. We could observe the distinct intracellular red signal upon the treatment of dye labeled treatment groups (Figure 7.5 A). Next, we quantified the materials by flow cytometry (Figure 7.5 B). P1 showed much better cellular uptake than HV3 peptide and rhodamine dye, demonstrating the exceptional transmembrane permeability of PLP platform.

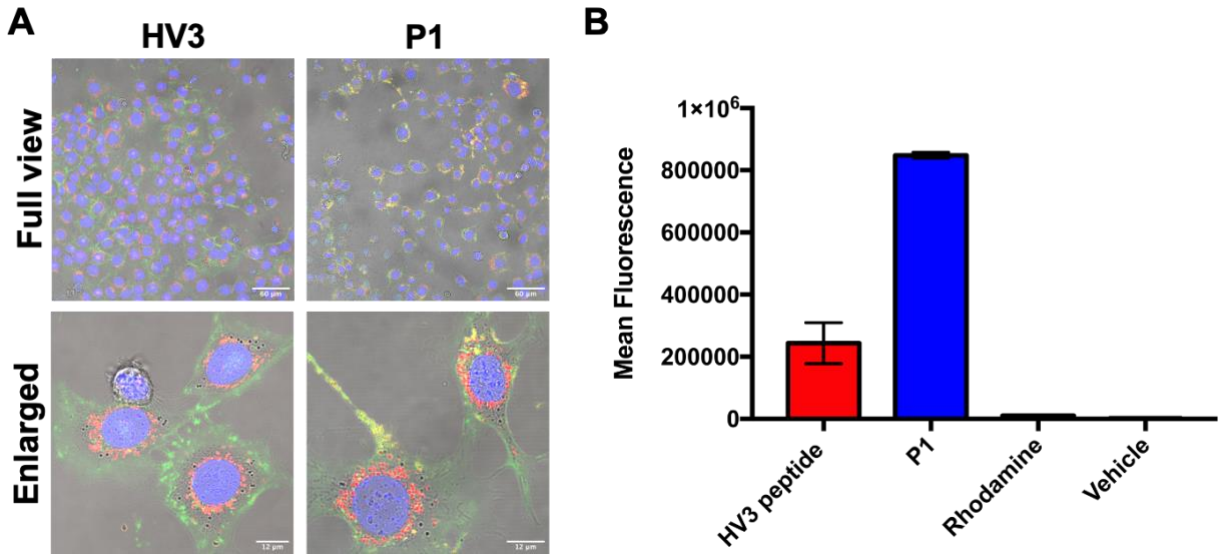


**Figure 7.5** Cellular Uptake Assays. (A) Live cell confocal microscopy in HD95 cells. HV3 peptide and P1 were treated to the HD cells at concentration of 3uM with respect to peptide. Green is cell membrane, red is treatment compound, and blue is nucleus. (B) Quantification of mean fluorescence output of flow cytometry cellular uptake in striatal HdhQ111 cells. Treatments: HV3 peptide, P1, rhodamine dye, and vehicle.

### 7.2.6 Assessment of Mitochondrial Localization

Since the mitochondria is the target of the system, we evaluated the mitochondrial localization of P1 in striatal HdhQ11 cells (Figure 7.6). To visualize the localization of the HV3 peptide and P1 to the mitochondria, we labelled the HV3 peptide and P1 with rhodamine dye (red) and mitochondria with Mito Tracker (green). Both HV3 peptide (positive control) and P1 exhibited yellow signal (overlap of red and green channels) upon the treatment while the treatment of rhodamine dye (negative control) didn't show the yellow signal (Figure 7.6). This demonstrates that the P1 can be localized to the target mitochondria.

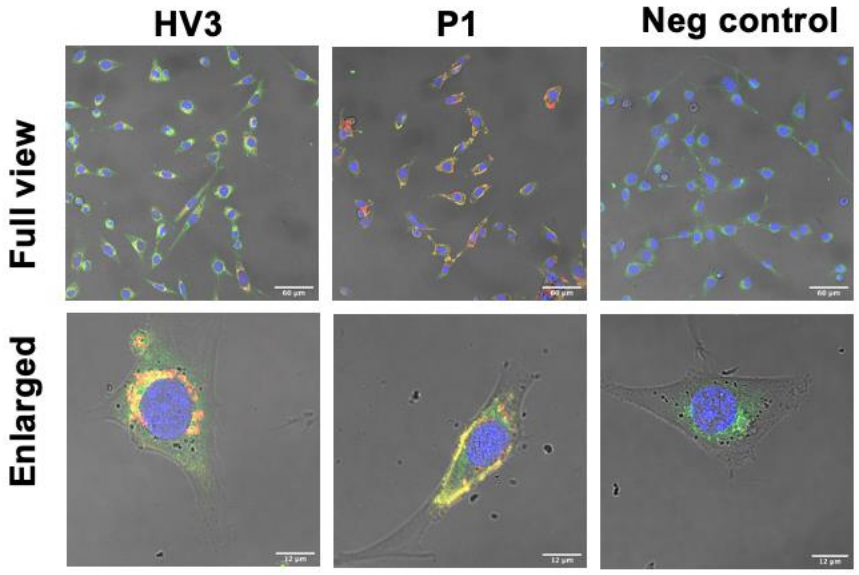


**Figure 7.6** Mitochondrial localization in striatal HdhQ111 cells. HV3 peptide, P1, and rhodamine were treated to the striatal HdhQ11 cells at concentration of 3uM with respect to peptide. Yellow signal shows overlap of green and red channels, signifying localization of compound in the mitochondria. Green is mitochondria, red is treatment compound, and blue is nucleus.

### 7.2.7 Binding Interaction of PLPs to VCP Protein

We proceeded to study the interaction of VCP receptor with HV3 peptide and P1. Aqueous solutions of HV3 peptide and P1 at various concentrations were assayed to study their binding with the VCP receptor (Figure 7.7). We recorded a dissociation constant in the 9.2 x $10^{-8}$ M range for P1 and 1.4 x $10^{-5}$ M for the HV3 peptide. These data indicate that the PLPs have stronger affinity for VCP protein than HV3 peptide, demonstrating the multivalent effect of PLP system.

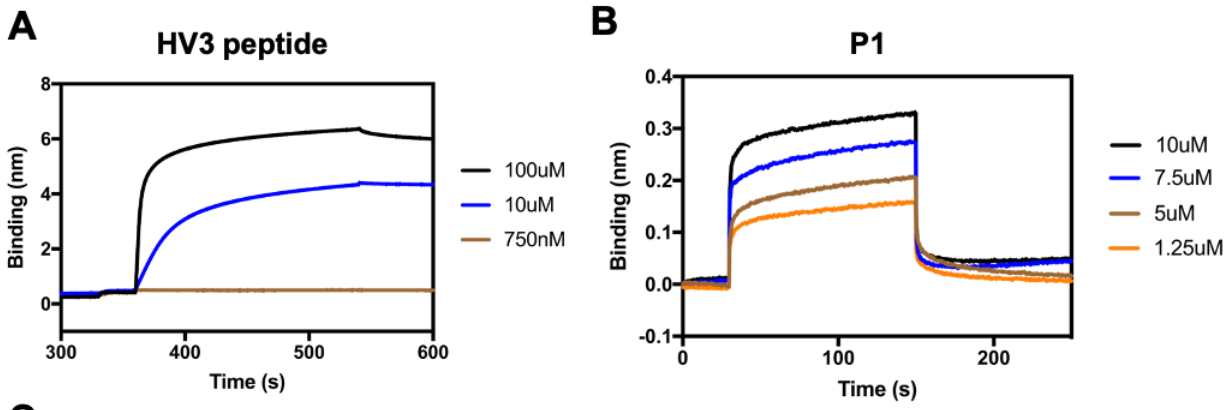


C

| | HV3 PLP | HV-3 peptide |
|---|---|---|
| **Dissociation Constant ($K_D$)** | 9.2 x $10^{-8}$ M | 1.4 x $10^{-5}$ M |
| **On-rate ($k_a$)** | 2.3 x $10^{3}$ 1/Ms | 1.6 x $10^{3}$ 1/Ms |
| **Off-rate ($k_d$)** | 2.5 x $10^{-5}$ 1/s | 2.3 x $10^{-2}$ 1/s |

**Figure 7.7** Binding affinity of peptide and PLPs measured by bio-layer interferometry. Binding kinetics of (A) HV3 peptide and (B) P1 were measured using VCP protein. (C) Dissociation constants, on-rates and off-rates from BLI were summarized in the table.

### 7.2.8 *In Vitro* Assessment of Blood Brain Barrier Translocation

In order to further understand and predict how the PLP will behave *in vivo* for a neurodegenerative target, we assessed its ability to permeate the blood brain barrier (Figure 7.8). Using human brain microvascular endothelial cells (HBEC-5i), we mimicked the same endothelial cells that form a protective layer around the brain's blood vessels. We treated cells with fluorescently dye labeled compounds, including P1, HV3 peptide, and controls. Percent translocation of materials across cell covered membrane was quantified, with both peptide and P1 showing translocation across the membrane, confirming the potential therapeutic use *in vivo*.

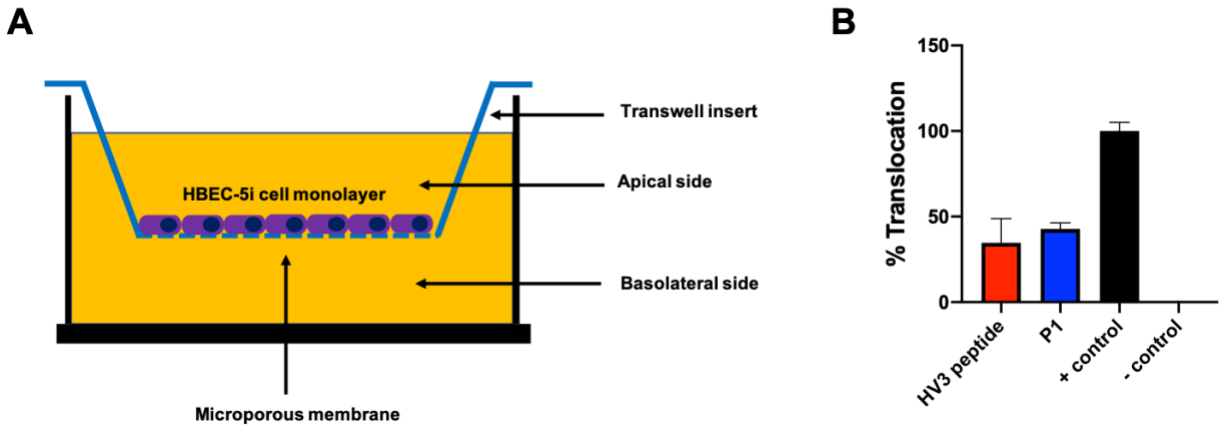


**Figure 7.8** *In vitro* blood brain barrier translocation assay**.** (A) Experimental design of blood brain barrier assay, where human HBEC-5i cells control translocation of materials across membrane. (B) % Translocation of compounds treated to HBEC-5i cells using formula (fluorescence outer well – fluorescence from cell media)/(fluorescence control – fluorescence media). + control : NaF, - control : vehicle.

### 7.2.9 Stability Assay

A key feature of the PLP platform centers on the proteolytic resistance the polymer backbone offers the peptide.[198, 227] Comprehensive enzyme degradation studies were conducted to ascertain the extent to which proteolysis is abated by the peptides being protected in the polymer form (Figure 3). In separate tests, pepsin and chymotrypsin were added to the PLPs across substrate concentration ranges. Analytical HPLC was used to evaluate fragment species existence and to determine percent cleavage as a function of time. Enzymes are chosen for their ability to fragment the peptides at only one cleavage site. Pepsin is one of the main stomach digestion enzymes. It cleaved HV3 peptide into two different fragments in 50 min (Figure 7.9 A). On the other hand, P1 was not cleaved into the fragment (SATRR) in the same period of time. This was confirmed by overlapping the HPLC peak with the synthesized fragment (Figure 7.9 B). Interestingly, the protection of P1 to the pepsin remained up to 450 min (Figure 7.9 C). Also, the stability of P1 was confirmed by incubating materials in the serum. While HV3 peptide degraded fast in either 10% FBS or 20% FBS condition, P1 didn't show any degradation in the same condition.

To verify that the PLPs retain their bioactivities after the treatment of enzymes or serum, cell viability was assessed (Figure 7.10). HV3 peptide and P1 were pretreated with trypsin, pronase and 10% FBS prior to incubation with HD cells. A dramatic comparison emerges in which cells treated with enzyme or serum digested HV3 peptide show decreased cell viability relative to those treated with undigested peptide. In contrast, P1 displayed similar cell viability upon the incubation after pretreatment with enzyme or serum.

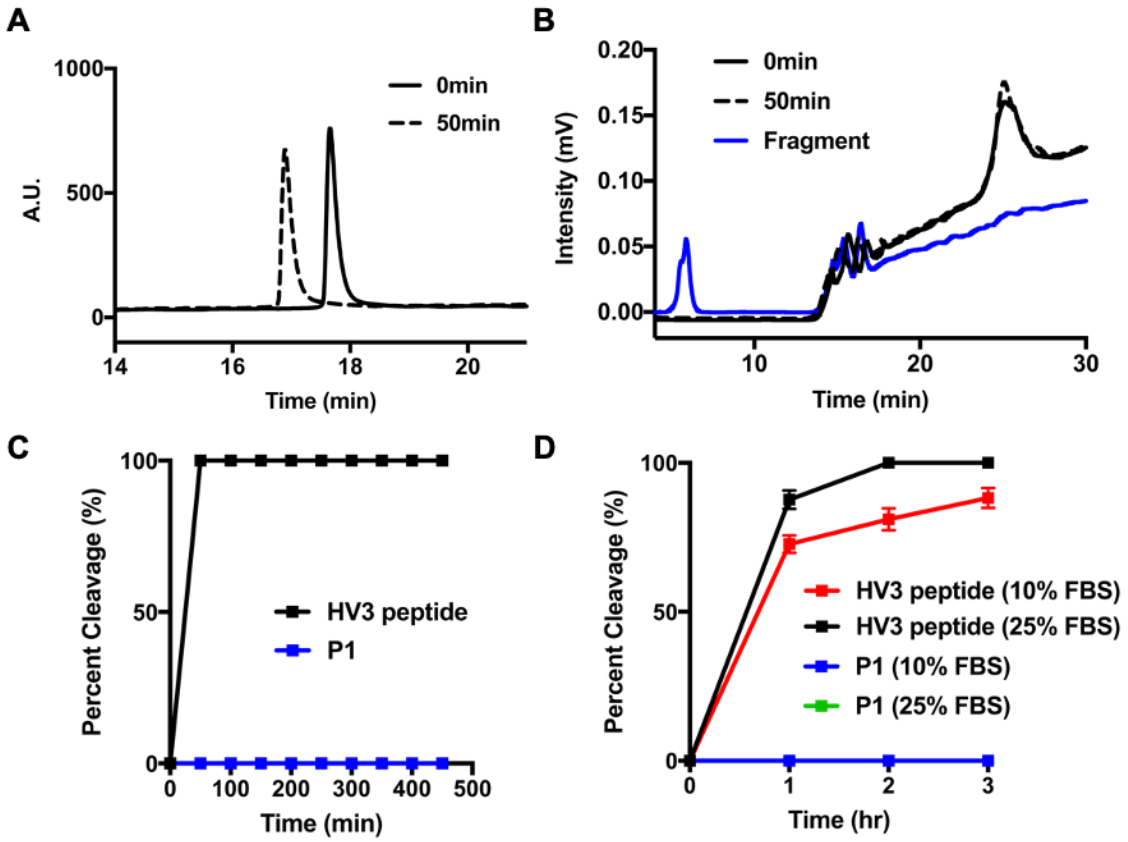


**Figure 7.9** Enzyme degradation and serum stability assays. The degradation kinetics of both HV3 peptide and P1 under the treatment of pepsin (pH2) was monitored by HPLC (A-C). (A) HV3 peptide (solid line) was degraded into cleaved product (dashed line). (B) P1 (solid line) was not degraded after the incubation in the pepsin enzyme for 50 minutes (dashed line). Expected fragment peak didn't overlap with dashed line, indicating that there is no degradation of P1. (C) Percent cleavage kinetics of HV3 peptide and P1 upon the treatment of pepsin in pH2 buffer. (D) Percent cleavage kinetics of HV3 peptide and P1 upon the treatment of 10% and 25% FBS.

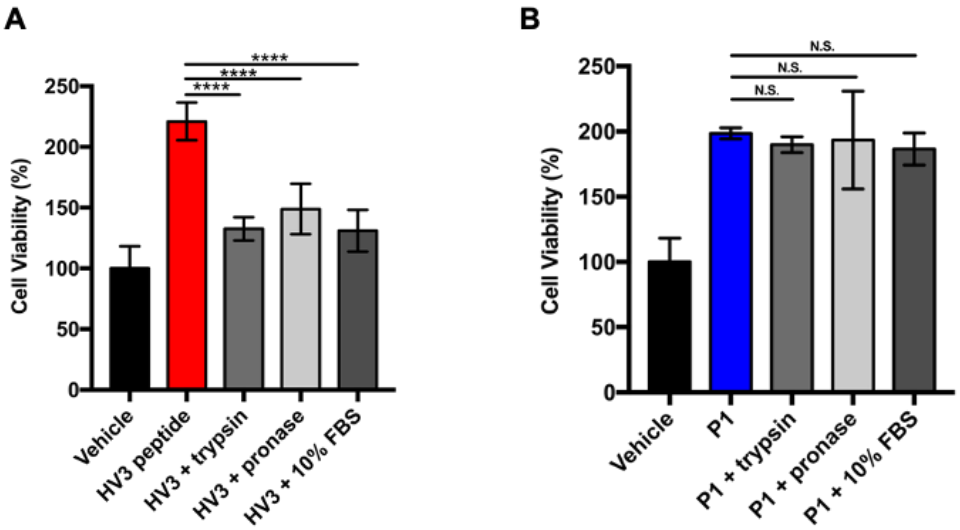


**Figure 7.10** Cell viability assay with enzymes or serum pretreated materials. (A) Cell viability after pretreating HV3 with different enzymes and 10% FBS. (B) Cell viability after pretreating P1 with different enzymes and 10% FBS. One-way ANOVA with multiple comparisons of the mean in each group with that of enzyme-untreated materials was used for analysis of cell viability. Statistical significance was defined as follows : N.S. ($p > 0.05$), * ($p \leq 0.05$), ** ($p \leq 0.01$), *** ($p \leq 0.001$), and **** ($p \leq 0.0001$).

### 7.2.10 Pharmacokinetic Profiles and Biodistribution

Polymers are polydisperse, and thus a method other than traditional LC-MS of plasma must be used to quantify its presence in blood and organs. With the gadolinium terminating agent tag we designed, we could facilely track the PLP in blood and tissue using ICPMS to analyze Gd levels in blood and tissue samples (Figure 7.11). The pharmacokinetics of the Gd tagged PLP follows the two-compartment model: there is an initial 20 minutes half-life with a distribution phase, followed by an extended 152 hour half-life of the elimination phase. The majority of the compound injected ends up in the liver and kidney, primary sites for drug metabolism. This PLP is detectable

3000x longer than the native peptide. Two-way ANOVA shows that there is no significance between the concentrations in the brain, striatum, and cortex for all time points, suggesting an average concentration of 0.6ug/g is the maintained concentration after 5 min.

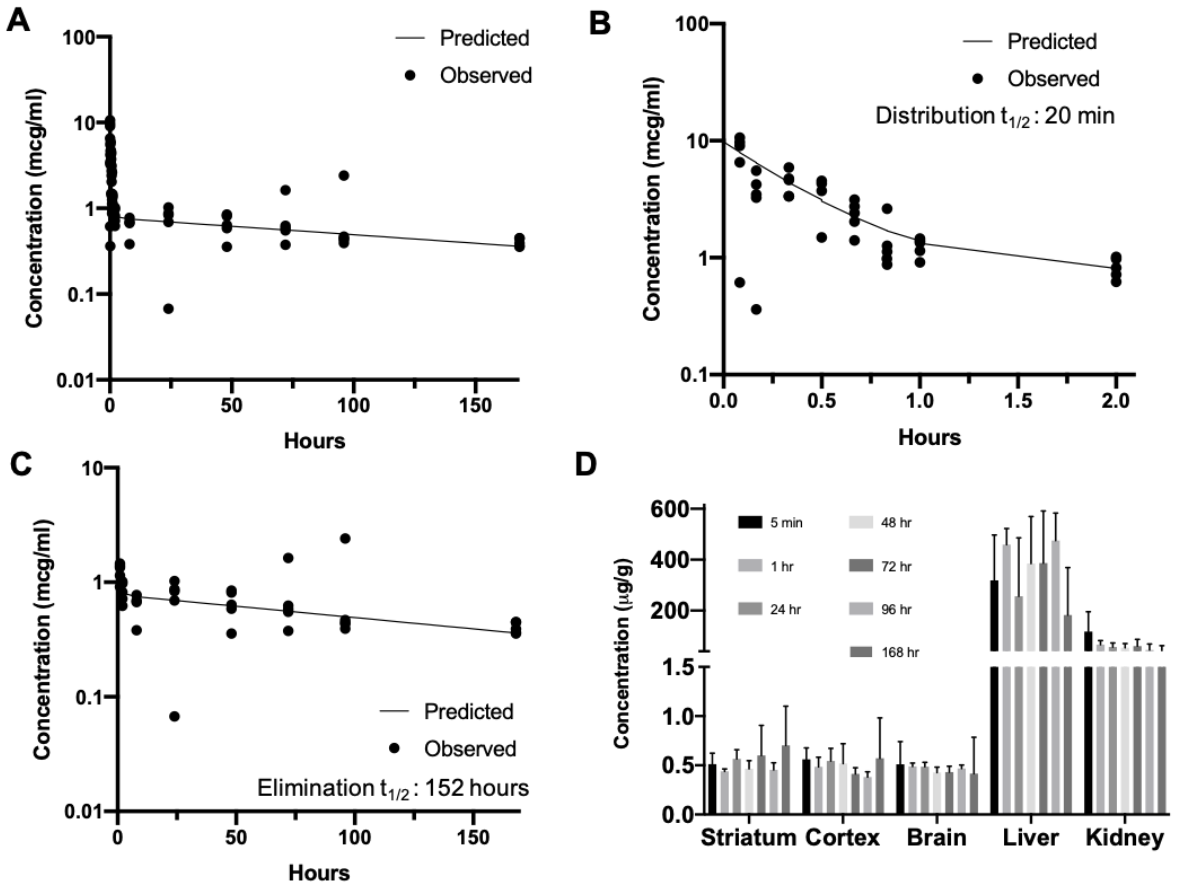


**Figure 7.11** Pharmacokinetics and biodistribution of Gd-P1. CD36 mice, WT for HD R6/2 mice, were dosed with 10mg/kg of Gd-P1 with respect to peptide (N=5 per group). Doses were administered IV via tail vein. Gd-P1 concentration was quantified by ICPMS and compared to calibration curve. (A) Full pharmacokinetic profile of Gd-P1 with predicted two-compartment model trend outlined overlayed with pharmacokinetic data. (B) Distribution phase of the pharmacokinetic profile of Gd-P1 from 5 minutes to 2 hours. Elimination half life is 20 minutes. (C) Elimination phase of the pharmacokinetic profile of Gd-P1 from 2 hours to 168 hours. Distribution half-life is 152 hours. (D) Biodistribution of Gd-P1. ug of P1 per g of organ across main timepoints, organized by organ.

### 7.2.11 Behavioral Analysis and Neuropathology

Huntington's phenotype R6/2 mice from Jackson laboratory have previously been used to assess efficacy of HV3 peptide. The accepted phenotype is a decrease in motor coordination (rotarod), general motility, and body weight as mice age from 5 to 13 weeks. R6/2 mice exhibited progressing deficits in motor deficits in the rotarod test, suggesting decreasing motor coordination and learning ability (Figure 7.12 A). Treatment with P1 significantly increased body weight of R6/2 mice compared to HV3 peptide and saline control (Figure 7.12 B). In a head-to-head comparison, R6/2 mice treated with HV3 peptide and saline displayed less survival rate than P1(Figure 7.12 C).

The levels of dopamine signaling protein, DARPP-32, enriched in medium spiny neurons are decreased in the striatum of HD patients and mouse models. Thus, DARPP-32 has been used as a marker to assess neuronal degeneration in HD mouse models. Western blot analysis of striatal extracts revealed a significant reduction of DARPP-32 protein levels in R6/2 mice. P1 treatment more significantly increased DARPP-32 levels when examined by immunoblotting (Figure 7.12 D). Significantly higher ratio of DARPP32 over actin for polymer vs both peptide and saline control indicate more DARPP32 is present in brains of PLP samples (Figure 7.12 E). This suggests fewer striatal neurons have died, thus signaling efficacy of PLP.

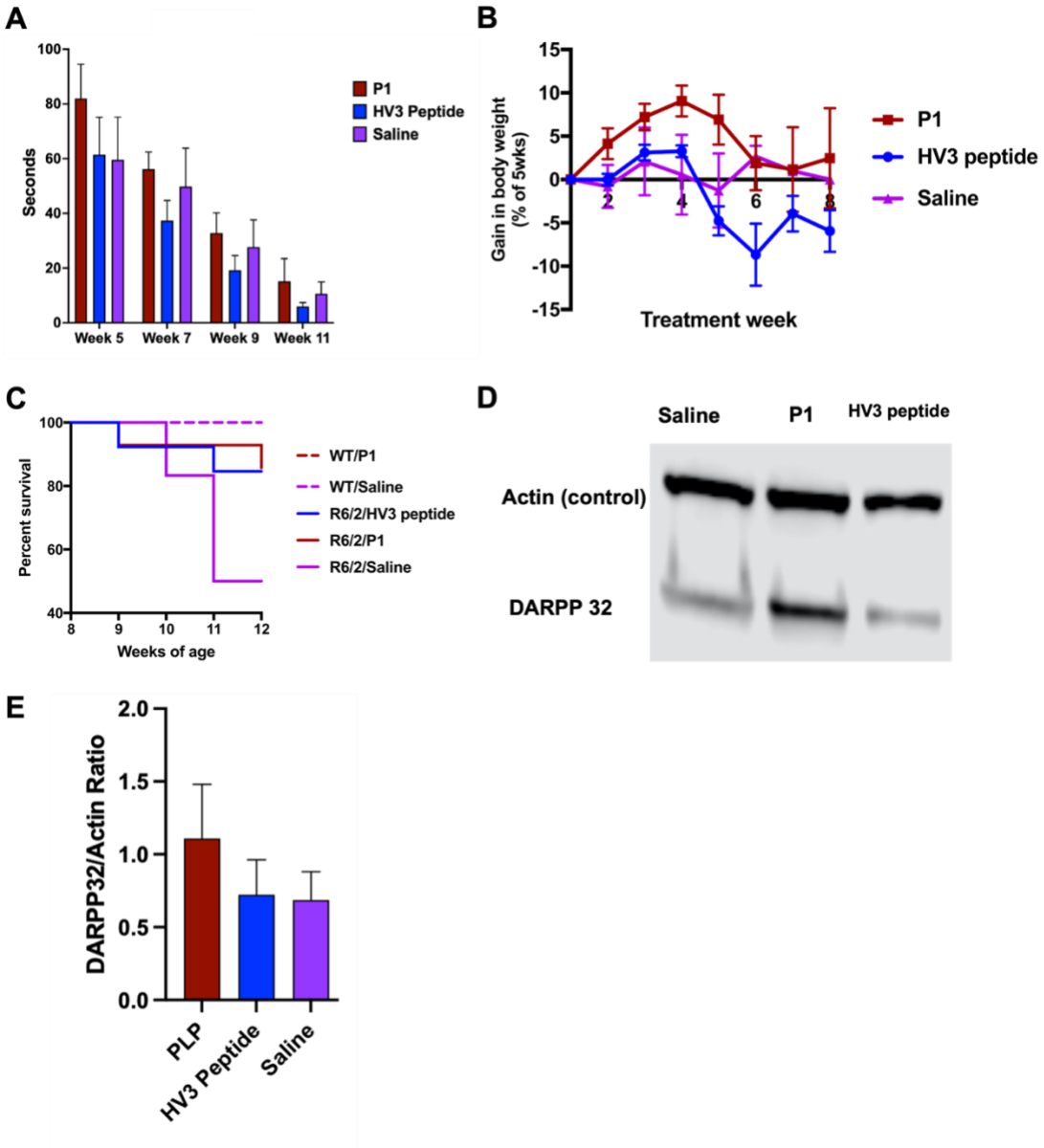


**Figure 7.12** Behavioral analysis and neuropathology. HD R6/2 mice and wild type litter mates were dosed with 3 mg/kg/day (with respect to peptide) of P1, HV3 peptide and saline from 6-13 weeks of age. Continuous dose administered via subcutaneous alzet osmotic pump. Groups: HD: P1, HV3 Peptide, Saline; WT: P1, Saline. (A) Rotarod performance of HD R6/2 was evaluated at the indicated age (n=7-14 mice per group). (B) Body weight was recorded from the age of 5–12 weeks (n=7-14 mice per group). (C) Survival rate was evaluated from the age 8-12 weeks (n=7-14 mice per group). (D) DARPP-32 protein levels were evaluated by WB of R6/2 mouse striatal lysates with representative image and (E) histogram of quantification of DARPP-32 levels. Actin was used as a loading control. n=4-8 mice/group.

## 7.3 Conclusion

In summary, we present the protein-like polymer (PLP) system for the treatment of Huntington's Disease. While the HV3 peptide prevents the neuronal death of mutant mouse striatal cells by impeding the VCP recruitment to the mtHTT, their clinical trial is limited due to their instability in the biological environment. To address this drawback, we employed the HV3 peptide into the densely packaged polymer (HV3 PLP). HV3 PLP showed good *in vitro* bioactivity with similar extent of HV3 peptide. Furthermore, we demonstrated an exceptional stability of HV3 PLP compared to the peptide by *in vitro* stability assays and pharmacokinetic profiling. Especially, HV3 PLP presented extended distribution half-life ($t_{1/2}$ = 20 min) and elimination half-life ($t_{1/2}$ = 152 hr) than HV3 peptide (undetectable), proposing its prospect as a novel peptide drug platform for the treatment of Huntington's disease.

## 7.4 Experimental Details

### 7.4.1 Polymerization of Library of HV3 PLPs.

HV3 PLPs were achieved by ring-opening metathesis polymerization (ROMP) under nitrogen gas in a glove box. Norbornene conjugated peptide monomers (20 mg, 15.0 equiv.) were dissolved in degassed DMF with 1M LiCl. Next, the olefin metathesis initiator $(IMesH_2)(C_5H_5N)_2(Cl)_2Ru{=}CHPh$ stock solution (1.0 equiv., 20 mg/mL in DMF) was quickly added into the monomer solution. The solution was left to stir for 12 h until the full consumption

of monomers. After the polymerization, the polymer solution was further purified via dialysis into deionized water. Finally, the polymer product was obtained by lyophilization.

### 7.4.2 Cell viability

Mouse striatal HdhQ111 cells were plated at a density of 5000 cells per well of a 96 well plate 18 hours prior to treatment. Cells were treated with HV3 peptide or PLPs at 3uM with respect to peptide once a day for 3days. The medium was replaced every day. Cell viability was assessed using the CellTilter-Blue assay. The medium was removed and 80 μL of new medium without phenol red was added followed by adding 20 μL of CellTilter-Blue reagent. The cells were incubated for 3 hours at 37 $^{o}$C. The fluorescence was measured at 560 nm excitation and 590 nm emission wavelength.

### 7.4.3 Confocal Laser Scanning Microscopy

Mouse striatal HdhQ111 cells were plated in a 4-chamber 35mm round glass-bottom dishes at a density of 50,000 per well. Cells were incubated for 24 hours in a 5% $CO_2$ atmosphere at 37 $^{o}$C. HV3 peptide, HV3 PLPs, rhodamine dye, and vehicle control in 10% FBS DMEM medium without phenol red were incubated with the cells for 24 hours, respectively. The cell nuclei (stained with Hoechst) was accomplished using a 405 nm laser with a 15% laser power. The cell membrane (stained with Wheat Germ Agglutinin, Alexa Fluor 488 Conjugate) was accomplished using a 488 nm laser with a 12% laser power. The mitochondria (stained with Mitotracker Green FM) was accomplished using 490nm laser with a 12% laser power. Cell imaging for Rhodamine fluorescence was accomplished using a 543 nm laser with an 8% laser power.

### 7.4.4 Cellular Uptake Measurement

For cellular uptake measurement, mouse striatal HdhQ111 cells were plated in 12-well plates at a density of 100,000 per well and incubated for 24 hours in a 5% $CO_2$ atmosphere at 37 $^{o}$C. HV3 peptide, HV3 PLPs, rhodamine dye and vehicle control in 10% FBS DMEM medium without phenol red were incubated with the cells for 24 hours respectively. After triple washing with DPBS, 100 µL of 0.25% Trypsin-EDTA was added to each well for 10 min at 37 $^{o}$C. The cell uptake study was analyzed through flow cytometry by using a BD FacsAria IIu 4-Laser flow cytometer (Becton Dickinson Inc., USA). Mean fluorescence intensity was prepared for presentation using FlowJo v10.

### 7.4.5 VCP Protein Association Assay

HEK293 cells were cultured and plated one day before treatment. Cells were pre-treated with HV3 peptide or PLPs at 3uM for 2h. Cells were then co-transfected with GFP-VCP and myc-Q73 FL plasmids. Cells were treated with a second dose of peptide or PLPs 6 hours after transfection, and a final third dose of peptide or PLPs treatment was administered 24 hours after transfection. Cell total lysate was harvested 48 hours after transfection, and immunoprecipitation analysis was performed to test the binding between mtHtt and VCP (IP myc—WB VCP). VCP binding to mtHtt was highly prevented by both P1 and P4, while poor performance in binding excludes P2 as a candidate.

### 7.4.6 Bio-Layer Interferometry (BLItz) Binding Assay

Binding affinity were measured by using BLItz instrument. The anti-HIS sensor (HIS2) was hydrated before the installation. After the sensor installation to the BLItz instrument, histidine tagged VCP proteins (50 ug/ml in sodium acetate buffer at pH 6.5) were immobilized on the sensor. HV3 peptide and P1 were dissolved in the Tris buffer (pH 8.4) with range of concentration. Using BLItz instrument, the dissociation constant ($K_D$), on-rate ($k_a$) and off-rate ($k_d$) of each analyte were measured.

### 7.4.7 Blood Brain Barrier Translocation Assay

For Blood Brain Barrier translocation assay, human brain microvascular endothelial cells (HBEC-5i cells) were seeded onto microporous membrane well inserts and cultured for 8 days to develop tight junctions. After 8 days, dye labeled compounds HV3 peptide, P1, positive control NaF and vehicle are treated in media on apical side of well. After 24 hours, media collected from basolateral side of wells, fluorescence read by plate reader, and % translocation calculated using formula (fluorescence outer well – fluorescence from cell media)/(fluorescence control – fluorescence media).

### 7.4.8 Enzyme Degradation Assay

For the enzyme degradation assay, we chose pepsin as a model enzyme. The molar concentration of pepsin was set to 0.1 μM. The concentration of side-chain peptides (HVLVMSATRR) was set to 200 μM with respect to peptide. Also, the temperature was set to

37 °C to match the body temperature. In a typical experiment, HV3 peptide and P1 were dissolved in 500ul of pH 2 buffer solution respectively. Next, 5 μL of pepsin stock solution (10 μM) was added into the peptide/PLP solution which was subsequently stirred on the heating plate at 37 °C. In this case, the molar ratio of peptide substrate to enzymes was 2000: 1. During the cleavage, aliquots were taken for HPLC analysis at predetermined time points. Each degradation experiment was repeated three times.

### 7.4.9 Pharmacokinetics

CD1 mice were purchased from Charles River laboratory and housed in Northwestern University's CCM core, handled by the DTC. All of the mice were maintained with a 12-h light/dark cycle (on 06:00 hours, off 18:00 hours) and acclimated for 1 week. Mice were dosed via IV with 10mg/kg with respect to peptide with a dose for a 30g mouse being 0.189mg of polymer in 100uL of saline.

At timepoints of 5 minutes, 10 min, 20 min, 30 min, 40 min, 50 min, 1 hour, 2 hr, 4 hr, 8 hr, 24hr, 48 hr, 72 hr, 96 hr, and 168 hr, mice were anesthetized and exsanguinated. (N=5). Whole blood was collected in pre-weighed falcon tubes. Livers, kidneys, striatum, cortex, and rest of the brain tissue were collected in pre-weighed tubes. Tubes were weighed again, to determine total mass of tissue collected in each tube.

To each tube of all samples except liver, 300 ul of conc nitric acid and 30% hydrogen peroxide were added. Liver samples had 500ul of conc nitric acid and 30% hydrogen peroxide added. All samples were digested in a 65°C water bath for 24 hours, until solutions were transparent. Tubes were diluted to 5ml total volume (10ml for liver) with Millipore water, and

weighed for a final time. After this point, any excess digested tissue that precipitated was removed by centrifugation and saving the supernatant. Each sample was run on high resolution ICPMS, which, after calibration with known Gd concentrations, resulted in exact Gd concentration in ppb of each sample. Ppb of Gd directly related to the calibration curve of known Gd PLP concentrations and was used to calculate the amount of PLP present in each sample.

Pharmacokinetics expert Dr. Michael Avram was consulted to perform statistical pharmacokinetics analysis and assist in plotting two-compartment pharmacokinetic half-life profile.

# References


1. Sun, H.; Choi, W.; Zang, N.; Battistella, C.; Thompson, M. P.; Cao, W.; Zhou, X.; Forman, C.; Gianneschi, N. C., Bioactive Peptide Brush Polymers via Photoinduced Reversible-Deactivation Radical Polymerization. *Angew Chem Int Ed Engl* **2019,** *58* (48), 17359-17364.

2. Liu, Q.; Wang, J.; Boyd, B. J., Peptide-based biosensors. *Talanta* **2015,** *136*, 114-27.

3. Carlini, A. S.; Choi, W.; McCallum, N. C.; Gianneschi, N. C., pH-Responsive Charge-Conversion Progelator Peptides. *Advanced Functional Materials* **2021,** *31* (13).

4. Metrano, A. J.; Miller, S. J., Peptide-Based Catalysts Reach the Outer Sphere through Remote Desymmetrization and Atroposelectivity. *Acc Chem Res* **2019,** *52* (1), 199-215.

5. Choi, W.; Battistella, C.; Gianneschi, N. C., High efficiency loading of micellar nanoparticles with a light switch for enzyme-induced rapid release of cargo. *Biomater Sci* **2021,** *9* (3), 653-657.

6. Chow, D.; Nunalee, M. L.; Lim, D. W.; Simnick, A. J.; Chilkoti, A., Peptide-based Biopolymers in Biomedicine and Biotechnology. *Mater Sci Eng R Rep* **2008,** *62* (4), 125-155.

7. Ledford, B.; Barron, C.; Van Dyke, M.; He, J. Q., Keratose hydrogel for tissue regeneration and drug delivery. *Semin Cell Dev Biol* **2021**.

8. Nematollahzadeh, A.; Lindemann, P.; Sun, W.; Stute, J.; Lutkemeyer, D.; Sellergren, B., Robust and selective nano cavities for protein separation: an interpenetrating polymer network modified hierarchically protein imprinted hydrogel. *J Chromatogr A* **2014,** *1345*, 154-63.

9. Hu, X. B.; Qin, Y.; Fan, W. T.; Liu, Y. L.; Huang, W. H., A Three-Dimensional Electrochemical Biosensor Integrated with Hydrogel Enables Real-Time Monitoring of Cells under Their In Vivo-like Microenvironment. *Anal Chem* **2021,** *93* (22), 7917-7924.

10. El-Sherbiny, I. M.; Yacoub, M. H., Hydrogel scaffolds for tissue engineering: Progress and challenges. *Glob Cardiol Sci Pract* **2013,** *2013* (3), 316-42.

11. Tavakoli, S.; Klar, A. S., Advanced Hydrogels as Wound Dressings. *Biomolecules* **2020,** *10* (8).

12. Coin, I.; Beyermann, M.; Bienert, M., Solid-phase peptide synthesis: from standard procedures to the synthesis of difficult sequences. *Nat Protoc* **2007,** *2* (12), 3247-56.

13. Henninot, A.; Collins, J. C.; Nuss, J. M., The Current State of Peptide Drug Discovery: Back to the Future? *J Med Chem* **2018,** *61* (4), 1382-1414.

14. Li, J.; Mooney, D. J., Designing hydrogels for controlled drug delivery. *Nat Rev Mater* **2016,** *1* (12).

15. Yang, C.; Suo, Z., Hydrogel ionotronics. *Nature Reviews Materials* **2018,** *3* (6), 125-142.

16. Slaughter, B. V.; Khurshid, S. S.; Fisher, O. Z.; Khademhosseini, A.; Peppas, N. A., Hydrogels in regenerative medicine. *Adv Mater* **2009,** *21* (32-33), 3307-29.

17. Edwards-Gayle, C. J. C.; Hamley, I. W., Self-assembly of bioactive peptides, peptide conjugates, and peptide mimetic materials. *Org Biomol Chem* **2017,** *15* (28), 5867-5876.

18. Park, J.; Choi, Y.; Chang, H.; Um, W.; Ryu, J. H.; Kwon, I. C., Alliance with EPR Effect: Combined Strategies to Improve the EPR Effect in the Tumor Microenvironment. *Theranostics* **2019,** *9* (26), 8073-8090.

19. Tang, Q.; Yu, B.; Gao, L.; Cong, H.; Song, N.; Lu, C., Stimuli Responsive Nanoparticles for Controlled Anti-cancer Drug Release. *Curr Med Chem* **2018,** *25* (16), 1837-1866.

20. Blum, A. P.; Kammeyer, J. K.; Rush, A. M.; Callmann, C. E.; Hahn, M. E.; Gianneschi, N. C., Stimuli-responsive nanomaterials for biomedical applications. *J Am Chem Soc* **2015,** *137* (6), 2140-54.

21. Hu, Q.; Katti, P. S.; Gu, Z., Enzyme-responsive nanomaterials for controlled drug delivery. *Nanoscale* **2014,** *6* (21), 12273-86.

22. Kamerlin, S. C.; Warshel, A., An Analysis of All the Relevant Facts and Arguments Indicates that Enzyme Catalysis Does Not Involve Large Contributions from Nuclear Tunneling. *J Phys Org Chem* **2010,** *23* (7), 677-684.

23. Gobin, E.; Bagwell, K.; Wagner, J.; Mysona, D.; Sandirasegarane, S.; Smith, N.; Bai, S.; Sharma, A.; Schleifer, R.; She, J. X., A pan-cancer perspective of matrix metalloproteases (MMP) gene expression profile and their diagnostic/prognostic potential. *BMC Cancer* **2019,** *19* (1), 581.

24. Meschiari, C. A.; Jung, M.; Iyer, R. P.; Yabluchanskiy, A.; Toba, H.; Garrett, M. R.; Lindsey, M. L., Macrophage overexpression of matrix metalloproteinase-9 in aged mice improves diastolic physiology and cardiac wound healing after myocardial infarction. *Am J Physiol Heart Circ Physiol* **2018,** *314* (2), H224-H235.

25. Wei, X. L.; Zhan, C. Y.; Shen, Q.; Fu, W.; Xie, C.; Gao, J.; Peng, C. M.; Zheng, P.; Lu, W. Y., A D-Peptide Ligand of Nicotine Acetylcholine Receptors for Brain-Targeted Drug Delivery. *Angew Chem Int Edit* **2015,** *54* (10), 3023-3027.

26. Kapitza, C.; Nosek, L.; Jensen, L.; Hartvig, H.; Jensen, C. B.; Flint, A., Semaglutide, a Once-Weekly Human GLP-1 Analog, Does Not Reduce the Bioavailability of Oral Contraceptives. *Diabetes* **2014,** *63*, A605-A605.

27. Zorzi, A.; Deyle, K.; Heinis, C., Cyclic peptide therapeutics: past, present and future. *Curr Opin Chem Biol* **2017,** *38*, 24-29.

28. Speltz, T. E.; Mayne, C. G.; Fanning, S. W.; Siddiqui, Z.; Tajkhorshid, E.; Greene, G. L.; Moore, T. W., A "cross-stitched" peptide with improved helicity and proteolytic stability. *Org Biomol Chem* **2018,** *16* (20), 3702-3706.

29. Bird, G. H.; Madani, N.; Perry, A. F.; Princiotto, A. M.; Supko, J. G.; He, X. Y.; Gavathiotis, E.; Sodroski, J. G.; Walensky, L. D., Hydrocarbon double-stapling remedies the proteolytic instability of a lengthy peptide therapeutic. *P Natl Acad Sci USA* **2010,** *107* (32), 14093-14098.

30. Pelegri-O'Day, E. M.; Lin, E. W.; Maynard, H. D., Therapeutic Protein-Polymer Conjugates: Advancing Beyond PEGylation. *J Am Chem Soc* **2014,** *136* (41), 14323-14332.

31. Tucker, B. S.; Coughlin, M. L.; Figg, C. A.; Sumerlin, B. S., Grafting-From Proteins Using Metal-Free PET-RAFT Polymerizations under Mild Visible-Light Irradiation. *Acs Macro Lett* **2017,** *6* (4), 452-457.

32. Fan, J.; Borguet, Y. P.; Su, L.; Nguyen, T. P.; Wang, H.; He, X.; Zou, J.; Wooley, K. L., Two-Dimensional Controlled Syntheses of Polypeptide Molecular Brushes via N-Carboxyanhydride Ring-Opening Polymerization and Ring-Opening Metathesis Polymerization. *Acs Macro Lett* **2017,** *6* (9), 1031-1035.

33. Baumgartner, R.; Fu, H. L.; Song, Z. Y.; Lin, Y.; Cheng, J. J., Cooperative polymerization of alpha-helices induced by macromolecular architecture. *Abstr Pap Am Chem S* **2017,** *253*.

34. Choi, W.; Sun, H.; Battistella, C.; Berger, O.; Vratsanos, M. A.; Wang, M. M.; Gianneschi, N. C., Biomolecular Densely Grafted Brush Polymers: Oligonucleotides, Oligosaccharides and Oligopeptides. *Angew Chem Int Ed Engl* **2020,** *59* (45), 19762-19772.

35. Line, B. R.; Mitra, A.; Nan, A.; Ghandehari, H., Targeting tumor angiogenesis: comparison of peptide and polymer-peptide conjugates. *J Nucl Med* **2005,** *46* (9), 1552-60.

36. Danial, M.; Root, M. J.; Klok, H. A., Polyvalent Side Chain Peptide-Synthetic Polymer Conjugates as HIV-1 Entry Inhibitors. *Biomacromolecules* **2012,** *13* (5), 1438-1447.

37. Sahariah, P.; Sorensen, K. K.; Hjalmarsdottir, M. A.; Sigurjonsson, O. E.; Jensen, K. J.; Masson, M.; Thygesen, M. B., Antimicrobial peptide shows enhanced activity and reduced toxicity upon grafting to chitosan polymers. *Chem Commun* **2015,** *51* (58), 11611-11614.

38. Song, Y.; Moore, E. G.; Guo, Y. S.; Moore, J. S., Polymer-Peptide Conjugates Disassemble Amyloid beta Fibrils in a Molecular-Weight Dependent Manner. *J Am Chem Soc* **2017,** *139* (12), 4298-4301.

39. Shi, J.; Schellinger, J. G.; Pun, S. H., Engineering biodegradable and multifunctional peptide-based polymers for gene delivery. *J Biol Eng* **2013,** *7* (1).

40. Deng, C.; Tian, H.; Zhang, P.; Sun, J.; Chen, X.; Jing, X., Synthesis and characterization of RGD peptide grafted poly(ethylene glycol)-b-poly(L-lactide)-b-poly(L-glutamic acid) triblock copolymer. *Biomacromolecules* **2006,** *7* (2), 590-6.

41. Palacián, E.; González, P. J.; Piñeiro, M.; Hernández, F., Dicarboxylic acid anhydrides as dissociating agents of protein-containing structures. *Mol. Cell. Biochem.* **1990,** *97* (2), 101-111.

42. Goto, Y.; Takahashi, N.; Fink, A. L., Mechanism of acid-induced folding of proteins. *Biochemistry* **1990,** *29* (14), 3480-3488.

43. Butler, P. J. G.; Harris, J. I.; Hartley, B. S.; Leberman, R., The use of maleic anhydride for the reversible blocking of amino groups on polypeptide chains. *Biochem. J.* **1969,** *112* (5), 679-689.

44. Liu, X.; Zhang, J.; Lynn, D. M., Polyelectrolyte multilayers fabricated from 'charge-shifting' anionic polymers: a new approach to controlled film disruption and the release of cationic agents from surfaces. *Soft Matter* **2008,** *4* (8), 1688-1695.

45. Lee, E. S.; Na, K.; Bae, Y. H., Super pH-Sensitive Multifunctional Polymeric Micelle. *Nano Lett.* **2005,** *5* (2), 325-329.

46. Lee, Y.; Fukushima, S.; Bae, Y.; Hiki, S.; Ishii, T.; Kataoka, K., A Protein Nanocarrier from Charge-Conversion Polymer in Response to Endosomal pH. *Journal of the American Chemical Society* **2007,** *129* (17), 5362-5363.

47. Takemoto, H.; Miyata, K.; Hattori, S.; Ishii, T.; Suma, T.; Uchida, S.; Nishiyama, N.; Kataoka, K., Acidic pH-Responsive siRNA Conjugate for Reversible Carrier Stability and Accelerated Endosomal Escape with Reduced IFNα-Associated Immune Response. *Angew. Chem. Int. Ed.* **2013,** *52* (24), 6218-6221.

48. Deng, H.; Liu, J.; Zhao, X.; Zhang, Y.; Liu, J.; Xu, S.; Deng, L.; Dong, A.; Zhang, J., PEG-b-PCL Copolymer Micelles with the Ability of pH-Controlled Negative-to-Positive Charge Reversal for Intracellular Delivery of Doxorubicin. *Biomacromolecules* **2014,** *15* (11), 4281-4292.

49. Luo, G.-F.; Chen, W.-H.; Liu, Y.; Lei, Q.; Zhuo, R.-X.; Zhang, X.-Z., Multifunctional Enveloped Mesoporous Silica Nanoparticles for Subcellular Co-delivery of Drug and Therapeutic Peptide. *Sci. Rep.* **2014,** *4*, 6064.

50. Huo, Q.; Zhu, J.; Niu, Y.; Shi, H.; Gong, Y.; Li, Y.; Song, H.; Liu, Y., pH-triggered surface charge-switchable polymer micelles for the co-delivery of paclitaxel/disulfiram and overcoming multidrug resistance in cancer. *International Journal of Nanomedicine* **2017,** *12*, 8631-8647.

51. Zhou, Q.; Hou, Y.; Zhang, L.; Wang, J.; Qiao, Y.; Guo, S.; Fan, L.; Yang, T.; Zhu, L.; Wu, H., Dual-pH Sensitive Charge-reversal Nanocomplex for Tumor-targeted Drug Delivery with Enhanced Anticancer Activity. *Theranostics* **2017,** *7* (7), 1806-1819.

52. Su, S.; Du, F.-S.; Li, Z.-C., Synthesis and pH-dependent hydrolysis profiles of mono- and dialkyl substituted maleamic acids. *Organic & Biomolecular Chemistry* **2017,** *15* (39), 8384-8392.

53. Kang, S.; Kim, Y.; Song, Y.; Choi, J. U.; Park, E.; Choi, W.; Park, J.; Lee, Y., Comparison of pH-sensitive degradability of maleic acid amide derivatives. *Bioorg. Med. Chem. Lett.* **2014,** *24* (10), 2364-2367.

54. Rizwan, M.; Yahya, R.; Hassan, A.; Yar, M.; Azzahari, A.; Selvanathan, V.; Sonsudin, F.; Abouloula, C., pH Sensitive Hydrogels in Drug Delivery: Brief History, Properties, Swelling, and Release Mechanism, Material Selection and Applications. *Polymers* **2017,** *9* (4), 137.

55. Chassenieux, C.; Tsitsilianis, C., Recent trends in pH/thermo-responsive self-assembling hydrogels: from polyions to peptide-based polymeric gelators. *Soft Matter* **2016,** *12* (5), 1344-1359.

56. Wang, L.; Shi, X.; Zhang, J.; Zhu, Y.; Wang, J., Self-assembled pH-responsive supramolecular hydrogel for hydrophobic drug delivery. *RSC Advances* **2018,** *8* (55), 31581-31587.

57. Kellum, J. A.; Song, M.; Li, J., Science review: Extracellular acidosis and the immune response: clinical and physiologic implications. *Critical Care* **2004,** *8* (5), 331-336.

58. Inserte, J.; Barba, I.; Hernando, V.; Garcia-Dorado, D., Delayed recovery of intracellular acidosis during reperfusion prevents calpain activation and determines protection in postconditioned myocardium. *Cardiovascular Research* **2009,** *81* (1), 116-122.

59. Kitakaze, M.; Takashima, S.; Funaya, H.; Minamino, T.; Node, K.; Shinozaki, Y.; Mori, H.; Hori, M., Temporary acidosis during reperfusion limits myocardial infarct size in dogs. *American Journal of Physiology-Heart and Circulatory Physiology* **1997,** *272* (5), H2071-H2078.

60. Goldie, I.; Nachemson, A., Synovial pH in Rheumatoid Knee-Joints I. The Effect of Synovectomy. *Acta Orthop. Scand.* **1969,** *40* (5), 634-641.

61. Treuhaft, P. S.; McCarty, D. J., Synovial fluid pH, lactate, oxygen and carbon dioxide partial pressure in various joint diseases. *Arthritis Rheum.* **1971,** *14* (4), 475-484.

62. Stevens, C. R.; Williams, R. B.; Farrell, A. J.; Blake, D. R., Hypoxia and inflammatory synovitis: observations and speculation. *Ann. Rheum. Dis.* **1991,** *50* (2), 124-132.

63. Green, J.; Maor, G., Effect of metabolic acidosis on the growth hormone/IGF-I endocrine axis in skeletal growth centers. *Kidney Int.* **2000,** *57* (6), 2258-2267.

64. Dissemond, J.; Witthoff, M.; Brauns, T. C.; Haberer, D.; Goos, M., pH-Wert des Milieus chronischer Wunden. *Der Hautarzt* **2003,** *54* (10), 959-965.

65. Rajamäki, K.; Nordström, T.; Nurmi, K.; Åkerman, K. E. O.; Kovanen, P. T.; Öörni, K.; Eklund, K. K., Extracellular Acidosis Is a Novel Danger Signal Alerting Innate Immunity via the NLRP3 Inflammasome. *The Journal of Biological Chemistry* **2013,** *288* (19), 13410-13419.

66. Seif-Naraghi, S. B.; Singelyn, J. M.; Salvatore, M. A.; Osborn, K. G.; Wang, J. J.; Sampat, U.; Kwan, O. L.; Strachan, G. M.; Wong, J.; Schup-Magoffin, P. J.; Braden, R. L.; Bartels, K.; DeQuach, J. A.; Preul, M.; Kinsey, A. M.; DeMaria, A. N.; Dib, N.; Christman, K. L., Safety and efficacy of an injectable extracellular matrix hydrogel for treating myocardial infarction. *Sci. Transl. Med.* **2013,** *5* (173), 10.1126/scitranslmed.3005503.

67. Peña, B.; Laughter, M.; Jett, S.; Rowland, T. J.; Taylor, M. R. G.; Mestroni, L.; Park, D., Injectable Hydrogels for Cardiac Tissue Engineering. *Macromol. Biosci.* **2018,** *18* (6), 1800079.

68. Spiller, K. L.; Maher, S. A.; Lowman, A. M., Hydrogels for the Repair of Articular Cartilage Defects. *Tissue Engineering. Part B, Reviews* **2011,** *17* (4), 281-299.

69. Rey-Rico, A.; Madry, H.; Cucchiarini, M., Hydrogel-Based Controlled Delivery Systems for Articular Cartilage Repair. *BioMed Research International* **2016,** *2016*, 12.

70. Li, Z.; Yuan, B.; Dong, X.; Duan, L.; Tian, H.; He, C.; Chen, X., Injectable polysaccharide hybrid hydrogels as scaffolds for burn wound healing. *RSC Advances* **2015,** *5* (114), 94248-94256.

71. Griffin, D. R.; Weaver, W. M.; Scumpia, P.; Di Carlo, D.; Segura, T., Accelerated wound healing by injectable microporous gel scaffolds assembled from annealed building blocks. *Nature materials* **2015,** *14* (7), 737-744.

72. Li, Z.; Zhou, F.; Li, Z.; Lin, S.; Chen, L.; Liu, L.; Chen, Y., Hydrogel Cross-Linked with Dynamic Covalent Bonding and Micellization for Promoting Burn Wound Healing. *ACS Applied Materials & Interfaces* **2018,** *10* (30), 25194-25202.

73. Bell, C. J.; Carrick, L. M.; Katta, J.; Jin, Z.; Ingham, E.; Aggeli, A.; Boden, N.; Waigh, T. A.; Fisher, J., Self-assembling peptides as injectable lubricants for osteoarthritis. *Journal of Biomedical Materials Research Part A* **2006,** *78A* (2), 236-246.

74. Joshi, N.; Yan, J.; Levy, S.; Bhagchandani, S.; Slaughter, K. V.; Sherman, N. E.; Amirault, J.; Wang, Y.; Riegel, L.; He, X.; Rui, T. S.; Valic, M.; Vemula, P. K.; Miranda, O. R.; Levy, O.; Gravallese, E. M.; Aliprantis, A. O.; Ermann, J.; Karp, J. M., Towards an arthritis flare-responsive drug delivery system. *Nature Communications* **2018,** *9* (1), 1275.

75. El-Sherbiny, I. M.; Yacoub, M. H., Hydrogel scaffolds for tissue engineering: Progress and challenges. *Global Cardiology Science & Practice* **2013,** *2013* (3), 316-342.

76. Zhu, J.; Marchant, R. E., Design properties of hydrogel tissue-engineering scaffolds. *Expert review of medical devices* **2011,** *8* (5), 607-626.

77. Chuang, E.-Y.; Chiang, C.-W.; Wong, P.-C.; Chen, C.-H., Hydrogels for the Application of Articular Cartilage Tissue Engineering: A Review of Hydrogels. *Advances in Materials Science and Engineering* **2018,** *2018*, 13.

78. Maulvi, F. A.; Lakdawala, D. H.; Shaikh, A. A.; Desai, A. R.; Choksi, H. H.; Vaidya, R. J.; Ranch, K. M.; Koli, A. R.; Vyas, B. A.; Shah, D. O., In vitro and in vivo evaluation of novel implantation technology in hydrogel contact lenses for controlled drug delivery. *J Control Release* **2016,** *226*, 47-56.

79. Burdick, J. A.; Murphy, W. L., Moving from static to dynamic complexity in hydrogel design. *Nature Communications* **2012,** *3*, 1269.

80. Portnov, T.; Shulimzon Tiberiu, R.; Zilberman, M., Injectable hydrogel-based scaffolds for tissue engineering applications. In *Rev. Chem. Eng.*, 2017; Vol. 33, p 91.

81. Nguyen, M. M.; Carlini, A. S.; Chien, M.-P.; Sonnenberg, S.; Luo, C.; Braden, R. L.; Osborn, K. G.; Li, Y.; Gianneschi, N. C.; Christman, K. L., Enzyme-Responsive Nanoparticles for Targeted Accumulation and Prolonged Retention in Heart Tissue after Myocardial Infarction. *Advanced Materials* **2015,** *27* (37), 5547-5552.

82. Wojtecki, R. J.; Meador, M. A.; Rowan, S. J., Using the dynamic bond to access macroscopically responsive structurally dynamic polymers. *Nature Materials* **2010,** *10*, 14.

83. Webber, M. J.; Appel, E. A.; Meijer, E. W.; Langer, R., Supramolecular biomaterials. *Nature Materials* **2015,** *15*, 13.

84. Selegård, R.; Aronsson, C.; Brommesson, C.; Dånmark, S.; Aili, D., Folding driven self-assembly of a stimuli-responsive peptide-hyaluronan hybrid hydrogel. *Scientific Reports* **2017,** *7* (1), 7013.

85. Guilbaud, J.-B.; Vey, E.; Boothroyd, S.; Smith, A. M.; Ulijn, R. V.; Saiani, A.; Miller, A. F., Enzymatic Catalyzed Synthesis and Triggered Gelation of Ionic Peptides. *Langmuir* **2010,** *26* (13), 11297-11303.

86. Carlini, A. S.; Gaetani, R.; Braden, R. L.; Luo, C.; Christman, K. L.; Gianneschi, N. C., Enzyme-responsive progelator cyclic peptides for minimally invasive delivery to the heart post-myocardial infarction. *Nature Communications* **2019,** *10* (1), 1735.

87. Sun, J.; Zheng, Q.; Wu, Y.; Liu, Y.; Guo, X.; Wu, W., Biocompatibility of KLD-12 peptide hydrogel as a scaffold in tissue engineering of intervertebral discs in rabbits. *Journal of Huazhong University of Science and Technology* **2010,** *30* (2), 173-177.

88. Tripathi, J. K.; Pal, S.; Awasthi, B.; Kumar, A.; Tandon, A.; Mitra, K.; Chattopadhyay, N.; Ghosh, J. K., Variants of self-assembling peptide, KLD-12 that show both rapid fracture healing and antimicrobial properties. *Biomaterials* **2015,** *56*, 92-103.

89. Bian, Z.; Sun, J., Development of a KLD-12 polypeptide/TGF-β1-tissue scaffold promoting the differentiation of mesenchymal stem cell into nucleus pulposus-like cells for treatment of intervertebral disc degeneration. *International Journal of Clinical and Experimental Pathology* **2015,** *8* (2), 1093-1103.

90. Sun, J.; Zheng, Q., Experimental study on self-assembly of KLD-12 peptide hydrogel and 3-D culture of MSC encapsulated within hydrogel in vitro. *Journal of Huazhong University of Science and Technology* **2009,** *29* (4), 512-516.

91. Wan, S.; Borland, S.; Richardson, S. M.; Merry, C. L. R.; Saiani, A.; Gough, J. E., Self-assembling peptide hydrogel for intervertebral disc tissue engineering. *Acta Biomater.* **2016,** *46*, 29-40.

92. Raghavendra, G. M.; Varaprasad, K.; Jayaramudu, T., Chapter 2 - Biomaterials: Design, Development and Biomedical Applications. In *Nanotechnology Applications for Tissue Engineering*, Thomas, S.; Grohens, Y.; Ninan, N., Eds. William Andrew Publishing: Oxford, 2015; pp 21-44.

93. Fröhlich, E., The role of surface charge in cellular uptake and cytotoxicity of medical nanoparticles. *International Journal of Nanomedicine* **2012,** *7*, 5577-5591.

94. Jiang, Z.; Vasil, A. I.; Hale, J. D.; Hancock, R. E. W.; Vasil, M. L.; Hodges, R. S., Effects of Net Charge and the Number of Positively Charged Residues on the Biological Activity of Amphipathic α-Helical Cationic Antimicrobial Peptides. *Biopolymers* **2008,** *90* (3), 369-383.

95. Kisiday, J.; Jin, M.; Kurz, B.; Hung, H.; Semino, C.; Zhang, S.; Grodzinsky, A. J., Self-assembling peptide hydrogel fosters chondrocyte extracellular matrix production and cell division: Implications for cartilage tissue repair. *Proc. Natl. Acad. Sci. U. S. A.* **2002,** *99* (15), 9996-10001.

96. Grover, G. N.; Braden, R. L.; Christman, K. L., Oxime Cross-Linked Injectable Hydrogels for Catheter Delivery. *Advanced materials (Deerfield Beach, Fla.)* **2013,** *25* (21), 2937-2942.

97. Yan, C.; Altunbas, A.; Yucel, T.; Nagarkar, R. P.; Schneider, J. P.; Pochan, D. J., Injectable solid hydrogel: mechanism of shear-thinning and immediate recovery of injectable β-hairpin peptide hydrogels. *Soft matter* **2010,** *6* (20), 5143-5156.

98. Hernandez, M. J.; Christman, K. L., Designing Acellular Injectable Biomaterial Therapeutics for Treating Myocardial Infarction and Peripheral Artery Disease. *JACC: Basic to Translational Science* **2017,** *2* (2), 212-226.

99. Weber, M.; Steinle, H.; Golombek, S.; Hann, L.; Schlensak, C.; Wendel, H. P.; Avci-Adali, M., Blood-Contacting Biomaterials: In Vitro Evaluation of the Hemocompatibility. *Frontiers in Bioengineering and Biotechnology* **2018,** *6*, 99.

100. Autian, J., Biological Model Systems for the Testing of the Toxicity of Biomaterials. In *Kronenthal R.L., Oser Z., Martin E. (eds) Polymers in Medicine and Surgery*, Springer: Boston, MA, Vol. 8, pp 181-203.

101. Horton, S.; Augustin, S., Activated Clotting Time (ACT). In *Monagle P. (eds) Haemostasis*, Humana Press: Totowa, NJ, 2013; Vol. 992, pp 155-167.

102. Xue, C.; Lin, T. Y.; Chang, D.; Guo, Z., Thioflavin T as an amyloid dye: fibril quantification, optimal concentration and effect on aggregation. *Royal Society Open Science* **2017,** *4* (1), 160696.

103. Hackl, E. V.; Darkwah, J.; Smith, G.; Ermolina, I., Effect of acidic and basic pH on Thioflavin T absorbance and fluorescence. *Eur. Biophys. J.* **2015,** *44* (4), 249-261.

104. Groenning, M., Binding mode of Thioflavin T and other molecular probes in the context of amyloid fibrils—current status. *J. Chem. Biol.* **2010,** *3* (1), 1-18.

105. Chen, Y.; Hua, Y.; Zhang, W.; Tang, C.; Wang, Y.; Zhang, Y.; Qiu, F., Amyloid-like staining property of RADA16-I nanofibers and its potential application in detecting and imaging the nanomaterial. *International Journal of Nanomedicine* **2018,** *13*, 2477-2489.

106. Battistella, C.; Klok, H. A., Controlling and Monitoring Intracellular Delivery of Anticancer Polymer Nanomedicines. *Macromol Biosci* **2017,** *17* (10).

107. Hare, J. I.; Lammers, T.; Ashford, M. B.; Puri, S.; Storm, G.; Barry, S. T., Challenges and strategies in anti-cancer nanomedicine development: An industry perspective. *Adv Drug Deliv Rev* **2017,** *108*, 25-38.

108. Roma-Rodrigues, C.; Mendes, R.; Baptista, P. V.; Fernandes, A. R., Targeting Tumor Microenvironment for Cancer Therapy. *Int J Mol Sci* **2019,** *20* (4).

109. Muntimadugu, E.; Kommineni, N.; Khan, W., Exploring the Potential of Nanotherapeutics in Targeting Tumor Microenvironment for Cancer Therapy. *Pharmacol Res* **2017,** *126*, 109-122.

110. Dougan, M.; Dougan, S. K., Targeting Immunotherapy to the Tumor Microenvironment. *J Cell Biochem* **2017,** *118* (10), 3049-3054.

111. Kzhyshkowska, J.; Bizzarri, M.; Apte, R.; Cherdyntseva, N., Editorial: Targeting of Cancer Cells and Tumor Microenvironment: Perspectives for Personalized Therapy. *Curr Pharm Des* **2017,** *23* (32), 4703-4704.

112. Leibovici, J.; Itzhaki, O.; Huszar, M.; Sinai, J., Targeting the tumor microenvironment by immunotherapy: part 2. *Immunotherapy* **2011,** *3* (11), 1385-408.

113. Wong, C.; Stylianopoulos, T.; Cui, J.; Martin, J.; Chauhan, V. P.; Jiang, W.; Popovic, Z.; Jain, R. K.; Bawendi, M. G.; Fukumura, D., Multistage nanoparticle delivery system for deep penetration into tumor tissue. *Proc Natl Acad Sci U S A* **2011,** *108* (6), 2426-31.

114. Ruan, S. B.; Zhang, L.; Chen, J. T.; Cao, T. W.; Yang, Y. T.; Liu, Y. Y.; He, Q.; Gao, F. B.; Gao, H. L., Targeting delivery and deep penetration using multistage nanoparticles for triple-negative breast cancer. *Rsc Advances* **2015,** *5* (79), 64303-64317.

115. Cun, X. L.; Chen, J. T.; Ruan, S. B.; Zhang, L.; Wan, J. Y.; He, Q.; Gao, H. L., A Novel Strategy through Combining iRGD Peptide with Tumor-Microenvironment-Responsive and Multistage Nanoparticles for Deep Tumor Penetration. *Acs Applied Materials & Interfaces* **2015,** *7* (49), 27458-27466.

116. Zhang, Z. W.; Wang, H.; Tan, T.; Li, J.; Wang, Z. W.; Li, Y. P., Rational Design of Nanoparticles with Deep Tumor Penetration for Effective Treatment of Tumor Metastasis. *Advanced Functional Materials* **2018,** *28* (40).

117. Su, Y. L.; Hu, S. H., Functional Nanoparticles for Tumor Penetration of Therapeutics. *Pharmaceutics* **2018,** *10* (4).

118. Mokhtari, R. B.; Homayouni, T. S.; Baluch, N.; Morgatskaya, E.; Kumar, S.; Das, B.; Yeger, H., Combination therapy in combating cancer. *Oncotarget* **2017,** *8* (23), 38022-38043.

119. Emens, L. A.; Middleton, G., The Interplay of Immunotherapy and Chemotherapy: Harnessing Potential Synergies. *Cancer Immunology Research* **2015,** *3* (5), 436-443.

120. Kessenbrock, K.; Plaks, V.; Werb, Z., Matrix Metalloproteinases: Regulators of the Tumor Microenvironment. *Cell* **2010,** *141* (1), 52-67.

121. Yao, Q.; Kou, L.; Tu, Y.; Zhu, L., MMP-Responsive 'Smart' Drug Delivery and Tumor Targeting. *Trends Pharmacol Sci* **2018,** *39* (8), 766-781.

122. Ku, T. H.; Chien, M. P.; Thompson, M. P.; Sinkovits, R. S.; Olson, N. H.; Baker, T. S.; Gianneschi, N. C., Controlling and Switching the Morphology of Micellar Nanoparticles with Enzymes. *Journal of the American Chemical Society* **2011,** *133* (22), 8392-8395.

123. Chien, M. P.; Thompson, M. P.; Barback, C. V.; Ku, T. H.; Hall, D. J.; Gianneschi, N. C., Enzyme-Directed Assembly of a Nanoparticle Probe in Tumor Tissue. *Advanced Materials* **2013,** *25* (26), 3599-3604.

124. Carlini, A.; Nguyen, M.; Chien, M. P.; Sonnenberg, S.; Luo, C.; Braden, R.; Osborn, K.; Li, Y. W.; Christman, K.; Gianneschi, N., Enzyme-responsive nanoparticles for targeted accumulation and prolonged retention in heart tissue after myocardial infarction. *Abstracts of Papers of the American Chemical Society* **2016,** *251*.

125. Proetto, M. T.; Callmann, C. E.; Cliff, J.; Szymanski, C. J.; Hu, D. H.; Howell, S. B.; Evans, J. E.; Orr, G.; Gianneschi, N. C., Tumor Retention of Enzyme-Responsive Pt(II) Drug-Loaded Nanoparticles Imaged by Nanoscale Secondary Ion Mass Spectrometry and Fluorescence Microscopy. *Acs Central Science* **2018,** *4* (11), 1477-1484.

126. Battistella, C.; Callmann, C. E.; Thompson, M. P.; Yao, S.; Yeldandi, A. V.; Hayashi, T.; Carson, D. A.; Gianneschi, N. C., Delivery of Immunotherapeutic Nanoparticles to Tumors via Enzyme-Directed Assembly. *Adv Healthc Mater* **2019,** *8* (23), e1901105.

127. Liu, G.; Liu, W.; Dong, C. M., UV- and NIR-responsive polymeric nanomedicines for on-demand drug delivery. *Polymer Chemistry* **2013,** *4* (12), 3431-3443.

128. Yu, N.; Huang, L.; Zhou, Y.; Xue, T.; Chen, Z.; Han, G., Near-Infrared-Light Activatable Nanoparticles for Deep-Tissue-Penetrating Wireless Optogenetics. *Adv Healthc Mater* **2019,** *8* (6), e1801132.

129. Zhang, Y.; Ang, C. Y.; Li, M.; Tan, S. Y.; Qu, Q.; Luo, Z.; Zhao, Y., Polymer-Coated Hollow Mesoporous Silica Nanoparticles for Triple-Responsive Drug Delivery. *ACS Appl Mater Interfaces* **2015,** *7* (32), 18179-87.

130. Klan, P.; Solomek, T.; Bochet, C. G.; Blanc, A.; Givens, R.; Rubina, M.; Popik, V.; Kostikov, A.; Wirz, J., Photoremovable Protecting Groups in Chemistry and Biology: Reaction Mechanisms and Efficacy. *Chemical Reviews* **2013,** *113* (1), 119-191.

131. Kammari, L.; Solomek, T.; Ngoy, B. P.; Heger, D.; Klan, P., Orthogonal Photocleavage of a Monochromophoric Linker. *Journal of the American Chemical Society* **2010,** *132* (33), 11431-11433.

132. Lai, J. P.; Mu, X.; Xu, Y. Y.; Wu, X. L.; Wu, C. L.; Li, C.; Chen, J. B.; Zhao, Y. B., Light-responsive nanogated ensemble based on polymer grafted mesoporous silica hybrid nanoparticles. *Chemical Communications* **2010,** *46* (39), 7370-7372.

133. Zheng, J.; Wan, Y.; Elhissi, A.; Zhang, Z. R.; Sun, X., Targeted Paclitaxel Delivery to Tumors Using Cleavable PEG-Conjugated Solid Lipid Nanoparticles. *Pharmaceutical Research* **2014,** *31* (8), 2220-2233.

134. Roomi, M. W.; Kalinovsky, T.; Monterrey, J.; Rath, M.; Niedzwiecki, A., In vitro modulation of MMP-2 and MMP-9 in adult human sarcoma cell lines by cytokines, inducers and inhibitors. *International Journal of Oncology* **2013,** *43* (6), 1787-1798.

135. Lavis, L. D., Ester bonds in prodrugs. *Acs Chemical Biology* **2008,** *3* (4), 203-206.

136. Chen, C. C.; Dai, L. H.; Ma, L. X.; Guo, R. T., Enzymatic degradation of plant biomass and synthetic polymers. *Nat Rev Chem* **2020,** *4* (3), 114-126.

137. Ciechanover, A., Proteolysis: from the lysosome to ubiquitin and the proteasome. *Nat Rev Mol Cell Bio* **2005,** *6* (1), 79-86.

138. Lau, J. L.; Dunn, M. K., Therapeutic peptides: Historical perspectives, current development trends, and future directions. *Bioorgan Med Chem* **2018,** *26* (10), 2700-2707.

139. Roberts, T. C.; Langer, R.; Wood, M. J. A., Advances in oligonucleotide drug delivery. *Nature Reviews Drug Discovery* **2020,** *19* (10), 673-694.

140. Leader, B.; Baca, Q. J.; Golan, D. E., Protein therapeutics: A summary and pharmacological classification. *Nature Reviews Drug Discovery* **2008,** *7* (1), 21-39.

141. Kong, X. D.; Moriya, J.; Carle, V.; Pojer, F.; Abriata, L. A.; Deyle, K.; Heinis, C., De novo development of proteolytically resistant therapeutic peptides for oral administration. *Nat Biomed Eng* **2020,** *4* (5), 560-571.

142. Kale, S. S.; Villequey, C.; Kong, X. D.; Zorzi, A.; Deyle, K.; Heinis, C., Cyclization of peptides with two chemical bridges affords large scaffold diversities. *Nat Chem* **2018,** *10* (7), 715-+.

143. Mourtada, R.; Herce, H. D.; Yin, D. J.; Moroco, J. A.; Wales, T. E.; Engen, J. R.; Walensky, L. D., Design of stapled antimicrobial peptides that are stable, nontoxic and kill antibiotic-resistant bacteria in mice. *Nat Biotechnol* **2019,** *37* (10), 1186-+.

144. Wade, D.; Boman, A.; Wahlin, B.; Drain, C. M.; Andreu, D.; Boman, H. G.; Merrifield, R. B., All-D Amino Acid-Containing Channel-Forming Antibiotic Peptides. *P Natl Acad Sci USA* **1990,** *87* (12), 4761-4765.

145. Walensky, L. D.; Kung, A. L.; Escher, I.; Malia, T. J.; Barbuto, S.; Wright, R. D.; Wagner, G.; Verdine, G. L.; Korsmeyer, S. J., Activation of apoptosis in vivo by a hydrocarbon-stapled BH3 helix. *Science* **2004,** *305* (5689), 1466-1470.

146. Sun, H.; Cao, W.; Zang, N.; Clemons, T. D.; Scheutz, G. M.; Hu, Z.; Thompson, M. P.; Liang, Y.; Vratsanos, M.; Zhou, X.; Choi, W.; Sumerlin, B. S.; Stupp, S. I.; Gianneschi, N. C., Proapoptotic Peptide Brush Polymer Nanoparticles via Photoinitiated Polymerization-Induced Self-Assembly. *Angew Chem Int Ed Engl* **2020**.

147. Blum, A. P.; Kammeyer, J. K.; Gianneschi, N. C., Activating peptides for cellular uptake via polymerization into high density brushes. *Chem Sci* **2016,** *7* (2), 989-994.

148. Blum, A. P.; Kammeyer, J. K.; Yin, J.; Crystal, D. T.; Rush, A. M.; Gilson, M. K.; Gianneschi, N. C., Peptides Displayed as High Density Brush Polymers Resist Proteolysis and Retain Bioactivity. *J Am Chem Soc* **2014,** *136* (43), 15422-15437.

149. Du, B. J.; Yu, M. X.; Zheng, J., Transport and interactions of nanoparticles in the kidneys. *Nat Rev Mater* **2018,** *3* (10), 358-374.

150. Hess, B.; Kutzner, C.; van der Spoel, D.; Lindahl, E., GROMACS 4: Algorithms for Highly Efficient, Load Balanced, and Scalable Molecular Simulation. *J. Chem. Theory Comput.* **2008,** *4*, 435-447.

151. Huang, J.; Rauscher, S.; Nawrocki, G.; Ran, T.; Feig, M.; de Groot, B. L.; Grubmuller, H.; MacKerell Jr, A. D., CHARMM36m: An Improved Force Field for Folded and Intrinsically Disordered Proteins. *Nat. Meth.* **2017,** *14* (1), 71-73.

152. MacKerell, A. D.; Bashford, D.; Bellott, M.; Dunbrack, R. L.; Evanseck, J. D.; Field, M. J.; Fischer, S.; Gao, J.; Guo, H.; Ha, S.; Joseph-McCarthy, D.; Kuchnir, L.; Kuczera, K.; Lau, F. T. K.; Mattos, C.; Michnick, S.; Ngo, T.; Nguyen, D. T.; Prodhom, B.; Reiher, W. E.; Roux, B.; Schlenkrich, M.; Smith, J. C.; Stote, R.; Straub, J.; Watanabe, M.; Wiorkiewicz-Kuczera, J.; Yin, D.; Karplus, M., All-Atom Empirical Potential for Molecular Modeling and Dynamics Studies of Proteins. *J. Phys. Chem. B* **1998,** *102* (18), 3586-3616.

153. Miyamoto, S.; Kollman, P. A., SETTLE: An Analytical Version of the SHAKE and RATTLE Algorithm for Rigid Water Models. *J. Comput. Chem.* **1992,** *13*, 952-962.

154. Vanommeslaeghe, K.; Hatcher, E.; Acharya, C.; Kundu, S.; Zhong, S.; Shim, J.; Darian, E.; Guvench, O.; Lopes, P.; Vorobyov, I.; Mackerell, A. D., CHARMM General Force Field: A Force Field for Drug-Like Molecules Compatible with the CHARMM All-Atom Additive Biological Force Fields. *J. Comput. Chem.* **2010,** *31* (4), 671-690.

155. Vanommeslaeghe, K.; MacKerell, A. D., Automation of the CHARMM General Force Field (CGenFF) I: Bond Perception and Atom Typing. *J. Chem. Inf. Model* **2012,** *52* (12), 3144-3154.

156. Vanommeslaeghe, K.; Raman, E. P.; MacKerell, A. D., Automation of the CHARMM General Force Field (CGenFF) II: Assignment of Bonded Parameters and Partial Atomic Charges. *J. Chem. Inf. Model* **2012,** *52* (12), 3155-3168.

157. Ferru, G.; Reinhart, B.; Bera, M. K.; Olvera de la Cruz, M.; Qiao, B.; Ellis, R. J., The Lanthanide Contraction beyond Coordination Chemistry. *Chem. Eur. J.* **2016,** *22* (20), 6899-6904.

158. Qiao, B.; Ferru, G.; Olvera de la Cruz, M.; Ellis, R. J., Molecular Origins of Mesoscale Ordering in a Metalloamphiphile Phase. *ACS Cent. Sci.* **2015,** *1* (9), 493-503.

159. Darden, T.; York, D.; Pedersen, L., Particle Mesh Ewald: An N·log(N) Method for Ewald Sums in Large Systems. *J. Chem. Phys.* **1993,** *98,* 10089-10092.

160. Essmann, U.; Perera, L.; Berkowitz, M. L.; Darden, T.; Lee, H.; Pedersen, L., A Smooth Particle Mesh Ewald Method. *J. Chem. Phys.* **1995,** *103*, 8577-93.

161. Lee, J.; Cheng, X.; Swails, J. M.; Yeom, M. S.; Eastman, P. K.; Lemkul, J. A.; Wei, S.; Buckner, J.; Jeong, J. C.; Qi, Y.; Jo, S.; Pande, V. S.; Case, D. A.; Brooks, C. L.; MacKerell, A. D.; Klauda, J. B.; Im, W., CHARMM-GUI Input Generator for NAMD, GROMACS, AMBER, OpenMM, and CHARMM/OpenMM Simulations Using the CHARMM36 Additive Force Field. *J. Chem. Theory Comput.* **2016,** *12* (1), 405-413.

162. Panganiban, B.; Qiao, B.; Jiang, T.; DelRe, C.; Obadia, M. M.; Nguyen, T. D.; Smith, A. A. A.; Hall, A.; Sit, I.; Crosby, M. G.; Dennis, P. B.; Drockenmuller, E.; Olvera de la Cruz, M.; Xu, T., Random Heteropolymers Preserve Protein Function in Foreign Environments. *Science* **2018,** *359* (6381), 1239-1243.

163. Qiao, B.; Lopez, L.; Olvera de la Cruz, M., "Mirror"-Like Protein Dimers Stabilized by Local Heterogeneity at Protein Surfaces. *J. Phys. Chem. B* **2019,** *123* (18), 3907-3915.

164. Qiao, B.; Jiménez-Ángeles, F.; Nguyen, T. D.; Olvera de la Cruz, M., Water Follows Polar and Nonpolar Protein Surface Domains. *Proc. Natl. Acad. Sci. U. S. A.* **2019,** *116*, 19274-19281.

165. Qiao, B.; Olvera de la Cruz, M., Enhanced Binding of SARS-CoV-2 Spike Protein to Receptor by Distal Polybasic Cleavage Sites. *ACS Nano* **2020,** *14*, 10616-10623.

166. Jiang, T.; Hall, A.; Eres, M.; Hemmatian, Z.; Qiao, B.; Zhou, Y.; Ruan, Z.; Couse, A. D.; Heller, W. T.; Huang, H.; de la Cruz, M. O.; Rolandi, M.; Xu, T., Single-chain heteropolymers transport protons selectively and rapidly. *Nature* **2020,** *577* (7789), 216-220.

167. Eisenhaber, F.; Lijnzaad, P.; Argos, P.; Sander, C.; Scharf, M., The double cubic lattice method: Efficient approaches to numerical integration of surface area and volume and to dot surface contouring of molecular assemblies. *J. Comput. Chem.* **1995,** *16* (3), 273-284.

168. Monticelli, L.; Kandasamy, S. K.; Periole, X.; Larson, R. G.; Tieleman, D. P.; Marrink, S.-J., The MARTINI Coarse-Grained Force Field: Extension to Proteins. *J. Chem. Theory Comput.* **2008,** *4* (5), 819-834.

169. de Jong, D. H.; Singh, G.; Bennett, W. F. D.; Arnarez, C.; Wassenaar, T. A.; Schäfer, L. V.; Periole, X.; Tieleman, D. P.; Marrink, S. J., Improved Parameters for the Martini Coarse-Grained Protein Force Field. *J. Chem. Theory Comput.* **2013,** *9* (1), 687-697.

170. Vögele, M.; Holm, C.; Smiatek, J., Coarse-grained simulations of polyelectrolyte complexes: MARTINI models for poly(styrene sulfonate) and poly(diallyldimethylammonium). *J. Chem. Phys.* **2015,** *143* (24), 243151.

171. Grunewald, F.; Rossi, G.; de Vries, A. H.; Marrink, S. J.; Monticelli, L., Transferable MARTINI Model of Poly(ethylene Oxide). *J. Phys. Chem. B* **2018,** *122* (29), 7436-7449.

172. Marrink, S. J.; Risselada, H. J.; Yefimov, S.; Tieleman, D. P.; de Vries, A. H., The MARTINI Force Field: Coarse Grained Model for Biomolecular Simulations. *J. Phys. Chem. B* **2007,** *111* (27), 7812-7824.

173. López, C. A.; Rzepiela, A. J.; de Vries, A. H.; Dijkhuizen, L.; Hünenberger, P. H.; Marrink, S. J., Martini Coarse-Grained Force Field: Extension to Carbohydrates. *J. Chem. Theory Comput.* **2009,** *5* (12), 3195-3210.

174. Leung, C.-Y.; Palmer, L. C.; Qiao, B.; Kewalramani, S.; Sknepnek, R.; Newcomb, C. J.; Greenfield, M. A.; Vernizzi, G.; Stupp, S. I.; Bedzyk, M. J.; Olvera de la Cruz, M., Molecular Crystallization Controlled by pH Regulates Mesoscopic Membrane Morphology. *ACS Nano* **2012,** *6*, 10901-10909.

175. Marrink, S. J.; Tieleman, D. P., Perspective on the Martini model. *Chem. Soc. Rev.* **2013,** *42* (16), 6801-6822.

176. de Jong, D. H.; Baoukina, S.; Ingólfsson, H. I.; Marrink, S. J., Martini straight: Boosting performance using a shorter cutoff and GPUs. *Comput. Phys. Commun.* **2016,** *199*, 1-7.

177. Periole, X.; Cavalli, M.; Marrink, S.-J.; Ceruso, M. A., Combining an Elastic Network With a Coarse-Grained Molecular Force Field: Structure, Dynamics, and Intermolecular Recognition. *J. Chem. Theory Comput.* **2009,** *5* (9), 2531-2543.

178. Poma, A. B.; Cieplak, M.; Theodorakis, P. E., Combining the MARTINI and Structure-Based Coarse-Grained Approaches for the Molecular Dynamics Studies of Conformational Transitions in Proteins. *J. Chem. Theory Comput.* **2017,** *13* (3), 1366-1374.

179. Souza, P. C. T.; Thallmair, S.; Marrink, S. J.; Mera-Adasme, R., An Allosteric Pathway in Copper, Zinc Superoxide Dismutase Unravels the Molecular Mechanism of the G93A Amyotrophic Lateral Sclerosis-Linked Mutation. *J. Phys. Chem. Lett.* **2019,** *10* (24), 7740-7744.

180. Thallmair, S.; Vainikka, P. A.; Marrink, S. J., Lipid Fingerprints and Cofactor Dynamics of Light-Harvesting Complex II in Different Membranes. *Biophys. J.* **2019,** *116* (8), 1446-1455.

181. Corrigan, N.; Yeow, J.; Judzewitsch, P.; Xu, J.; Boyer, C., Seeing the Light: Advancing Materials Chemistry through Photopolymerization. *Angew Chem Int Ed Engl* **2019,** *58* (16), 5170-5189.

182. Xu, J.; Jung, K.; Atme, A.; Shanmugam, S.; Boyer, C., A robust and versatile photoinduced living polymerization of conjugated and unconjugated monomers and its oxygen tolerance. *J Am Chem Soc* **2014,** *136* (14), 5508-19.

183. Chen, M.; Zhong, M.; Johnson, J. A., Light-Controlled Radical Polymerization: Mechanisms, Methods, and Applications. *Chem Rev* **2016,** *116* (17), 10167-211.

184. Molla, M. R.; Rangadurai, P.; Antony, L.; Swaminathan, S.; de Pablo, J. J.; Thayumanavan, S., Author Correction: Dynamic actuation of glassy polymersomes through isomerization of a single azobenzene unit at the block copolymer interface. *Nat Chem* **2018,** *10* (8), 895.

185. Yang, L.; Sun, H.; Liu, Y.; Hou, W.; Yang, Y.; Cai, R.; Cui, C.; Zhang, P.; Pan, X.; Li, X.; Li, L.; Sumerlin, B. S.; Tan, W., Self-Assembled Aptamer-Grafted Hyperbranched Polymer Nanocarrier for Targeted and Photoresponsive Drug Delivery. *Angew Chem Int Ed Engl* **2018,** *57* (52), 17048-17052.

186. Niu, J.; Lunn, D. J.; Pusuluri, A.; Yoo, J. I.; O'Malley, M. A.; Mitragotri, S.; Soh, H. T.; Hawker, C. J., Engineering live cell surfaces with functional polymers via cytocompatible controlled radical polymerization. *Nat Chem* **2017,** *9* (6), 537-545.

187. Pan, X.; Lathwal, S.; Mack, S.; Yan, J.; Das, S. R.; Matyjaszewski, K., Automated Synthesis of Well-Defined Polymers and Biohybrids by Atom Transfer Radical Polymerization Using a DNA Synthesizer. *Angew Chem Int Ed Engl* **2017,** *56* (10), 2740-2743.

188. Pan, X.; Fang, C.; Fantin, M.; Malhotra, N.; So, W. Y.; Peteanu, L. A.; Isse, A. A.; Gennaro, A.; Liu, P.; Matyjaszewski, K., Mechanism of Photoinduced Metal-Free Atom Transfer Radical Polymerization: Experimental and Computational Studies. *J Am Chem Soc* **2016,** *138* (7), 2411-25.

189. Xu, J.; Shanmugam, S.; Fu, C.; Aguey-Zinsou, K. F.; Boyer, C., Selective Photoactivation: From a Single Unit Monomer Insertion Reaction to Controlled Polymer Architectures. *J Am Chem Soc* **2016,** *138* (9), 3094-106.

190. Ogawa, K. A.; Goetz, A. E.; Boydston, A. J., Metal-free ring-opening metathesis polymerization. *J Am Chem Soc* **2015,** *137* (4), 1400-3.

191. Kottisch, V.; Supej, M. J.; Fors, B. P., Enhancing Temporal Control and Enabling Chain-End Modification in Photoregulated Cationic Polymerizations by Using Iridium-Based Catalysts. *Angew Chem Int Ed Engl* **2018,** *57* (27), 8260-8264.

192. Michaudel, Q.; Kottisch, V.; Fors, B. P., Cationic Polymerization: From Photoinitiation to Photocontrol. *Angew Chem Int Ed Engl* **2017,** *56* (33), 9670-9679.

193. Kottisch, V.; Michaudel, Q.; Fors, B. P., Cationic Polymerization of Vinyl Ethers Controlled by Visible Light. *J Am Chem Soc* **2016,** *138* (48), 15535-15538.

194. Fu, C.; Xu, J.; Boyer, C., Photoacid-mediated ring opening polymerization driven by visible light. *Chem Commun (Camb)* **2016,** *52* (44), 7126-9.

195. Gormley, A. J.; Yeow, J.; Ng, G.; Conway, O.; Boyer, C.; Chapman, R., An Oxygen-Tolerant PET-RAFT Polymerization for Screening Structure-Activity Relationships. *Angew Chem Int Ed Engl* **2018,** *57* (6), 1557-1562.

196. Blackman, L. D.; Varlas, S.; Arno, M. C.; Houston, Z. H.; Fletcher, N. L.; Thurecht, K. J.; Hasan, M.; Gibson, M. I.; O'Reilly, R. K., Confinement of Therapeutic Enzymes in Selectively Permeable Polymer Vesicles by Polymerization-Induced Self-Assembly (PISA) Reduces Antibody Binding and Proteolytic Susceptibility. *ACS Cent Sci* **2018,** *4* (6), 718-723.

197. Hill, M. R.; Carmean, R. N.; Sumerlin, B. S., Expanding the Scope of RAFT Polymerization: Recent Advances and New Horizons. *Macromolecules* **2015,** *48* (16), 5459-5469.

198. Blum, A. P.; Kammeyer, J. K.; Yin, J.; Crystal, D. T.; Rush, A. M.; Gilson, M. K.; Gianneschi, N. C., Peptides displayed as high density brush polymers resist proteolysis and retain bioactivity. *J Am Chem Soc* **2014,** *136* (43), 15422-37.

199. Blum, A. P.; Kammeyer, J. K.; Gianneschi, N. C., Activating Peptides for Cellular Uptake via Polymerization into High Density Brushes. *Chem Sci* **2016,** *7* (2), 989-994.

200. Maynard, H. D.; Okada, S. Y.; Grubbs, R. H., Inhibition of cell adhesion to fibronectin by oligopeptide-substituted polynorbornenes. *J Am Chem Soc* **2001,** *123* (7), 1275-9.

201. Adamiak, L.; Touve, M. A.; LeGuyader, C. L. M.; Gianneschi, N. C., Peptide Brush Polymers and Nanoparticles with Enzyme-Regulated Structure and Charge for Inducing or Evading Macrophage Cell Uptake. *ACS Nano* **2017,** *11* (10), 9877-9888.

202. Conrad, R. M.; Grubbs, R. H., Tunable, temperature-responsive polynorbornenes with side chains based on an elastin peptide sequence. *Angew Chem Int Ed Engl* **2009,** *48* (44), 8328-30.

203. Fairbanks, B. D.; Gunatillake, P. A.; Meagher, L., Biomedical applications of polymers derived by reversible addition - fragmentation chain-transfer (RAFT). *Adv Drug Deliv Rev* **2015,** *91*, 141-52.

204. Cieslewicz, M.; Tang, J.; Yu, J. L.; Cao, H.; Zavaljevski, M.; Motoyama, K.; Lieber, A.; Raines, E. W.; Pun, S. H., Targeted delivery of proapoptotic peptides to tumor-associated macrophages improves survival. *Proc Natl Acad Sci U S A* **2013,** *110* (40), 15919-24.

205. Doncom, K. E. B.; Blackman, L. D.; Wright, D. B.; Gibson, M. I.; O'Reilly, R. K., Dispersity effects in polymer self-assemblies: a matter of hierarchical control. *Chem Soc Rev* **2017,** *46* (14), 4119-4134.

206. Uno, K.; Bhutto, I. A.; McLeod, D. S.; Merges, C.; Lutty, G. A., Impaired expression of thrombospondin-1 in eyes with age related macular degeneration. *Br J Ophthalmol* **2006,** *90* (1), 48-54.

207. Foulsham, W.; Dohlman, T. H.; Mittal, S. K.; Taketani, Y.; Singh, R. B.; Masli, S.; Dana, R., Thrombospondin-1 in ocular surface health and disease. *Ocul Surf* **2019,** *17* (3), 374-383.

208. Zhang, X.; Lawler, J., Thrombospondin-based antiangiogenic therapy. *Microvasc Res* **2007,** *74* (2-3), 90-9.

209. Su, X.; Abumrad, N. A., Cellular fatty acid uptake: a pathway under construction. *Trends Endocrinol Metab* **2009,** *20* (2), 72-7.

210. Isenberg, J. S.; Jia, Y.; Fukuyama, J.; Switzer, C. H.; Wink, D. A.; Roberts, D. D., Thrombospondin-1 inhibits nitric oxide signaling via CD36 by inhibiting myristic acid uptake. *J Biol Chem* **2007,** *282* (21), 15404-15.

211. Shao, Z.; Friedlander, M.; Hurst, C. G.; Cui, Z.; Pei, D. T.; Evans, L. P.; Juan, A. M.; Tahiri, H.; Duhamel, F.; Chen, J.; Sapieha, P.; Chemtob, S.; Joyal, J. S.; Smith, L. E., Choroid sprouting assay: an ex vivo model of microvascular angiogenesis. *PLoS One* **2013,** *8* (7), e69552.

212. Frank, S., Treatment of Huntington's disease. *Neurotherapeutics* **2014,** *11* (1), 153-60.

213. Jimenez-Sanchez, M.; Licitra, F.; Underwood, B. R.; Rubinsztein, D. C., Huntington's Disease: Mechanisms of Pathogenesis and Therapeutic Strategies. *Cold Spring Harb Perspect Med* **2017,** *7* (7).

214. Franco-Iborra, S.; Vila, M.; Perier, C., Mitochondrial Quality Control in Neurodegenerative Diseases: Focus on Parkinson's Disease and Huntington's Disease. *Front Neurosci* **2018,** *12*, 342.

215. Yin, X.; Manczak, M.; Reddy, P. H., Mitochondria-targeted molecules MitoQ and SS31 reduce mutant huntingtin-induced mitochondrial toxicity and synaptic damage in Huntington's disease. *Hum Mol Genet* **2016,** *25* (9), 1739-53.

216. Rawlins, M. D.; Wexler, N. S.; Wexler, A. R.; Tabrizi, S. J.; Douglas, I.; Evans, S. J.; Smeeth, L., The Prevalence of Huntington's Disease. *Neuroepidemiology* **2016,** *46* (2), 144-53.

217. Kumar, A.; Kumar Singh, S.; Kumar, V.; Kumar, D.; Agarwal, S.; Rana, M. K., Huntington's disease: an update of therapeutic strategies. *Gene* **2015,** *556* (2), 91-7.

218. Kordasiewicz, H. B.; Stanek, L. M.; Wancewicz, E. V.; Mazur, C.; McAlonis, M. M.; Pytel, K. A.; Artates, J. W.; Weiss, A.; Cheng, S. H.; Shihabuddin, L. S.; Hung, G.; Bennett, C. F.; Cleveland, D. W., Sustained therapeutic reversal of Huntington's disease by transient repression of huntingtin synthesis. *Neuron* **2012,** *74* (6), 1031-44.

219. Bano, D.; Zanetti, F.; Mende, Y.; Nicotera, P., Neurodegenerative processes in Huntington's disease. *Cell Death Dis* **2011,** *2*, e228.

220. Guo, X.; Sun, X.; Hu, D.; Wang, Y. J.; Fujioka, H.; Vyas, R.; Chakrapani, S.; Joshi, A. U.; Luo, Y.; Mochly-Rosen, D.; Qi, X., VCP recruitment to mitochondria causes mitophagy impairment and neurodegeneration in models of Huntington's disease. *Nat Commun* **2016,** *7*, 12646.

221. Fosgerau, K.; Hoffmann, T., Peptide therapeutics: current status and future directions. *Drug Discov Today* **2015,** *20* (1), 122-8.

222. Craik, D. J.; Fairlie, D. P.; Liras, S.; Price, D., The future of peptide-based drugs. *Chem Biol Drug Des* **2013,** *81* (1), 136-47.

223. Kaspar, A. A.; Reichert, J. M., Future directions for peptide therapeutics development. *Drug Discov Today* **2013,** *18* (17-18), 807-17.

224. Vlieghe, P.; Lisowski, V.; Martinez, J.; Khrestchatisky, M., Synthetic therapeutic peptides: science and market. *Drug Discov Today* **2010,** *15* (1-2), 40-56.

225. Otvos, L., Jr.; Wade, J. D., Current challenges in peptide-based drug discovery. *Front Chem* **2014,** *2*, 62.

226. Kammeyer, J. K.; Blum, A. P.; Adamiak, L.; Hahn, M. E.; Gianneschi, N. C., Polymerization of protecting-group-free peptides via ROMP. *Polym Chem-Uk* **2013,** *4* (14), 3929-3933.

227. Kammeyer, J. K.; Blum, A. P.; Adamiak, L.; Hahn, M. E.; Gianneschi, N. C., Polymerization of Protecting-Group-Free Peptides via ROMP. *Polym Chem* **2013,** *41*, 3929-3933.